Study of particle transport in high pressure sputter deposition process

Takeo Nakano

December 2001

Preface

The objective of this study is to propose the new methods to simulate the transport process of atoms and molecules in high pressure (5–50 Pa) sputter deposition process. More specifically, we extend the conventional Monte Carlo (MC) simulation from two standpoints. One is to introduce the effect of the thermal motion of ambient gas atoms/molecules, which has conventionally been ignored, into the MC calculation of collision and scattering process between the sputtered particles and the gases. The other is to formulate the random diffusion process of the sputtered particles, which occurs after they decelerated, by Poisson's equation sand to solve it using the Boundary Element Method (BEM).

Sputtered particles have large kinetic energy when they are ejected from the target, but their speed is decelerated by the collision with gas atoms so that the gas motion becomes gradually important. This is especially significant in high pressure environment, since the collision occurs more frequently. The first extension is to treat this gas motion properly based on the kinetic theory of gases.

When the pressure (hence the collision event) increases more, the calculational complexity proportional to the square of it is required to trace the sputtered particle by MC method until they deposit onto the chamber wall. The second extension aims to reduce this. It treats the transport of the sputtered particles by the diffusion equation, after they lose their large initial energy (and momentum).

Simulation program has been implemented based on these ideas, and applied to the following problems to check the validity of the model as well as to understand the physics behind these phenomena.

- Deceleration process of high energy atoms in gas environment. It's a typification of the transport of sputtered atoms from the target. Especially, the effect of the thermal gas motion on this transport behaviour is speculated by comparing the cases with/without the gas motion.

- Thickness profile of sputtered copper films. Firstly, the effect of the distance from the chamber wall on the thickness profile is studied. At higher pressures, films also deposit on chamber walls from which the target cannot be seen directly. The pressure dependence of this diversion phenomenon is investigated, and its relationship with the particle transport process is discussed.

- The deviation of the film stoichiometry from that of the composite target material, and its dependence on the gas pressure. Lanthanum hexaboride (LaB_6) is used as the model

case. The reason of this is discussed considering the difference in the transport process between lanthanum and boron atoms, which reflects the mass difference of these.

- Evaluation of spatial density of sputtered atoms. Using the extended method introduced in this study, we can trace the motion of sputtered atoms precisely. We applied this feature to calculate the atomic density of these sputtered atoms. When you observe the optical emission from Cu sputter plasma, the emission including the ground state, as the final state of its transition, is re-absorbed by the ambient Cu atoms in ground state. Therefore, the higher the atomic density is, the lower the intensity of these emissions are. The calculated atomic density using our simulation model is shown to be in accordance with the one expected from the decrement of this kind of emission.

The contents of this thesis are as follows.

Chapter 1 is the introduction. Researches on sputter deposition process are reviewed mainly from the theoretical viewpoint, and the modeling/simulation of the sputter deposition is mentioned. Subsequently, studies treating the MC simulation of particle transport process are summarized. By showing the problems in these previous studies, the objective of this study is clarified.

In chapter 2, details of the particle transport simulation used in this study are described. By reconsidering the physical backgrounds of them, their validity and limitation are considered. Next, the two methods introduced in this study are explained; incorporation of the gas motion into the collision of sputtered particles with gases, and the treatment of thermal diffusion process of sputtered particles via diffusion equation. The latter will be compared with the result of Monte Carlo method, and its validity is discussed.

In chapter 3, the simulation program is applied to the problems listed above. We will check how well the simulation reproduce the experimental results, and discuss by what reason those phenomena occur.

Finally, the study is summarized in chapter 4.

The proposed model in this study is implemented into the FORTRAN/C program working on Linux operating system. In appendix A, this program is described; availability, usage, algorisms, structure of the program, etc.

In appendix B, atomic parameters used in this study are given in a table.

Contents

List of Figures

Chapter 1

Introduction

Film preparation using sputtering phenomena is classified in the Physical Vapor Deposition (PVD) process, and has been widely used in these days [105,161]. For industrial purposes, sputter deposition frequently accompanies the low pressure discharges. By applying a high-voltage to noble gas of 0.1–10 Pa, you can generate a glow discharge plasma. Then a sputtering target is introduced into the plasma, and negative bias is applied to it, which cause the bombardment of the target by positive ions and the ejection of target materials via sputtering phenomenon. These ejected particles travel through the gas environment, and some of them will deposit onto the substrate and form the film. The deposition system using this method can be constructed rather easily; evacuation of the chamber, introduction of the discharge gas and the application of the high voltage. Though the sputter deposition had some disadvantages in the early stages, they have been conquered through developments of new techniques: e.g., magnetron sputtering has enabled the faster deposition, and RF sputtering has made this applicable to the insulating targets. And now sputtering is used with almost all the materials.

The merit of the sputtering method, compared to the ordinary vacuum deposition, is the presence of high energy particles that hit the substrate. It has been reported that the denseness, the adhesion, and/or the strain of the film are improved or controlled [79,116,118,164,165] by the bombardment with moderated energy and fluence.

On the other hand, however, it is not easy to determine the optimum deposition condition in sputter deposition. It is because that relationships are not straightforward between the experimental parameters and the internal parameters of the process (former include chamber shapes, pressure of the gas, discharge power / voltage, etc., while the latter include electron temperature / density of the plasma, ion generation frequency, sputtering yield of the target, etc.). They are summarized in figure 1.1. It is generally difficult to predict the film property or the thickness profile from experimental parameters, and cut-and-try method with many repetitions of experiments is necessary to optimize such conditions.

The topic of this study is the theoretical / experimental research on the "Particle Transfer" in the fig. 1.1, where the particles ejected from the target are transported onto the substrate. In this field, the usefulness of the Monte Carlo (MC) method is widely accepted today. However, the conventional MC simulation suffer from the discrepancy between its results and experiments at high pressure region, where much more collision of sputtered particles occur.

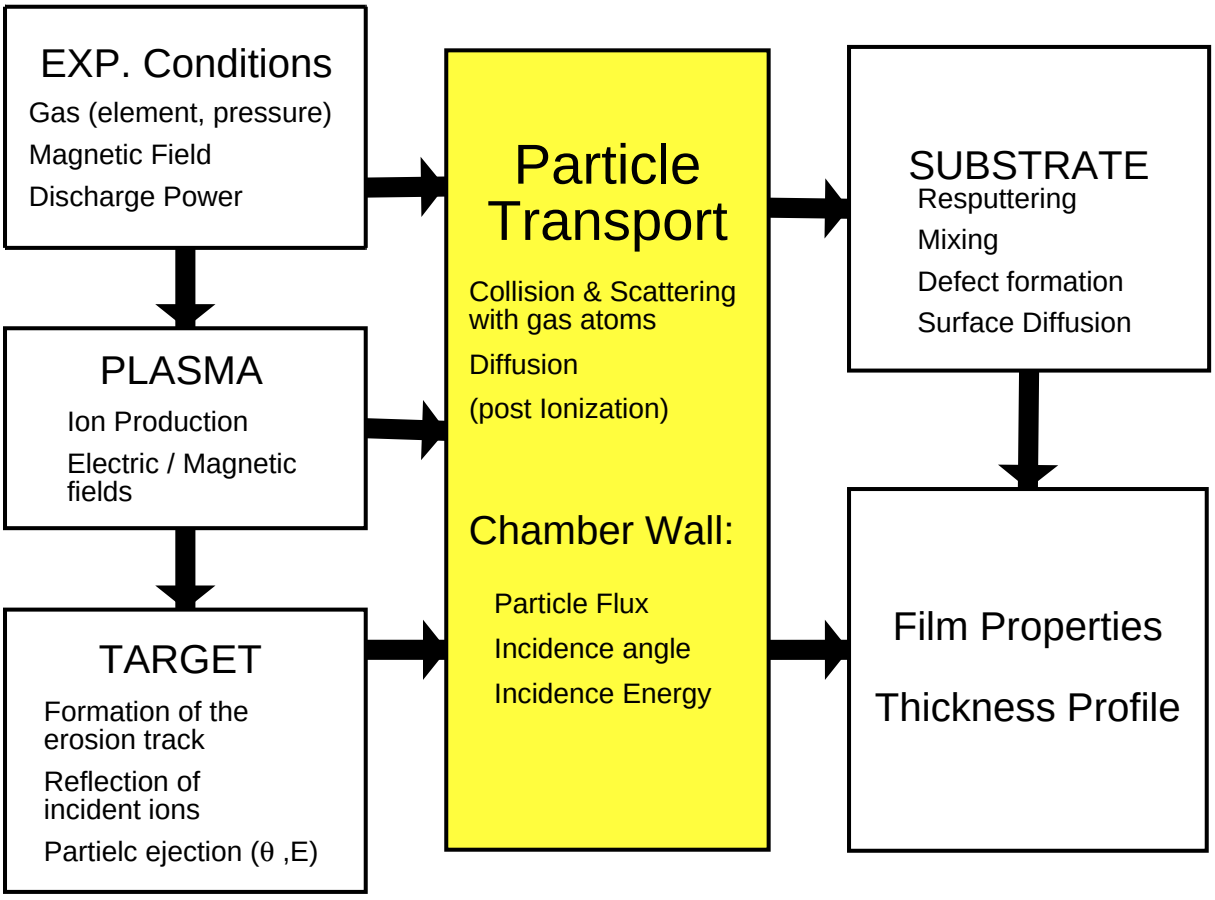

Figure 1.1: Schematics of the sputter deposition process.

In this study, we try to extend the MC framework and enable more reasonable and realistic simulation at high pressures. We also proposed the method to reduce the calculational complexity, which increases at the square of the gas pressure in MC. By comparing the experimental results with simulation we developed, we discuss the physical processes of sputtered particles and their behavior in high pressure environment.

In this chapter, we review the studies on the sputter deposition. In the first 4 sections, overall sputtering process is roughly categorized based on fig. 1.1; plasma generation, target processes, particle transport, and atomic processes at the substrate. Studies on those topics will be summarized mainly from theoretical viewpoint, to clarify the position of the MC study of the transport process. The next section refers some experimental results on the sputtering deposition of compounds. It has been reported that the film composition deviates from the target, which will be discussed in this study in conjunction with the particle transport process. The next section reviews historically the Monte Carlo method applied to the transport process in detail. Finally, the purpose of this study is presented in the last section.

1.1 Magnetron plasma

Fundamental processes occurring in low pressure discharges used for film deposition have been attracted many interests [69].

For sputter deposition process, development of the magnetron plasma has the significant importance. It has been proposed in 1960's by Kay *et al.* to generate and maintain the plasma at lower gas pressures [158,161]. It uses magnetic field to confine electrons near the target, which enhances the ion production, enables the plasma ignition at low gas pressure, and increase greatly the deposition rate of films.

On the other hand, it has some disadvantages caused by its spatial inhomogeneity. For example, non-uniform of positive ion production generates the "erosion track" on the target, which reduces the efficiency of the target usage. The inhomogeneity of the plasma also makes difficult the theoretical treatment of it.

From the viewpoint of the transport process, the energy and fluence profiles of incident ions onto the target affect the ejection of the sputtered particles. In this section, we mention several reports on this topic.

1.1.1 Magnetic configuration near the target

Since its early years, design and optimization of the magnetic configuration of the magnetron has vigorously been studied. It is because that it affects the efficiency of the target consumption, stabilization of the discharge, and the reduction of substrate heating via the confinement of the plasma (for example, the topics in 1980's has been summarized by Almeida [2]). In 1991, Rao *et al.* have studied the ring type magnetron with various combinations of magnets and yokes, and pointed out [111]:

- Stronger magnetic field maintains the discharge at lower pressure, or generates larger current at constant voltage.

- Spatial distribution of the magnetic field determines the uniformity of the erosion and/or the trapping efficiency of electrons. If the latter becomes worse, the substrate is heated up by those escaped from the confined plasma region.
- If electrons escape, cathode current decreases in high voltages.

On the contrary, "unbalanced magnetron" configuration is proposed in 1986, where the yoke is saturated and the magnetic flux escapes above the target [167]. With these flux from the target to the substrate, ions and/or electrons are conveyed toward the target, by which the film growth process will be controlled. Howson *et al.* has performed the probe measurement with this unbalanced type magnetron plasma, and obtained the ion energy distribution near the target as a function of gas pressure and discharge power [50]. By insulating the substrate, 30 V of substrate self-bias and 100 mW/cm^2 of heat supply to the substrate were observed.

In 1995, the group of Musil and Kadlec have developed the experimental system with two electromagnets in between / outside of two cylindrical yokes. The system can generate both balanced and unbalanced magnetron configuration by changing the current ratio of these electromagnets [96]. With this system, they observed that the dependency of discharge ignition pressure on the current ratio, and found its minimum at $I_{\rm outer}/I_{\rm inner} \sim 2$. By calculating the magnetic fields, they showed that the area of the target face covered by the magnetic flux became maximum at this current ratio [58].

1.1.2 Electron trajectory and ion production

As mentioned above, the ion production profile is inhomogeneous in the magnetron plasma. It is important to predict this profile for the simulation of sputter deposition process, since it gives the way to calculate the erosion formation from the magnetic configuration.

Sheridan *et al.* [132] have developed the method to do this using Monte Carlo simulation of the electron motion. They traced the electrons produced at the target by secondary electron emission process. They solved the equation of motion of the electron in the applied electric and magnetic fields. During the motion, electron collides with gas atoms, and ionizes them with some probability. Those ions are then dragged onto the target, bombard it and produce another secondary electrons. Iterating this processes, they could obtain the arrival distribution of ions (=depth profile of the erosion) for given magnetic configuration, which agreed fairly well with experiments.

Ido *et al.* at Saitama University have extended this MC simulation method, and applied them to the erosion track formation on the target of magnetic materials [52–54]. Shidoji *et al.* also have used this method for the rectangular target, and obtained the good agreement with the experimentally obtained erosion depth profiles.

Though the method of Sheridan has been used widely, it has to assume the electric field profile before the simulation, hence is not an *a priori* calculation. But there have been several proposals recently, to predict the sheath potential of plasma without magnetic fields [10] as well as for Ar magnetron plasma [134]. Both of these are the combinations of fluid dynamical approach and of kinematical one for the electron motions. If they are merged with the Sheridan's method, it will be possible to predict the erosion track from the magnet configurations, and to optimize it during the design. The probe measurement of the plasma parameters and the spatial

distribution of them has also been performed by Sheridan's group themselves [133], which will be compared with theories and activate the development of the theoretical considerations in the future.

1.1.3 Sheath formation in RF plasma

In DC discharges, the potential drop at the cathode sheath is almost equivalent to the discharge voltage, and the energy of ions bombarding the target is almost identical to sheath potential drop times the ion charge[1]. On the other hand, the ion energy distribution in radio frequency (RF) discharge is more complicated and has been extensively studied.

The study reported by Tsui [150] in 1968 was one of the pioneering work in this field. He solved equations of motion for ions and electrons under the electric field with both RF and DC (self-bias) components. The resultant ion energy distribution function (IEDF) has two peaks at top and bottom energies of the distribution.

This shape of distribution has confirmed by the experiment by Coburn and Kay [16], who measured the IEDF at the DC biased substrate exposed to the RF plasma. Recent experiment [77] and calculation [76] also supports the IEDF of Tsui's.

1.1.4 Gas rarefaction effect

For the particle transport, gas density is a critical parameter since it determines the collision frequency of sputtered particles. It has been proposed that the gas density is reduced near the discharge target, which is called "gas rarefaction effect". In sputter deposition, sputtering target can be regarded as the source of various kind of high energy particles, such as reflected and neutralized ions, charge exchanged atoms, and sputtered target atoms. They heat the gas near the target region which reduces the density of them (assuming the pressure is constant).

This effect has been proposed by Rossnagel [115], based on the concept of "sputtering wind" by Hoffman [45]. Rossnagel has measured this local reduction directly by inserting the tube near the cathode, and proposed the model that the gas density is proportional to the one-second power of the discharge current.

He also has studied the magnetron sputtering discharges by various techniques, and discussed the ramification of this effect. It includes the saturation of the optical emission intensity at high power region [122], and the energy distribution of ions incident on the substrate [116].

1.2 Processes at the target

Sputtering process on solid state surfaces has initially been studied mainly motivated by the surface damages introduced by radiations. And as the sputter deposition technique came to be used widely, energy and angular distributions of sputtered particles, which are necessary for the simulation, have also been attracting interests.

[1] if we can neglect the charge exchange process [21].

1.2.1 Sputtering phenomena

In the field of theoretical study of sputtering, Thompson's work for energy distribution [146] and Sigmund's for the sputtering yield [135] have been well known and cited frequently. Since the former is especially important for the MC simulation, it will be mentioned in detail in 2.2.2.

After their work, Monte Carlo codes (*MALOWE*, *TRIM*, *ACAT*, etc.) have been developed, and been applied to obtain various properties of sputtering: angular distribution [61,103], energy distribution [15,176], dependence of sputtering yield on primary ion energy [128], and the depth profile of ejected particles [107].

Experimental studies have also been carried out intensively (most of which has been compiled by Mahan [72]). Especially, the angular profile of sputtered particles measured by Tsuge for polycrystalline metal [149] has actually been used by several groups in the particle transport simulation. In view of experimental technique, the work by Whitaker *et al.* is also interesting, in which they applied the Laser Induced Fluorescence (LIF) to measure the angular distributions of sputtered particles accurately.

Though it's rather difficult to use in the study of sputter deposition process, it should be noted that there is a comprehensive data set of sputtering yields for elemental targets at normal incidence of primary ions [177]. It is the compilation of experimental data, part of which are compensated by the simulation using *ACAT*. Mahan has used this kind of data, and discussed the periodicity of sputtering yield with the atomic weight, as well as the effect of nonlinear cascades [73].

Recently, several calculations have been presented for the selective sputtering phenomena on the alloy / compound targets, including the effects of atomic diffusion [7, 55]. They will be important as the application of those materials becomes major (see also 1.5).

1.2.2 Target roughening during sputtering

The contents of this subsection is rather off-topic from the MC simulation, the main subject of this study, but it has been attracting interests relating to the formation of self affine fractals [6]. Since surface roughening by the ion beam sputtering affects the resolution of the depth-profile measurement in surface analysis, it is also interested by researchers of surface physics and/or chemistry [85]. Surface roughness may also affect the ejection of sputtered atoms, so we will review some reports on this topic here.

Sigmund has also made significant contributions in this field. According to his theory on the sputtering yield mentioned above [135], the primary high-energy particle causes collision cascade at some depth under the surface, and the energy of it is spread in ellipsoidal form. If the energy delivered to the surface by this collision cascade is larger than the binding energy of atoms there, the sputtering ejection occurs. The probability of this ejection becomes larger at positions where the curvature is larger. Hence the random roughness grows up, and more rough surface forms [136].

Using his theory, Bradley and Harper have successfully explained the wavy structure observed on the amorphous materials sputtered by ions with oblique incidence angle in 1988 [13]. Their theory has developed to explain experimental results:

- At suitable incidence angle, flux and target temperature, wavy ripple structure appears

on the surface.

- The 2D wave vector of the ripple structure is parallel to the surface component of the incidence vector of ions, when the incidence angle is small (*i.e.* the nearly normal incidence).
- If the incidence angle becomes larger than some threshold, the wave vector of the structure rotates in 90 degrees, and becomes vertical to the surface component of the ion's incidence vector.

The smaller the wave vector is, the faster the roughness growth is, because of the larger curvature. But the smoothing effect by the surface diffusion is also faster for smaller wave vector structure. As a result of the competition of these two effects, some characteristic wave vector is determined and the structure with it appears on the surface. Applying this model and comparing the growth rate of structures with the wave vector parallel / vertical to the surface component of the incidence vector, it is shown that their relationship inverses at certain incidence angle which agrees with the experimental results above[2]. Mayer *et al.* have carried out the experiment where ions of H, He, Xe, etc. were irradiated onto the SiO_2 surface [80], and showed that the surface roughening and smoothing were well described by the Bradley's model.

Barabási and coworkers have developed the model which includes both the Sigmund's energy transfer model and the curvature dependence of the surface diffusion. With the model, they summarized the ion-induced surface structure into a phase diagram with two parameters: the penetration depth a of the primary ion and the incidence angle θ of the ions [17, 74].

Makeev and Barabási have applied this model to the sputtering of self affine surfaces, and calculated the dependence of the sputtering yield (for secondary ions) on the fractal parameters of the surface. They showed that the yield Y depended on the ion penetration depth a, surface saturation width w and the correlation length ξ:

- $Y \propto w^2$ when $a >> w$.
- $Y \propto w^{-2}$ when $a << w$.
- Y is larger for larger w when $\xi >> w$.
- Y is smaller for larger w when $\xi << w$.

1.3 Particle transport process

As sputter deposition has become popular, problems of it have also been recognized, e.g. the inhomogeneity of the deposition rate on substrate positions, and the generation of convex curvature near mask edges. In addition, it has also been understood that the sputtered particles have much larger energies compared to the particles in vacuum evaporation, and affects the properties of deposited films in various way (see 1.4). Therefore, it has been interested how sputtered particles are transported to the substrate, and what energy, flux and incidence angle

[2]There has been another report using the simulation with discrete model, protesting that the ripple structure appears only in the initial stage of the surface growth, and changes into the self-affine fractals [18]

they reach there with. The Monte Carlo simulation, the main topic of this thesis, is one of these studies.

In this section, we introduce the studies on this particle transport process, except for those using MC method. MC studies will be reviewed in separated section (1.6), and other miscellaneous subjects are covered here: thermalization of particles in the ambient gas, analytical study of the transport process, Direct Simulation of Monte Carlo (DSMC) method for particle transport and experimental methods developed to control them during sputter deposition.

1.3.1 Thermalization of particles

Since the effect of high energy particles came to be known, the behaviour of them have attracted interests. High energy particles generated on the target are decelerated by collisions with sputtering gases. When the energy of sputtered particle becomes comparable to that of gases, the particle is called "thermalized". This process —thermalization— gave one of the most significant motivations to the particle transport study.

In 1981, Sculler *et al.* have calculated how the energy of sputtered particles, ejected with Thompson's EDF, were quenched as they went away from the target for the cases of Nb and Cu sputtering by Ar [83]. After that, they have applied this result to evaluate the degradation of the steepness of Cu/Nb multilayer interfaces induced by the milling of those high energy particles delivered to film surface [129].

Inspired by these theoretical considerations, experiments have been performed to measure directly the velocity distribution of particles in the plasma. Ball and coworkers have performed this for Cu/Ar sputtering plasma by observing the Doppler's shift of the atomic emission line from Cu in 1986 [5], and Park *et al.* have done for Fe using laser induced fluorescence in 1991 [104]. The mean energy and the proportion of the thermalized particles were given as functions of the product of the distance and the gas pressure. These studies gave an strong influence on the development of the MC simulations.

For the origin of high energy particles and the evaluation of their energies, comprehensive review has been submitted by Winters, Eckstein, and others [168]. When impinging ions are neutralized and recoil on the target surface, they have very high energy so that they cause major effects on the film. Window stated that heavy gas (Xe, Kr) should be used to reduce these effects, and proposed the static system without the flow of expensive gases in the production system [166].

1.3.2 Analytical calculation

To evaluate the thickness profile in sputter deposition, analytical calculations were developed at first ([161] pp.115). In these, deposition rate was obtained by integrating the flux from each part of the source of sputtered particles. The intensity distribution of the source was taken to be proportional to the depth profile of the erosion track. Then the flux was given by the product of the source intensity and the solid angle of the source from the substrate, the latter of which was calculated from the distance and the angle between them. Introduction of the computer has made this calculation applicable to any form of the chamber and the erosion track [142].

The scattering of sputtered particles by gas has come to be considered since late 1970's. For example, Wu *et al.* have elucidated the deceleration of high energy particles from their mean free path (MFP), and evaluated the damage brought to the film surface during the deposition of Nb_3Ge superconducting films [171]. Westwood has noticed that the experimental thickness profile and/or the form of the curvature at the mask edge show the discrepancy from the calculation, and has proposed the model where sputtered particles move diffusively after they travel certain distance from the target [163]. Keller *et al.* have indicated that the transfer to the diffusive stage was dominated by the product Pd of gas pressure P and the target–substrate distance d, and lead the expressions which determined the high-energy flux and the diffusive flux [63]. These have been confirmed by Drüsedau *et al.* in 1998 [29]. They used several sputtering chambers and measured pressure dependence of deposition rate for Al/Ar and Si/Ar, which were well described by Keller's expression. They also measured deposition rates for combinations of 4 gases and 7 targets, and stated that the prefactor of Pd, which determined the flux decrease, was affected by the atomic mass ratio between the gas and the target elements.

The MC simulation followed these studies by Wu, Westwood and Keller, and becomes dominant in this field. However, analytical methods have still been used by several groups. For example, diffusive process was treated by solving the diffusion equation with cylinder boundary [109], and the composition of the high-T_c superconducting film was evaluated with different geometry of target and substrate, considering the angular distribution of the sputtered particles [67].

1.3.3 DSMC method

Direct Simulation of Monte Carlo (DSMC) has been developed by Bird and others to treat the rarefied gas flow [8]. In this method, the considering volume is split into cells as small as a half of the MFP, where some thousands of representative particles are manipulated assuming the Boltzmann's distribution. And then, temperature, density and particle flux are obtained in each cell. This method has been applied to the transport process of sputtered particles since early 1990's, and several reports were submitted.

In 1993, Urbassek *et al.* have applied DSMC to Cu/Ar sputtering, and obtained profiles of temperature, density, pressure and velocity for both Ar and Cu [156]. But their results showed the higher gas density near the target, which did not agree with the experimentally observed "gas rarefaction" by Rossnagel [115, 116, 122], so the validity of their calculation was rather questionable.

Kersch *et al.* have reported the simulation study on Ti/Ar in 1994, using DSMC and TEPA [64]. The latter method was the derivative of the MC simulation, assuming certain temperature / density profiles of Ar. DSMC and TEPA did not agree well, and it was also difficult to determine which was valid, since experimental result was not shown. In their TEPA calculation, the VHS (Variable Hard Sphere) and M1 interatomic potentials were used, which was rather scarce in MC simulations.

In 1999, Dosa and coworkers have applied DSMC to the simulation of Ar gas flow in the large size sputtering chamber [28]. They only treated the flow of supplied Ar, and not the sputtered particles. But the Ar gas density profile is an important parameter for MC simulation, so it is going to be taken into account in the future.

1.3.4 Directional sputtering and Ionization sputtering

Since 1990's, as characteristic dimensions of semiconductor devices shrink, metalization of trench structure of high aspect-ratio has been required with void-free dense films. It is difficult for normal sputtering technique since the incidence angle distribution of arrival particles is so scattered that overhangs are generated at the entrance of trenches and blocks the further deposition at the bottom of them. To solve this, so-called "directional sputtering" and "ionization sputtering" techniques have been developed mainly by Rossnagel and coworkers at IBM [114, 117].

Collimated sputtering is one of the directional sputtering, proposed by Rossnagel in 1991 [121]. In this method, the array of tubes (=collimator) is located between the target and substrate. In his case, each tube was 5 mm in diameter and 20 mm in length. Though it was demonstrated that trenches with aspect ratio as large as 1:3 were filled well, it has not widely been used because the droplets grow on the collimator in relatively short deposition time [117].

Long throw sputtering is an another kind of directional sputtering, where the substrate is located far away from the target, to converge the incidence angle of particles to surface normal and improve the trench filling characteristics. It is known that the reduction of gas pressure decrease the scattering of particles, and more sputtered particles directly reach the substrate [19]. Moreover, in long throw sputtering, the target–substrate (T–S) distance is increased and the angle subtended by the ring-like evaporation source (erosion track on the target) at the substrate is reduced. By generating the discharge at as low as $10^{-1} \sim 10^{-3}$ Pa and increase the MFP, it is insisted that the sputtered particles arrive at the substrate preserving its initial direction at the target[3]. Motegi *et al.* at ULVAC Corp. have deposited Ti, TiN and Al alloy under the pressure of 0.04 Pa and T–S distance of 31 cm, and obtained the bottom coverage[4] of 50 % for the hole with 1:2 ratio [89]. Mayo *et al.* have studied this technique both experimentally and theoretically [81]. Their conditions were T–S distance of 30 cm, gas pressure as low as 0.1 Pa, and target / substrate diameters of 30 cm and 20 cm, respectively. They compared the side / bottom coverage of experiment and calculation, and indicated that long throw sputtering had the advantage on side wall coverage.

Ionized sputtering [47] has proposed also by Rossnagel and coworkers in 1993. In this method, RF coil is inserted between the target and substrate to enhance the ionization of sputtered particles there. Then the direction of these ions are controlled by applying the bias to the substrate. In their first paper, they located the thickness monitor behind the grid electrode, and evaluated the ionization percentage by comparing the deposition rate with or without the repelling bias. When magnetron power was $1 \sim 3$ kW and the coil power was $100 \sim 1000$ W, $50 \sim 90$ % of ionization efficiency was observed under 4.7 Pa [119]. In this condition, the substrate was inserted and the bias voltage ($20 \sim 40$ V) was applied to it. For contact holes with aspect ratio of $5 \sim 6$ on the substrate, bottom coverage of 50 % was obtained [120]. They also simulated the deposition process in this method, and reproduced well the deposition profile inside the trench, considering the resputtering effect, sticking probabilities, and angular distributions of incident neutrals / ions / ambient gas ions [40]. There have been some attempts to extend the ionization sputtering: Magnets were arranged to form a multipole magnetic configuration

[3] But the MFP is still some centimeters in length, and much shorter than the T–S distance in these pressures.

[4] "bottom coverage" means the ratio of the deposition rate at the bottom of the trench or of the hole, compared to the substrate surface outside of them. "side(wall) coverage" is also defined as well.

around the RF coil which improved the ionization efficiency [159], or some hundreds gauss of magnetic field was applied to penetrate the RF coil to form helicon wave[5] in the plasma [160]. The latter is called "helicon plasma sputtering" by several groups, and has been applied to the production of optical multilayers of Si $_2$/TiO_2, which show the well defined interfaces [40].

1.4 Processes on film surfaces

In sputter deposition process, high energy particles arrive at the film surface and cause various phenomena there, as already mentioned above several times. These effects were noticed by many researchers in early 1980's, when the sputter deposition had become popular by the development of magnetron sputtering apparatus. Since then, many experimental studies have been reported about the film properties deposited by sputtering. These knowledge was summarized and shared at the end of 1980's.

In 1990's, as the performance of the computer improved and the simulation methods (such as molecular dynamics) were developed, simulation of the growth process of sputtered films has been studied by several groups. These studies were enhanced by the requirement from VLSI industries, in which trenches and holes with high aspect ratio must be filled and metallized by the sputter deposition.

In this study, our goal is not to simulate the detailed properties of deposited films, but to obtain frequency, energy and angular distributions of arrival particles. However, we believe that it is meaningful to review here the growth process of sputtered films and effects of high energy particles on it.

1.4.1 Experimental studies

As described above, it was known in the beginning of 1980's that high energy particles brought significant effects to film properties. Moreover, it was also noticed that applying the bias voltage to the substrate changed the film characters: incorporation of discharge gases (e.g. Ar), film stress, density, electrical conductivity, and so on.

Ziemann and Kay proposed a measure "normalized energy" to explain these phenomena [179]. It is the energy delivered onto the film surface per depositing atom. To study the effect of this parameter, they prepared the Pd film with dual ion beam sputtering system. It was shown that normalized energy well described the variation of film properties: the gas (Kr) incorporation, lattice distortion, grain size, orientation and electrical conductivity. Just after their study, Hoffman have reported the dependence of film properties on gas pressure, discharge current and substrate position. It was concluded that their behaviors were described qualitatively by the concept of normalized energy.

In 1985, Kay and coworkers have also used the dual ion beam apparatus for Ag, and showed that the change of film orientation was dominated by the competition between strain energy and the surface energy: the former was originated from the biaxial stress generated in the film volume, and the latter was dependent on the lattice face appeared on the film surface [51]. They

[5] About helicon wave in the plasma, see [108] for example.

have also confirmed this phenomenon for sputtered Ni films deposited by conventional sputter deposition using Ar discharge plasma [62].

For the structure of sputter deposited films and their dependency on the process parameters, Thornton's zone model [148] has generally been accepted since 1980's. It takes the gas pressure and the substrate temperature[6] as parameters, and categorize the region into 4 zones (Zones 1, T, 2 and 3), each of which have characteristic microstructures. Thornton has discussed the relation between this model and the effects of high energy particles, and explained why these zone structures were grown in respective conditions [147].

In 1989, reviews of these experimental results have been compiled independently by Mattox [79] and by Rossnagel [118]. Both have summarized the phenomena by normalized energy, and become the standard way to understand the growth of sputtered films. They mainly treated the sputter deposition using plasma discharges, where the high energy particles were originated by:

- ions accelerated by the plasma sheath near the substrate, which are affected by the substrate bias (mostly charged positive)
- atoms / molecules sputtered from the target (electrically neutral)
- primary ions bombarding the target which are neutralized by the charge exchange process there, and recoil (neutral)
- negative ions generated near the target, and inversely accelerated by the cathode's potential drop (negative charge)

These high energy particles affect the deposited films in various way including:

- desorption of adsorbates on film surface
- secondary electron emission, which may affect the chemical process at the surface
- resputtering of surface atoms and redeposition of them
- enhancement of surface diffusivity of adsorbed atoms
- increase in nucleation density by the introduction of surface defects
- implantation of high energy particles into films
- recoil implantation of surface atoms into films
- lattice defects caused by the collision cascade generated underneath the surface
- increase surface temperature

[6] more accurately, the ratio of substrate temperature and the melting temperature of the film.

These primary events then caused changes in grain size, defect density and internal stress, which were summarized as a function of normalized energy. We cannot go into the detailed discussion here, but can roughly summarize that "moderate normalized energy brings good effects to the films, but too high energy affects rather badly".

It should be worth to mention here, that the stress in sputtered films has thoroughly been reviewed by Windischmann in 1991 [164] and 1992 [165], including the mechanisms of the stress generation for both tensile and compressive cases, and the compilation of vast of experimental results. Hoffman has also discussed the stress transition between tensile and compressive [46], relating to elements of gases and targets, deposition rate, substrate angle, etc.

1.4.2 Simulation studies

As the general understanding for the effect of high energy particles has been common, simulation studies of the film growth process with high energy particles appeared in late 1980's.

Müller have applied the molecular dynamics (MD) method to the simulation of sputtered films in 1987 [95]. He arranged atoms randomly on the substrate, and supplied additional atoms from the above of it. Lennard-Jones interatomic potential was used for the pair of atoms composing the film, and Moliére potential was used between the bombarding high energy particle and the film atom. Atoms just above the substrate were fixed, which meant the substrate temperature of zero. The result of the simulation showed tensile stresses in any condition. The strength of the stress increased as energies of depositing atoms and/or the high-energy particles increased, took a maximum at a certain energy, and decreased after that. When the energy was nearly zero, film structure became columnar because of the shadowing effect. Near the peak of the stress, these columns coalesced and caused the tensile stress by the mixing of atoms.

In 1993, Fang *et al.* have reported the MD simulation also [34]. It was based on the Müller's, but more realistic modeling was developed and applied. Their model could account for the gas incorporation into the film, so that the generation of the compressive stress could be reproduced [33]. In the second report, they used the MC simulation to obtain energy and angular distributions of incoming particles.

Apart from these MD simulations, a group of Smy, Tait and Brett has developed the simulation code called *SIMBAD*. It simulated more macroscopic film growth. Initial model was rather simple, where disks were incident at certain angles, rolled on the surface, found energetically preferable place and located there. Despite of its simplicity, the film structure near the substrate step and the density profiles were well reproduced [23, 138, 143, 144]. This *SIMBAD* was combined with the MC particle transport program, *SIMSPUD*, and was modified to use the energy and angular distributions calculated with it [22, 24]. Independently, their group has developed the grain growth simulation program called *GROFILMS* applicable to sputtered polycrystalline films [35]. This method handled the surface / interface diffusion of atoms on / between the grain(s), as well as the flow of atoms by bulk diffusion between grains, through the motion of the linear nodes representing each crystalline. It has been applied to the growth of sputtered Cu on the trench structure of Ta/SiO_2, and successfully reproduce the cross sectional structure of experiments [36, 37].

Through these studies, the importance of the energy / angular distributions of incident particles have been recognized to simulate the sputtered film growth. Therefore, some attempts

have been submitted to combine the particle transport simulation with that of the film growth process. They include the reports by Smy and Fang mentioned above, a study by Hoshi and coworkers [49] which applied the Henderson's rigid sphere model [44], and that by Ohta *et al.* [102] which used the Leon's model [68] where the surface motion was accounted as the viscous flow to minimize the surface energy.

1.5 Stoichiometric deviation in the sputtering of compounds

Sputtering deposition has also been widely used for alloys and compounds including magnetic / dielectric / superconducting materials [161]. It is critical to control the film composition for the properties of these materials, but it frequently deviates from that of the target. In this subsection, the studies on this compositional deviation are summarized. Reactive sputtering method has also been used generally to prepare compound films, where some of elements consisting the film are supplied as a reactive gas. But it is out of the scope of this study[7].

Since the discovery of High-T_c superconducting materials in the midst of 1980's, many groups have reported the preparation of the film of it by sputtering. The compositional deviation problem has also been recognized since the early stages of them, and the "off-axis sputtering" method has been proposed [32, 145], where the substrate did not face to the target but was inclined or was even located vertically to it. It was found that this method actually decreases the extent of the deviation. The reason of the deviation were thought to be electrons and/or negative ions generated near the target, which were accelerated by the cathode potential, hit the substrate and caused selective resputtering or desorption of particular element [174]. The dependence of the deviation on the pressure (P) [97] and target–substrate distance (d) [127] showed that the deviation decreases as the P and/or d increases. It was explained that the high-energy particles were blocked by the scattering with ambient gas atoms [38].

Apart from these discussions that ascribed the deviation to substrate reactions, there have also been reports that consider the difference in scattering process by gases due to the mass difference between elements [172, 173]. It has been considered in the study by Rossnagel *et al.* [123], where they study the pressure dependence of the film composition of metallic alloys e.g. AlCu and WTi. They deposited films between 5–30 mTorr, and found the minimum of the concentration of lighter elements at the intermediate pressure. They explained this by the transition of the transport process from ballistic to diffusive. In the both low and high pressure extremes, the difference in the element does not appear, while in the midst of them, lighter atoms are backscattered by ambient gases, and deplete more in the film. We also have observed the depletion of lighter elements with pressure increase at LaB_6 deposition [59], and discussed the effect of the scattering of lighter boron [65].

Moreover, selective sputtering at the target [178] has also been discussed. However, it cannot make the deviation by itself if the enough time of pre-sputtering is performed before the deposition, and if the diffusion of elements in the target is not so significant [169].

[7] For more description of this method, see section IV in [105], for example.

1.6 Monte Carlo simulation of particle transport processes

As described in preceding sections, particle transport process during the sputter deposition is significantly important for deposited films. It dominates the thickness profile of the film, and also affects film properties through the energy / angular distributions of incident particles.

However, it is not so easy to model the transport process and to reproduce the experiment. It comes from two reasons. Firstly, each sputtered particle collides with gases, be scattered by them, and changes its energy and direction until it reaches the chamber wall. Therefore, simple geometrical calculation is not valid as in the case of vacuum evaporation. Secondly, sputtered particles ejected from the target have energies of some electron volts, which are much higher than the thermal energy of ambient gases [146]. Hence the transport of particles has the strong directivity initially, and cannot be treated as the simple homogeneous diffusion.

To simulate this problem, Monte Carlo (MC) method has been proposed in the midst of 1980's. It assumes probability functions for various processes that particles experience during the transport, which construct the Markov chain. It traces $10^5 \sim 10^6$ of trial particles, and statistically obtains the distribution of arrival positions on the chamber wall and the energy / angular distributions of particles at each positions.

In this section, we review historically the development of this method. The model generally accepted at the time of writing will be discussed in sections from 2.2 to 2.4 of the next chapter. Applications and the latest developments of the MC method are also introduced.

1.6.1 Early developments of MC simulation

The reports by Somekh in 1984 [139] and by Motohiro *et al.* [91–93] in 1983–1984 may be the earliest ones which apply the MC method to the particle transport. In this subsection, we describe their studies in some detail.

Somekh has been motivated by the damage of films brought by high energy particles originated from the target, and simulated the deceleration process of these particles in the gas atmosphere. His assumptions were:

- Energy of sputtered particles was ruled by the Thompson's formula [146] and that of (neutralized and) recoiled ions obeys the Kaminsky's formula [60]. Angular distribution of the sputtered particles was assumed to be over-cosine distribution measured by Patterson *et al.* [106].

- In the collision process with gases, differential scattering cross section proposed by Robinson [113] was used to determine the scattering angle from the collision parameter. Total cross section σ was obtained by linearly approximating the Robinson's data. The mean free path $kT_g/P\sigma$ was deduced from it, and respective free paths were yielded using Poisson's distribution.

- Gas atom was assumed to be stationary on collision.

- Only elastic collision was treated. The direction and the energy of the particle were calculated from the scattering angle.

In his model, cross section of the collision was dependent on the particle energy. As the energy increases, the cross section became smaller. As a result, the deceleration distance became longer than the case where the cross section of the thermal energy region was assumed. It was also pointed out that high energy particles affecting film properties were mostly recoiled ions when the Pd (gas pressure P times the target–substrate distance d) was as large as $10 \sim 500$ Pa mm.

The report by Motohiro *et al.* have treated sputtered particles only. In their initial studies [91–93], the Thompson's formula was used for energy distribution, and cosine rule was used for angular distribution. Ambient gases were assumed to be immobile as Somekh's model, and rigid sphere model was applied for the collision between the sputtered particle and the gas atom. Each radius was determined by interpolating the values obtained from the viscosity of their gas. Using this model, they deduced the probability of the sputtered particle from the target to arrive the substrate facing to it (ν_A) as well as to be back and redeposit onto the target (ν_R) as functions of Pd. In the case of Ag and Pd is more than 0.1 Torr $\cdot$ cm (1.34×10^2 Pa mm), it was indicated that ν_A became almost zero, ν_R saturated at 0.5, and the rest of particles were thermalized in the atmosphere. The deceleration process of the particles and the angular distribution of them at the substrate were also discussed. Their assumptions in these reports were rather simple compared to Somekh's.

Motohiro's paper in 1986 [90] was greatly improved, in which he compared the simulation with experimental results of thickness profiles of Ti sputtered by Ar. The disk form substrate holder was dangled above the target, and pressure dependence of thickness profiles of the holder, front and back sides from the target, were measured. In MC model, both the rigid sphere model and the potential scattering model were used. In the latter, Born-Mayer interatomic potential was adopted, and Abrahamson's potential parameters [1] were used. This potential decreases exponentially as the distance increases, hence the "cross section reduction" effect proposed by Somekh was incorporated implicitly. This potential was chosen since it was more similar to the result of Gaussian 80 compared to the Robinson's pair potential used by Somekh. The Thompson's distribution was used for the energy of sputtered particles. Three types of angular distributions; $\cos\theta$, $\cos^3\theta$ and $\sin 2\theta$ were tested as the angular distribution. Gases were also assumed to be stationary. In high pressures, the sputtered particle collides with gases many times and their energy may become lower than that of gases, where the assumption is not valid. In this case, he assumed that the motion of the sputtered particle became the random walk. The mean free path of this random walk was determined from the thermal radius of the gases, considering the factor of $(1 + m/M)^{-0.5}$ which came from the gas motions. Mainly because the computer performance, this random walk was limited as many as 50000 collisions, and the particle which could not reach the chamber wall until then were thought to be lost. As a result of the simulation, they concluded:

- The result using $\sin 2\theta$ angular distribution showed the best agreement with thickness profiles of the experiment.
- Significant difference did not observed between the result with rigid sphere model and that with potential scattering model.
- The discrepancy between the simulation and the experiment became considerable at pressures more than 5×10^{-2} Torr.

1.6.2 Effects of the thermal motion of gases

As appeared in the report by Motohiro in 1986, it had been recognized that the decelerated particles with many collisions, *i.e.*, thermalized particles, was dominant in high pressures, where the stationary gas assumption was not valid. For example, the experimentally observed energy distribution of sputtered particles by Ball *et al.*[8] did not agree well with the theoretical one by Westwood [163], which used the resemble method with Somekh's simulation.

Motivated by this, Turner and coworkers proposed the method to incorporate the thermal gas motion into the MC simulation [153]. Taking the thermal velocity distribution of gases into account, mean free path of the sputtered particles becomes shorter (e.g., even the particle with zero speed may be collided). Note that this effect overlaps with the reduction of the collision cross section at high energies which extend the MFP. The MFP of the particle in the gas with Maxwellian has been given by Jeans [56] as a function of the particle speed, which was used in their study. On collision, the gas speed was determined randomly assuming the gaussian with FWHM of $2\sqrt{kT_g/M_g}$ for each component of x, y and z. Other processes were modeled almost in the same way with Somekh's and/or Motohiro's; Thompson's formula and cosine distribution were used for the ejection of particles from the target. Lennard-Jones potential was chosen for the scattering potential. Cu-Ar, Cu-Xe and Cu-Kr cases were studied. They calculated the distribution of velocity components both parallel and vertical to the target surface, and discussed their dependence on the gas pressure and the distance from the target. The mean speed observed from the side of the chamber were also calculated, which agreed fairly well with the experimental results by Ball *et al.* [5].

With this paper by Turner, the framework of the MC simulation was completed as used in these days. As the computer performance improves, the MC simulation of sputtered particle transport, using their models, has come to applied widely since then.

1.6.3 Applications of MC simulation

Because of the detailed description of the simulation method by Motohiro, and the establishment of the reasonable treatment of low energy region by Turner, many applications have been reported since the beginning of 1990's.

Several MC studies were already performed before the Turner's study, including the discussion of the edge effect of the mask in ion beam sputtering system [41], the evaluation of the dependence of particle energies on hydrogen partial pressure in the reactive sputtering of a-Si:H using Ar-H_2 gas mixture [157], and the study of the energy and angular distributions of arrival particles at the substrate for Si/Ar sputtering [43]. Elsing has been developed the MC simulation independent of Somekh, Motohiro and Turner in 1991 [31]. His model was almost identical with theirs, but simpler assumptions were used for the ejection from the target. It should be noted that he took into account the inclination of the target normal caused by the formation of the erosion track, when ejection angle of the sputtered particles were deduced. Some results of calculation were shown for Ti/Ar system.

Turner *et al.* have also been presented some reports themselves. In 1990, they discussed the dependence of the Cu concentration in YBCO superconducting films on gas pressure and

[8] mentioned in 1.3.1

T–S distance [155]. In 1992, they chose several elements which have a variety of binding energy (BE) and atomic mass, and simulated pressure dependence of their thickness profile, arrival angular distribution, mean energy and energy distribution for Ar sputtering [154]. The elements include: C, Nb, W (high BE), Si, Pd, Au (medium BE), Na, Cd, Pb (small BE). Furthermore, in 1995, they applied the MC simulation to evaluate the gas rarefaction effect [115] proposed by Rossnagel *et al.*By splitting the chamber space into meshes and calculating the energy transfer from the sputtered particle to ambient gases, they obtained and displayed the gas temperature profile and its dependence on target elements, discharge current and voltage [152].

Nanbu *et al.* have also used MC simulation and discussed the effect of target power and gas pressures [99], as well as the pinhole filling in case of the collimated sputtering [42].

Tuda *et al.* have applied MC method to interpret the experimental result of the trench filling with $(Ba, Sr)TiO_3$ in 1994 [151]. Though the simulation was performed only for Ti/Ar and the simple hard sphere model was used without the change in its radius by energy, the experimental results were reproduced fairly well where the side wall coverage in the shallow trench increased with increase in gas pressure ($0.1 \rightarrow 10$ mTorr).

In 1995, Eisenmenger-Sittner *et al.* have compared the angular distributions of the sputtered particles at chamber wall obtained from MC simulation and experiment, for the axisymmetric magnetron sputtering system which has the target inside [30]. They assumed that the gas atoms were stationary. They reported that they had to modify the angular dependence of particle ejection (the n of $\cos^n \theta$ distribution) as the gas pressure changed to fit experimental data.

Though some of the contents were already mentioned in 1.4.2, we would like to show here several reports again which combine the film growth model on the substrate with the particle transport process. They have appeared since the midst of 1990's.

The group of Smy, Dew and others have developed the simulation code, called *SIMSPUD / SIMBAD*. The former is the MC simulation treating the particle transport, and the latter is the one to simulate the film growth. *SIMSPUD* has been proposed in 1994, based on the Somekh's model. They used this *SIMSPUD / SIMBAD*, and indicated that good agreements were obtained with experiments for trench filling [24] and for collimated sputtering [22]. Lin and Cale also used their method, and calculated the thickness profile on the substrate which located behind the hexagonal collimator [70].

Ohta *et al.* have proposed the simulation method which uses the viscous flow model of Leon [68] for the atomic diffusion process on the substrate, and calculated the thickness profile inside the contact hole embedded in the substrate [102]. Agreement with experiments was good under 1 Pa, but became poorer at higher pressures than that.

1.6.4 Extensions of MC simulation

Proposals to extend the MC method have also been reported since the study by Turner. In this subsection, we would like to review them in the historical order.

In 1991, Myers, Ruzic and coworkers have used their *fractal TRIM* simulation code [124,125] to calculate the energy and angular distributions of sputtered particles, instead of using the Thompson's formula and cosine distribution [98]. Van der Waals potential with r^{-6} dependence was used for the scattering potential, and the motion of Ar gases were neglected. They applied

the simulation to the Si/Ar sputtering with the disk target and the rectangular chamber. As the gas pressure increased, thermalized particles increased and the high energy flux of Si atoms decreased at the substrate. They did not discuss the difference between the simulation with *fractal TRIM* and that with Thompson's formula.

Avaritsiotis *et al.* have applied the MC simulation to the reactive sputtering in 1992 [3]. They incorporated the absorption process of the reactive gas, and deduced deposition rates and film compositions at various positions on the substrate.

The report by Yamamura *et al.* in 1995 have also used the simulation inside of the target, to obtain the ejection parameters of sputtered particles [175]. For Cu/Ar sputtering, they applied their *ACAT* code [176] and calculated angular / energy profiles for both sputtered particles and the neutralized / recoiled high energy Ar atoms. It was indicated that the result of *ACAT* code differed significantly from those of Thompson's formula and cosine rule. For the scattering potential, they proposed the Thomas-Fermi-Morse potential which was obtained by adding the exponential term to the Thomas-Fermi potential to fit the Morse potential.

In the same year, Stache has proposed a method to treat the thermalized transport with diffusion equation, which were solved by finite element method [140] to reduce the computational complexity. In his method, both target and substrate were assumed to be the infinite plane, and the thermalized position of particles were recorded by the relative coordinate from the ejection position. They were superposed with the weight of the depth of the erosion track at the target, and the profile of thermalized position of particles were obtained. It was treated as the source of particle in the diffusion equation. The calculation results were compared with experiments for Si/Ar sputtering, and good agreements were obtained for pressures of 1 Pa and 10 Pa.

Bogaerts have studied the profile of thermalized position of sputtered Cu atoms for Cu/Ar sputtering in 1995 [12]. He intensively discussed the effect of interatomic potential, and compared the result using Molier potential with those using power law potential with orders of $1 \sim 4$. At 100 Pa, the peak of the thermalized profile came to about 0.05 cm from the target with Molier potential, while it went much further in the case of the power law potential with order 4.

In 1996, Malaurie *et al.* have compared the thickness profile of simulation and experiment for Cu, Ti, Al, etc. in the axisymmetric sputtering chamber [75]. In their simulation, they introduced the ellipsoid-like ejection angle distribution:

$$g(\theta) = b\frac{2\alpha^2 \cos\theta}{1 + (\alpha^2 - 1)\cos^2\theta}, \tag{1.1}$$

where b was the major axis of the ellipsoid, and α was the ratio of b with the minor axis a. By comparing with the experiment, $\alpha = 1$ (*i.e.* cosine rule) was optimal for Cu, and the undercosine values of 1.75 and 2.5 were good for Ti and Al, respectively. These optimal α's did not depend on the gas pressure nor the T–S distance. In the case of Ti-Al alloy, $\alpha = 2.5$ reproduced well the experiment for both elements.

In the report by Serikov *et al.* in 1996 [130], they have proposed a method in which the flow field of the ambient gas is deduced by DSMC[9] at first, and the MC simulation based on the Turner's method was performed. They have developed this model further, and proposed the particle-in-cell / Monte Carlo (PIC/MC) method in 1997 [131]. In this hybrid method,

[9] mentioned in 1.3.3

the chamber was split into cells, and the energy brought into them by the sputtered particles were deduced using MC simulation. Then the energy flow between cells was solved by the finite different method. This procedure was iterated until the thermal profile converged.

In 1997, Smy *et al.* have discussed the treatment of sputtered particles redeposited onto the erosion track [137]. In high pressure environment, sputtered particles experience many collision nearest the target, so the redeposition occurs frequently. They explained that the net of the ejected particles, including these redeposited ones, should be proportional to the depth profile of the erosion track, or the match between the simulation and the experiment became worse in high pressures. They also showed the result treating the particle transport only by FEM where the ejection flux of particles were proportional to the erosion depth, but the result did not agree with the experiment well.

Bogaerts *et al.* have proposed the method to combine the MC with the FEM treatment of the diffusion process in 1998 [11]. They applied it to Li/Ar. Using laser absorption experiment, spatial profile of Li atoms were measured. And the simulation was performed by changing the sticking coefficients on the chamber wall to fit the result with the experiment. However, the agreement between them was rather poor.

1.7 The goal of this study

In previous studies, gas atoms / molecules were treated as immobile, since the sputtered particles have energies much higher than that of gases initially. Nevertheless, these sputtered particles are decelerated as low as thermal energy of gases (*i.e.* "thermalized") with less than 10 times of collisions. Hence as the pressure increases and the mean free path becomes shorter, most of particles are thermalized before they reach the chamber wall. We believe this is the reason why the accuracy of the simulation becomes worse in high pressures.

Turner's model is properly incorporate the effect of the gas motion for mean free path, but still assumes that the velocity distribution is independent on the speed of the sputter particle. It is not valid as you can see by considering the coordinate on the sputtered particle in the velocity space. For example, when the particle speed is high enough, most of the gas collides from the forward of the particle. Since the scattering direction is significant in the MC simulation, it is desirable to treat this effect accurately.

The further pressure increase brings more scattering events, hence much more calculation time is needed. After the thermalization, however, the motion of the particle is well described by the random walk, so the ensemble of them can be treated by the diffusion equation with the source term constructed by thermalization points of particles. By combining the MC simulation and the diffusive treatment, the calculation time should greatly be reduced.

Summarizing, we would like to develop the models that can be applied to the MC simulation:

- We deduce the distribution of colliding gas velocity and its dependence on the particle speed by considering the kinetic theory of gases.

- We propose the method to account thermalized particles with the diffusion equation, and try to reduce the computational complexity. It will compared with the MC method to check the validity, and combined to it after that.

The developed model will be applied to the high pressure sputter deposition process. We will check how well the simulation reproduce the experimental results, and discuss the origin of some phenomena observed experimentally in high pressure environment.

Chapter 2

Theory

In this chapter, we discuss physical backgrounds of the particle transport simulation. We skip the detailed description about the implementation of the simulation program here, which will be given in appendix A. In the following, we assume that the sputter deposition system is axisymmetric for simplicity, while our discussion can be extended to 3-dimensional system easily.

In the Monte Carlo simulation of the sputtering process, we assume that the "life" of sputtered particles can be treated as the Markov process[1]. The life includes ejection from the target, the collision and scattering by the ambient gas atoms/molecules, and deposition on the chamber wall. To execute this simulation, we need probability functions for these steps. We prepare them (e.g. $f(x)$ for variable x) before the simulation, and use them to determine x with the pseudo-random number w generated by the computer. Normally, w distributes uniformly between $(0 \leq w < 1)$.

Using these functions, we track down $10^4 \sim 10^6$ particles, and stochastically obtain the particle flux onto the chamber wall (including substrates), as well as energy and angular distributions of those particles.

In the first section of this chapter, we briefly explain how to determine the parameters (*i.e.*, x) in each Markov process of the Monte Carlo (MC) simulation. Three sections follow, where the physical models of MC methods are discussed in the sequence: ejection, collision and scattering, and deposition. These have been proposed by previous works, reviewed in sections 1.6.1 and 1.6.2. The last two sections are the discussion of methods we developed in this study. In section 2.5, we extend the collision model to take the thermal gas motion into account. And in the final section, we discuss the treatment of diffusive transport of thermalized particles using the diffusion equation and boundary element method.

2.1 Concept of the Monte Carlo method

In this section, we discuss how to determine the parameter x at each Markov process, from its given probability function $f(x)$. Two methods are generally used. The first one is called "acceptance-rejection" technique. This is generally used when the analytical integration of $f(x)$

[1] In this stochastic process, the probability f_i, for which the system in status q_0 at time t_0 becomes q_i at $t + \delta t$, does not depend on the history of the system before t_0 but only on the status q_0 itself.

is impossible. Before the simulation, you have to determine the value f_{sup}, which is larger than the maximum of $f(x)$ between $x_{min} \leq x \leq x_{max}$. On simulation trials, two independent pseudo-random numbers w_1 and w_2 are generated between the range $[0, 1)$, and are tested whether they satisfy the following conditions at the same time:

$$x_r = x_{min} w_1 + x_{max}(1 - w_1) \tag{2.1}$$

$$w_2 f_{sup} \leq f(x_r) \tag{2.2}$$

If both of them are true, x_r is used as the result of this trial. If any of them is false, another two random numbers are generated and tested.

The second method uses the relation:

$$w = \frac{\int_{x_{min}}^{x_r} f(\xi) d\xi}{\int_{x_{min}}^{x_{max}} f(\xi) d\xi}. \tag{2.3}$$

If $f(x)$ is analytically integrable, and if the primitive function of $f(x)$ can also be solved analytically, you can directly calculate x_r from eq. 2.3. It is preferable generally from the viewpoint of the calculational complexity.

You can still use the second method even if the analytical root of the primitive function of $f(x)$ cannot be obtained. You can solve the eq. 2.3 numerically using Newton method, bisection method, etc. It's difficult to determine which method to use in this case. It depends on the probability of the rejection in "sampling and rejection" method and on the expected number of iteration required to solve the equation 2.3 with satisfactory precision.

2.2 Particle ejection from the target

Each MC trial starts from the ejection of the sputtered particle. In this section, methods to determine its position, energy and angle are explained in corresponding subsections.

2.2.1 Ejection position

We consider the axisymmetric system in this study, and the target has disk form. Ejection point of the sputtered particle from the target is determined so that the probability of the ejection is proportional to the removed volume of the target there. The removed volume is calculated from the depth profile of the target erosion track actually measured after sputtering experiments. If we measure the depth $d_T(r)$ of the target at radius r from the center of the target, probability density function of the ejection point $P(r)$ is:

$$P(r) \propto r\, d_T(r) \tag{2.4}$$

At higher pressures, re-deposition of the sputtered particles onto the erosion track becomes more significant. In the simulation, these particles should be re-ejected immediately from there, or the depth profile of the simulation will be differ from that of the experiment [137].

2.2.2 Energy distribution

For the energy distribution function (EDF) of sputtered particles, we use the Thompson's formula, which has been widely accepted and used in various sputter-related simulation studies. He actually measured the EDF for several poly-crystalline metal targets, and found that the high-energy tail of those EDF's decreased inversely proportional to the square of the particle energy. He then proposed this EDF formula to explain these trends. In the following of this subsection, we try to follow his paper [146] and deduce this formula.

Firstly, we consider the collision cascade occurring in the bulk of the sputter target, and derive the flux of particles through an arbitrary plane. The flux $\Phi'(E', \boldsymbol{r}')$ with direction $\boldsymbol{r}'$ and energy E' is:

$$\Phi'(E', \boldsymbol{r}')dE'd\Omega' = v'\rho(E', \boldsymbol{r}')\frac{\cos\theta' d\Omega'}{4\pi}dE', \tag{2.5}$$

where v' is the speed of the particle with energy E', and θ' is an angle between the normal of the plane and $\boldsymbol{r}'$.

There should be particles which act as the source of such a collision cascade. We now introduce the energy density $q(E_2)$ of such particles with energy E_2. We also introduce the collision frequency $\nu(E_2, E')$ of these, where their energy decreases from E_2 to less than E'. Using these, the spatial density of particles which are decelerated below E' in unit time is given by:

$$\int_{E'}^{\infty} q(E_2)\nu(E_2, E')dE_2 \tag{2.6}$$

The reduction rate of the kinetic energy of the particle at E' in unit time can be expressed as dE'/dt. This can be rewritten as $v'\,(dE'/dx)$ using the particle speed $v' = dx/dt$, hence we can deduce the relation

$$dt = dE'\left\{v'\frac{dE'}{dx}\right\}^{-1}. \tag{2.7}$$

Substituting 2.6 and 2.7 into 2.5 leads:

$$\Phi' E', \boldsymbol{r}' dE' d\Omega = \int_{E'}^{\infty} \frac{q(E_2)\nu(E_2, E')}{dE'/dx}dE_2\frac{\cos\theta' d\Omega' dE'}{4\pi} \tag{2.8}$$

At this stage, Thompson introduced several assumptions:

- $\nu(E_2, E') = \eta E_2/E'$ (η is a constant with the order of unity)
- $dE'/dx \sim E'/D$ (D is the nearest neighbor distance of the bulk atoms)
- $q(E_2)$ is independent of the location (uniform in space).
- Inter atomic potential between the primary ion and the bulk atom is:

$$V(r) = \frac{2E_R}{e}(Z_1 Z_2)^{5/6}(a_0/r)^2, \tag{2.9}$$

  where E_R is the Rydberg energy and a_0 is the Bohr radius. Using this,

$$q(E_2) = \begin{cases} 0 & (E_2 > \Lambda E_1) \\ \frac{\pi^2 a^2 n E_a \Lambda^{1/2}\Phi_1}{8{E_1}^{1/2}{E_2}^{3/2}} & (E_2 < \Lambda E_1) \end{cases} \tag{2.10}$$

E_1	energy of the primary ion
Φ_1	flux of ions crossing unit area normal to their path
n	density of atoms
a	screening radius of interatomic potential ($= a_0/(Z_1 Z_2)^{1/6}$)
Λ	energy transfer coefficient between the ion and the atom ($= 4M_1M_2/(M_1+M_2)^2$)
E_a	the value of E_1 that gives a distance of closest approach of a in a head-on collision ($= 2E_R(Z_1Z_2)^{7/6}(M_1+M_2)/(eM_2)$)

Table 2.1: notations in equation 2.10

(please refer to table 2.1 for notations).

With these assumptions, equation 2.8 becomes:

$$\Phi'(E', \boldsymbol{r}')dE'd\Omega = \frac{\pi^2 a^2 n E_a \Phi_1 \eta D}{16E'^2}\left[1 - \sqrt{\frac{E'}{\Lambda E_1}}\right]\frac{\cos\theta' d\Omega}{4\pi} \tag{2.11}$$

Now we progress into the case where the bulk is cut by the surface, and the potential difference (=binding energy) E_b exists between the particles inside/outside of the bulk. When the inside particle with kinetic energy E', speed v' and angle θ' emits outside of the surface and has E, v and θ there, these quantities should fulfill the following relations because of the preservation of energy, tangential momentum, etc.:

$$v' \sin\theta' = v \sin\theta \tag{2.12}$$

$$\frac{1}{2}M_2 v'^2 \cos^2\theta' = \frac{1}{2}M_2 v^2 \cos^2\theta + E_b \tag{2.13}$$

$$E' = E + E_b. \tag{2.14}$$

The relation between the density function of the flux inside/outside of the bulk is:

$$\Phi'(E', \theta')dE' \sin\theta' d\theta' = \Phi(E, \theta)\sin\theta d\theta, \tag{2.15}$$

that is,

$$\Phi(E, \theta) = \Phi'(E', \theta')\frac{dE'}{dE}\frac{d\theta'}{d\theta}\frac{\sin\theta'}{\sin\theta}. \tag{2.16}$$

Therefore, we can rewrite the equation 2.7 using eqs. 2.12–2.14 and obtain:

$$\Phi(E, \theta) = \frac{\cos\theta}{4\pi(1 + E_b/E)}\int_{E+E_b}^{\infty}\frac{q(E_2)\nu(E_2, E')}{dE'/dx}dE_2. \tag{2.17}$$

Now we can use the same assumption and procedure, which are used to obtain eq. 2.11 from eq. 2.7. The result is:

$$\Phi(E, \theta)dEd\Omega = P\cos\theta\frac{1 - \sqrt{(E_b + E)/\Lambda E_1}}{E^2(1 + E_b/E)^3}dEd\Omega, \tag{2.18}$$

where $P = \pi a^2 n \Lambda E_a \eta D \Phi_1 / 16$.

As shown in eq. 2.18, energy distribution is independent of the ejection angle θ. So on applying this to the MC simulation, we determine the energy independently of the angle. Neglecting the constant term, EDF can be written as:

$$f(E) \propto E \frac{1 - \sqrt{(E_b + E)/\Lambda E_1}}{(E + E_b)^3} \tag{2.19}$$

The region of the energy E is $0 < E < \Lambda E_1 - E_b$. Since ejection event is basically only at once for each particle, it does not effect significantly on the calculational complexity. So we use the acceptance-rejection procedure to determine E from this function in this study.

2.2.3 Angular distribution

In case of collision cascade as described in the preceding subsection, the particle flux ejecting through the unit area of the surface obeys the cosine rule:

$$\Phi(\theta') \propto \cos\theta'. \tag{2.20}$$

Note that it is lead by the assumption that the distribution of particle speed in the collision cascade is independent of the direction. θ is the angle between the direction of the flux and the surface normal, and is in the range $0 \leq \theta < \pi$. We assume that the cosine law is valid throughout this study. Though it should be noted that a few reports have stated the distribution does not agree with the cosine law (as introduced in 1.2.1).

In the simulation of the particle transport process, including ours, you have to determine the 3D vector of the particle direction on the ejection event. Hence, it is more convenient to know the distribution of $\cos\theta$ than that of θ itself. So we try to transform the flux distribution $\Phi(\theta)$ into $f(x)$ with $x \equiv \cos\theta$. Then we can obtain the relation:

$$\begin{aligned} \Phi(\theta)d\theta &= -f(x)\frac{dx}{\sqrt{1-x^2}} \\ 0 \leq \theta \leq \pi &\rightarrow 1 \geq x \geq 0. \end{aligned}$$

If the primitive function $F(x)$ of $f(x)/\sqrt{1-x^2}$ can be obtained analytically, x is yielded from the pseudo-random number w by solving:

$$\omega = \frac{F(x) - F(0)}{F(1) - F(0)}. \tag{2.21}$$

If the inverse function F^{-1} of F is also given, x is obtained by:

$$x = F^{-1}\left((F_1 - F_0)w + F_0\right) \tag{2.22}$$

In the case of cosine distribution, where $f(x)$ is simply x, $F(x)$ becomes $-\sqrt{1-x^2}$. Hence, using eq. 2.22, $\cos\theta$ is obtained from the random number w by:

$$\cos\theta = \sqrt{1-w} \tag{2.23}$$

At the same time, $\sin\theta$ is also given with the same w:

$$\sin\theta = \sqrt{w} \tag{2.24}$$

On ejection, you also need the polar angle ϕ in addition to the θ. In this study, we simply assume that it distributes uniformly between $0 \sim 2\pi$.

2.3 Collision and scattering with gases

In this section, we consider the collision of the sputtered particle with ambient gases. The treatment of the thermal motions of gases is described in detail in section 2.5, while some of the rules in this section are still applicable there.

2.3.1 Mean free path

In this subsection, we treat the "free path" of the sputtered particles. It is the distance in which the particle goes without the collision event. In the current discussion, we assume that the sputtered particle is traveling through the gas environment, in which each gas is stationary. If the collision occurs when the distance between the center of the sputtered particle and that of the gas becomes less than b_{max}, gases can be treated as targets with the cross section of $\sigma = \pi {b_{max}}^2$. In this case, when the sputtered particle goes the distance dx, the collision occurs if the gas is in the volume $\sigma\, dx$. Using the gas density n, the probability of this collision event becomes $n\sigma dx$. As a consequence, the distribution $p(x)$ of the free path x of the sputtered particle obeys the differential equation:

$$\frac{dp}{dx} = -pn\sigma dx \tag{2.25}$$

If we define the quantity λ which has the unit of length as:

$$\lambda \equiv \frac{1}{n\sigma}, \tag{2.26}$$

we can write $p(x)$ in the form of Poisson distribution

$$p(x) = \frac{1}{\lambda}\exp\left(-\frac{x}{\lambda}\right). \tag{2.27}$$

Note that this function is normalized. Also note that the λ is the mean value of x since:

$$\int_0^\infty x\, p(x) dx = \lambda. \tag{2.28}$$

This λ is called "mean free path (MFP)".

2.3.2 Potential scattering problem

We use the potential scattering for the scattering process between the sputtered particle and the gas. First of all, we introduce the mass, position and the velocity of these two particles: m_p, m_g, $\boldsymbol{r}_p$, $\boldsymbol{r}_g$, $\boldsymbol{v}_p$, $\boldsymbol{v}_g$. Subscript $_p$ and $_g$ denote the particle and the gas, respectively. Boldfaces denote the vector quantity. We also introduce the interatomic potential $U(r)$. It is assumed that $U(r)$ is spherically symmetric (*i.e.*, dependent only on the distance r), and that $U(r) \to 0$ when $r \to \infty$.

We define the center-of-mass coordinate $\boldsymbol{r}_G$ and the relative coordinate $\boldsymbol{r}_R$ as:

$$\boldsymbol{r}_G = \frac{m_p \boldsymbol{r}_p + m_g \boldsymbol{r}_g}{m_p + m_g} \tag{2.29}$$

$$\boldsymbol{r}_R = \boldsymbol{r}_p - \boldsymbol{r}_g \tag{2.30}$$

Velocities $\boldsymbol{v}_G$ and $\boldsymbol{v}_R$ are also defined as $\dot{\boldsymbol{r}_G}$ and $\dot{\boldsymbol{r}_R}$, respectively. Then the kinetic equations of $\boldsymbol{r}_G$ and $\boldsymbol{r}_R$ are:

$$(m_p + m_g)\ddot{\boldsymbol{r}_G} \equiv (m_p + m_g)\dot{\boldsymbol{v}_G} = 0 \tag{2.31}$$

$$\mu\ddot{\boldsymbol{r}_R} \equiv \mu\dot{\boldsymbol{v}_R} = \mathrm{grad}U(r_R) \tag{2.32}$$

where we introduce the effective mass $\mu = m_p m_g/(m_p + m_g)$. We can see from eq. 2.31 that $\boldsymbol{v}_G$ does not change throughout the collision process.

Since $U(r)$ is central potential, the $\boldsymbol{r}_R$ is always included in a single plain which also includes the origin $\boldsymbol{r} = 0$. So we assign $\boldsymbol{r}_R$ in this plane with polar coordinate (ρ, χ) as in figure 2.1. The equations of motion (2.32) then become:

$$\mu\left(\ddot{\rho} - \rho\dot{\chi}\right) = \frac{d}{d\rho}U(\rho) \tag{2.33}$$

$$\mu\left(2\dot{\rho}\dot{\chi} + \rho\ddot{\chi}\right) = 0. \tag{2.34}$$

The former gives the conservation of energy:

$$\frac{1}{2}\mu\left(\dot{\rho}^2 + (\rho\dot{\chi})^2\right) + U(\rho) = \text{const.} \tag{2.35}$$

and the latter gives the conservation of angular momentum:

$$\rho^2\dot{\chi} = \text{const.} \tag{2.36}$$

b in figure 2.1 is called "scattering parameter", which is defined by the component of $\boldsymbol{r}_R$ vertical to $\boldsymbol{v}_R$ at infinity. In the MC simulation, the collision event occurs if this is less than b_{max}, which was appeared in 2.3.1. If we define v_0 as the absolute value of $\boldsymbol{v}_R$ at infinity, the RHS constant terms of eqs. 2.35 and 2.36 are determined:

$$\frac{1}{2}\mu\left[\dot{\rho}^2 + (\rho\dot{\chi})^2\right] + U(\rho) = \frac{1}{2}\mu {v_0}^2 \tag{2.37}$$

$$\rho^2\dot{\chi} = v_0 b \tag{2.38}$$

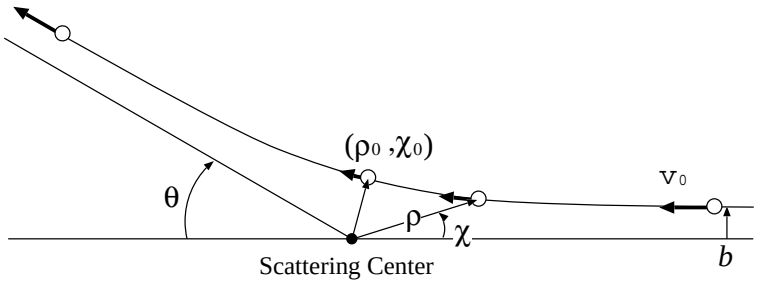

Figure 2.1: Potential scattering in the center-of-mass system.

We can combine eqs. 2.37 and 2.38:

$$\frac{d\chi}{d\rho} = \frac{\dot{\chi}}{\dot{\rho}} = \pm \frac{b/\rho^2}{\sqrt{1-(b/\rho)^2 - 2U(\rho)/\mu {v_0}^2}}. \tag{2.39}$$

Now we introduce the point (ρ_0, χ_0) as shown in fig. 2.1 where $\dot{\rho} = 0$. Then the integration between $\rho_\infty \to \rho_0$ corresponds to $0 \to \chi_0$, so we obtain:

$$\chi_0 = -\int_\infty^{\rho_0} \frac{b/\rho^2}{\sqrt{1-(b/\rho)^2 - 2U(\rho)/\mu {v_0}^2}} d\rho. \tag{2.40}$$

ρ_0 can be given by the relation:

$$1 - \frac{b}{\rho_0}^2 - \frac{2U(\rho_0)}{\mu {v_0}^2} = 0 \tag{2.41}$$

which is obtained by substituting eq. 2.38 and $\dot{\rho} = 0$ into eq. 2.37. It means that the integration of eq. 2.40 has the singularity at ρ_0. However, as described in A.1.1, this singularity can be avoided by the numerical integration using the double exponential type transformation.

Finally, the scattering angle θ is given by:

$$\theta = \pi - 2\chi_0 \tag{2.42}$$

as shown in fig. 2.1.

Remember that the figure 2.1 represents the plane including $\boldsymbol{r}_R$ and the origin (hence the $\boldsymbol{v}_R$ also), and note that the angle of this plane around the direction of initial $\boldsymbol{v}_R$ should be randomly distributed between $0 \sim 2\pi$. Also note that the absolute value of $\boldsymbol{v}_R$ does not change since we are considering the elastic collision only. Therefore, if we take the z axis parallel to the direction of $\boldsymbol{v}_R$ before collision, $\boldsymbol{v}_R$ is:

$$\boldsymbol{v}_R = {}^T(0, 0, v_0),$$

where ^{T} means the transposition of the vector. Then, velocity $\boldsymbol{v}_R{}'$ after the collision becomes:

$$\boldsymbol{v}_R{}' = {}^T(v_0 \sin\theta\cos\phi, v_0 \sin\theta \sin\phi, v_0 \cos\theta)$$

where θ is given from eq. 2.42 and $\phi = 2\pi w$ with the pseudo random number w between $[0, 1)$.

Now we replace $\boldsymbol{r} \to \boldsymbol{v}$ in eqs. 2.29 and 2.30 (which also gives the valid expressions) and solve them. Then we obtain:

$$\boldsymbol{v}_p = \boldsymbol{v}_G + \frac{m_g}{m_p + m_g}\boldsymbol{v}_R. \tag{2.43}$$

Equation 2.43 is also valid after the collision, namely $\boldsymbol{v}_p{}'$ and $\boldsymbol{v}_R{}'$. Remember again that $\boldsymbol{r}_G$ does not change by the collision. If the gas is stationary before the collision (*i.e.*, $\boldsymbol{v}_g = 0$), $\boldsymbol{v}_G$ is:

$$\boldsymbol{v}_G = \frac{m_p}{m_p + m_g}\boldsymbol{v}_p. \tag{2.44}$$

In summary, the velocity $\boldsymbol{v}_p{}'$ of the sputtered particle after the collision is given by:

$$\boldsymbol{v}_p{}' = \frac{m_p\boldsymbol{v}_p + m_g\boldsymbol{v}_R{}'}{m_p + m_g} \tag{2.45}$$

2.3.3 Scattering potential

In the calculation of eq. 2.40 in this study, we use the Born-Mayer type interatomic potential [2]:

$$U(r) = A\exp(-br). \tag{2.46}$$

It has a simple form, and the parameters of many elements have been given by Abrahamson [1]. They are also tabulated in appendix B of this thesis.

Abrahamson has only given the potential parameters between the atoms of same element, but he also showed that the potential between the different elements could be approximated. The potential $U_{a-b}(r)$ between the atoms of element a and b is:

$$U_{ab}(r) = (U_{a-a}U_{b-b})^{1/2} = (A_aA_b)^{1/2}\exp\left(-\frac{b_a + b_b}{2}r\right), \tag{2.47}$$

where A_a and b_a are the parameters between a–a, and A_b and b_b are those for b–b.

For example, we show the potential between Cu and Ar in figure 2.2 (a). Using this potential, the scattering angle θ can be obtained from eq. 2.42, which is shown in figure 2.2 (b). θ is a function of the initial energy $E_0 = (1/2)\mu{v_0}^2$ and the collision parameter b. You can see from the figure that the smaller E_0 gives larger θ at constant b, and requires larger b for constant θ.

2.3.4 Collision parameter

In the simulation, you need to choose the maximum collision parameter b_{max} to calculate the MFP as described in 2.3.1. The collision parameter b for each event in the simulation can be determined such that it distributes uniformly in the area of the target $\sigma = \pi{b_{max}}^2$, *i.e.*:

$$f(b)db \propto bdb. \tag{2.48}$$

[2] It means that we assume all the sputtered particles, as well as gases, are atoms. See section 3.1.2

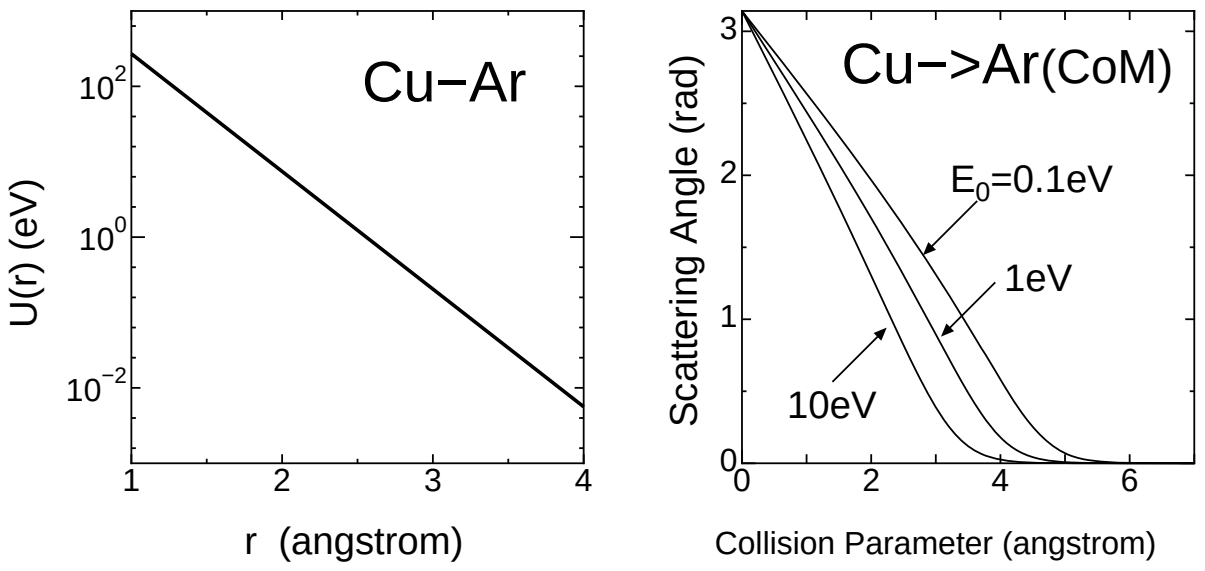

Figure 2.2: (a) Born Mayer potential between Cu and Ar. (b) Dependence of the scattering angle on collision parameter in center of mass system, in case of Cu → Ar collision.

Therefore, using the pseudo-random number w between $[0, 1)$, b is determined by:

$$b = b_{max}\sqrt{\omega}. \tag{2.49}$$

For the potential-scattering case, there is no standard way to determine b_{max}. It depends on the threshold you will give for θ (with some E_0). Larger b_{max} can treat the subtle change in θ, while it causes the shorter MFP, hence the larger computation time.

Nevertheless, the reproducibility of the MC calculation is not affected if b_{max} is large enough. We show it in the following.

We consider two cases, one is $b_{max} = b_1$ and the other is $b_{max} = b_2$ $(b_1 < b_2)$. We assume that b_1 is already large enough, and that collision does not actually occur between $b_1 < b < b_2$ in the latter case.

When $b_{max} = b_1$, mean free path λ_1 is given by eq. 2.26:

$$\lambda_1 = \frac{1}{n\pi {b_1}^2} \tag{2.50}$$

And the probability $p_1(x)dx$ where the collision occurs between x and $x + dx$ is:

$$p_1(x) = \frac{1}{\lambda_1} \exp\left(-\frac{x}{\lambda_1}\right) \tag{2.51}$$

On the other hand, when $b_{max} = b_2$, MFP λ_2 is:

$$\lambda_2 = \frac{1}{n\pi {b_2}^2}. \tag{2.52}$$

Now we consider the probability $p_2(x)dx$, where the collision of $b < b_1$ occurs between x and $x + dx$. It is given by the sum of the probabilities that "collision of $b_1 < b < b_2$ occurs n times" AND "collision of $b < b_1$ occurs between x and $x + dx$", from $n = 1$ to infinity. Hence:

$$\begin{aligned} p_2(x) &= \frac{1}{\lambda_2}\exp\left(-\frac{x}{\lambda_2}\right)\frac{{b_1}^2}{{b_2}^2} + \int_0^x d\xi \frac{1}{{\lambda_2}^2}\exp\left(-\frac{\xi}{\lambda_2}\right)\exp\left(-\frac{x-\xi}{\lambda_2}\right)\left(1-\frac{{b_1}^2}{{b_2}^2}\right)\frac{{b_1}^2}{{b_2}^2} \\ &+ \int_0^x d\xi_1 \int_{\xi_1}^x d\xi_2 \frac{1}{{\lambda_2}^3}\exp\left(-\frac{\xi_1}{\lambda_2}\right)\exp\left(-\frac{\xi_2-\xi_1}{\lambda_2}\right)\exp\left(-\frac{x-\xi_2}{\lambda_2}\right)\left(1-\frac{{b_1}^2}{{b_2}^2}\right)^2\frac{{b_1}^2}{{b_2}^2} \\ &+ \ldots. \end{aligned} \tag{2.53}$$

Note that the terms of exp's in the integral can simply be rewritten as $\exp(-x/\lambda_2)$, so using the relation

$$\frac{{b_1}^2}{{b_2}^2} = \frac{\lambda_2}{\lambda_1}$$

and

$$\int_0^x d\xi_1 \int_{\xi_1}^x d\xi_2 \cdots \int_{\xi_{n-1}}^x d\xi_n = \frac{x^n}{n!},$$

$p_2(x)$ becomes:

$$\begin{aligned} p_2(x) &= \frac{1}{\lambda_2}\exp\left(-\frac{x}{\lambda_2}\right)\left[\frac{\lambda_2}{\lambda_1} + \frac{1}{\lambda_2}\left(1-\frac{\lambda_2}{\lambda_1}\right)\frac{\lambda_2}{\lambda_1}x + \frac{1}{{\lambda_2}^2}\left(1-\frac{\lambda_2}{\lambda_1}\right)^2\frac{\lambda_2}{\lambda_1}\frac{x^2}{2!} + \ldots..\right] \\ &= \frac{1}{\lambda_2}\exp\left(-\frac{x}{\lambda_2}\right)\exp\left[\left(\frac{1}{\lambda_2}-\frac{1}{\lambda_1}\right)x\right]\frac{\lambda_1}{\lambda_2} = \frac{1}{\lambda_1}\exp\left(-\frac{x}{\lambda_1}\right), \end{aligned} \tag{2.54}$$

and is proved to be identical with $p_1(x)$.

2.4 Trapping on the chamber boundary

In this study, we simply assume that the particle reached at the chamber boundary deposits there with the probability of unity. The estimation whether the particle path crosses the boundary is rather complicated in the axisymmetric coordinate, hence we summarize the procedure here.

We use the index p for the position of the particle, and b for the boundary. The components of the 3D Cartesian coordinate is expressed by x, y and z, and its projection to the axisymmetric coordinate by r and z. With these, the following relation comprises:

$$r^2 = x^2 + y^2 \tag{2.55}$$

After a collision event, the direction and the free path of the particle is determined. The start and the end of this path are defined as (x_{p1}, y_{p1}, z_{p1}) and (x_{p2}, y_{p2}, z_{p2}). In the following, we consider the method to determine whether this path crosses with any of the (linear) boundary element from (r_{b1}, z_{b1}) to (r_{b2}, z_{b2}).

At first, we consider necessary conditions of the trap event. The path of the particle is:

$$\begin{aligned} x &= (1-t)x_{p1} + tx_{p2} \\ y &= (1-t)y_{p1} + ty_{p2} \\ z &= (1-t)z_{p1} + tz_{p2} \end{aligned}$$

where $(0 \leq t \leq 1)$. By projecting these to the axisymmetric coordinate, we obtain:

$$r^2 = (1-t)^2 r_{p1}^2 + t^2 r_{p2}^2 + 2t(1-t)(r_{p1} \cdot r_{p2}) \tag{2.56}$$

$$z = (1-t)z_{p1} + z_{p2}, \tag{2.57}$$

where $(r_{p1} \cdot r_{p2})$ is defined by:

$$(r_{p1} \cdot r_{p2}) = x_{p1}x_{p2} + y_{p1}y_{p2}. \tag{2.58}$$

Hence the path of the particle becomes hyperbola in (r, z) plane.

Substituting eq. 2.57 into eq. 2.56 and eliminating t, we obtain:

$$\begin{aligned} r^2 &= \left\{r_{p1}^2 + r_{p2}^2 - 2(r_{p1} \cdot r_{p2})\right\} \left\{ t - \frac{r_{p1}^2 - (r_{p1} \cdot r_{p2})}{r_{p1}^2 + r_{p2}^2 - 2(r_{p1} \cdot r_{p2})} \right\}^2 \\ &+ \frac{r_{p1}^2 r_{p2}^2 - (r_{p1} \cdot r_{p2})^2}{r_{p1}^2 + r_{p2}^2 - 2(r_{p1} \cdot r_{p2})}. \end{aligned} \tag{2.59}$$

Hence, if

$$0 \leq \frac{r_{p1}^2 - (r_{p1} \cdot r_{p2})}{r_{p1}^2 + r_{p2}^2 - 2(r_{p1} \cdot r_{p2})} \leq 1 \tag{2.60}$$

is true, the minimum r_{pmin} of r component through the path is given by:

$$r_{pmin}^2 = \frac{r_{p1}^2 r_{p2}^2 - (r_{p1} \cdot r_{p2})^2}{r_{p1}^2 + r_{p2}^2 - 2(r_{p1} \cdot r_{p2})}. \tag{2.61}$$

Otherwise, r_{pmin} is the smaller one of r_{p1} or r_{p2}. As well, r_{pmax}, z_{pmin} and z_{pmax} are:

$$\begin{aligned} r_{pmax} &= \max(r_{p1}, r_{p2}) \\ z_{pmin} &= \min(z_{p1}, z_{p2}) \\ z_{pmax} &= \max(z_{p1}, z_{p2}) \end{aligned}$$

respectively. We also prepare the definitions of r_{bmin}, etc. for the boundary node (r_{b1}, z_{b1})-(r_{b2}, z_{b2}).

Using these parameters, the necessary condition that the the particle path crosses the boundary is the AND's of:

$$\begin{aligned} r_{pmax} &\geq r_{bmin} \\ r_{pmin} &\leq r_{bmax} \\ z_{pmax} &\geq z_{bmin} \\ z_{pmin} &\leq z_{bmax} \end{aligned} \tag{2.62}$$

Next, we consider sufficient conditions when eqs. 2.62 are true. For this, all of:

$$r^2 = (1-t)^2 r_{p1}^2 + t^2 r_{p2}^2 + 2t(1-t)(r_{p1} \cdot r_{p2}) \quad (2.63)$$
$$z = (1-t)z_{p1} + t z_{p2} \quad (2.64)$$
$$r = (1-s)r_{b1} + s r_{b2} \quad (2.65)$$
$$z = (1-s)z_{b1} + s z_{b2} \quad (2.66)$$

must be satisfied. Moreover, $(0 \leq t \leq 1)$ and $(0 \leq s \leq 1)$ are required. When such t's are given from several nodes, the node which gives the smallest t is the one where the particle is trapped actually. We will discuss how to obtain such t's for several cases where the ends of the node have different conditions.

CASE1: $r_{b1} = r_{b2}$

From equation 2.63, we obtain:

$$(r_{p1}^2 + r_{p2}^2 - 2(r_{p1} \cdot r_{p2}))t^2 - 2\left\{r_{p1}^2 - (r_{p1} \cdot r_{p2})\right\} + (r_{p1}^2 - r_{b1}^2) = 0. \quad (2.67)$$

If the discriminant D of this quadratic satisfies the condition $D \geq 0$, then check:

- Solution t satisfies $0 \leq t \leq 1$.
- Substituting the t into eq. 2.64, and the resultant z satisfies $z_{bmin} \leq z \leq z_{bmax}$.

If both of these conditions are satisfied, the particle is trapped there. When both solutions of the quadratic satisfies these, the smaller one is adopted.

CASE2: $z_{b1} = z_{b2}$

If $z_{p1} = z_{p2}$ is also satisfied, the path of the particle becomes the line parallel to the r axis, and the trapping point r is:

- $r = r_{bmin}$ if $r_{pmin} \leq r_{bmax}$.
- $r = r_{bmax}$ if $r_{pmax} \geq r_{bmin}$.

If $z_{p1} \neq z_{p2}$, t becomes:

$$t = \frac{z_{b1} - z_{p1}}{z_{p2} - z_{p1}} \quad (2.68)$$

from eq. 2.64. This t automatically satisfies $0 \leq t \leq 1$ from eq. 2.62. So if r, obtained by the t and eq. 2.63, satisfies $r_{pmin} \leq r \leq r_{pmax}$, the particle is trapped.

CASE3: the other

Eliminating r, z and s from eq. 2.63 gives:

$$\begin{aligned} 0 &= \left[\left(\frac{r_{b2}-r_{b1}}{z_{b2}-z_{b1}}\right)^2 (z_{p2}-z_{p1})^2 - r_{p1}^2 - r_{p2}^2 + 2(r_{p1}\cdot r_{p2})\right] t^2 \\ &+ \left[\left(\frac{r_{b2}-r_{b1}}{z_{b2}-z_{b1}}\right)^2 (z_{p2}-z_{p1})\left(z_{p1}-z_{b1}+\frac{z_{b2}-z_{b1}}{r_{b2}-r_{b1}}r_{b1}\right) + r_{p1}^2 - (r_{p1}\cdot r_{p2})\right] 2t \\ &+ \left[\left(\frac{r_{b2}-r_{b1}}{z_{b2}-z_{b1}}\right)^2 \left(z_{p1}-z_{b1}+\frac{z_{b2}-z_{b1}}{r_{b2}-r_{b1}}r_{b1}\right)^2 - r_{p1}^2\right]. \end{aligned} \tag{2.69}$$

If the discriminant D of this quadratic satisfies $D \geq 0$, then solve the equation and determine t. And then check:

- Solution t satisfies $0 \leq t \leq 1$.
- s deduced from eqs. 2.64 and 2.66 satisfies $0 \leq s \leq 1$.

If both of these are satisfied, the particle is trapped there. If both of the solution of the quadratic satisfies these, the smaller one is adopted.

2.5 MC calculation with the thermal motion of gases

In this section, we consider the particle p traveling in the gas atmosphere with the speed v_p, and discuss its interaction (*i.e.*, collision and scattering) with environmental gas particles. We propose the method to simulate this process, which can be applied to the Monte Carlo simulation.

2.5.1 Collision frequency and mean free path

We consider the particle p traveling in the gas atmosphere, and show how the gases collide to the particle. The discussion in this section is partly based on the chapter X of the reference [56] by Jeans.

We assume that the distribution of the gas speed is the Maxwellian:

$$f(v_g) = \frac{4}{\sqrt{\pi}}\alpha^{\frac{3}{2}} {v_g}^2 \exp\left(-\alpha {v_g}^2\right) \tag{2.70}$$

where v_g is the speed of the gas and $\alpha = m_g/2kT_g$. k is the Boltzmann's constant, m_g is mass of the gas particle, and T_g is gas temperature. We also assume that the distribution is only dependent on the speed, and not on the direction.

Now we consider the contribution of gases from $[v_g \sim v_g + dv_g]$, $[\theta \sim \theta + d\theta]$, $[\phi \sim \phi + d\phi]$ to the collision. θ and ϕ are the azimuthal and the polar angles of the velocity of g corresponding to the direction of p, respectively. Then the contribution $d\nu$ from this part of the velocity-space to the total collision frequency ν is given by:

$$d\nu = \pi {b_{pg}}^2 v_R n_g f(v_g) dv_g \frac{\sin\theta d\theta d\phi}{4\pi} \tag{2.71}$$

where b_{pg} is a maximum collision parameter, n_g is gas density. v_R is the relative speed between the particle p and colliding gas g, which is defined by (see figure 2.3):

$$v_R^2 = v_p^2 + {v_g}^2 - 2v_p v_g \cos\theta. \tag{2.72}$$

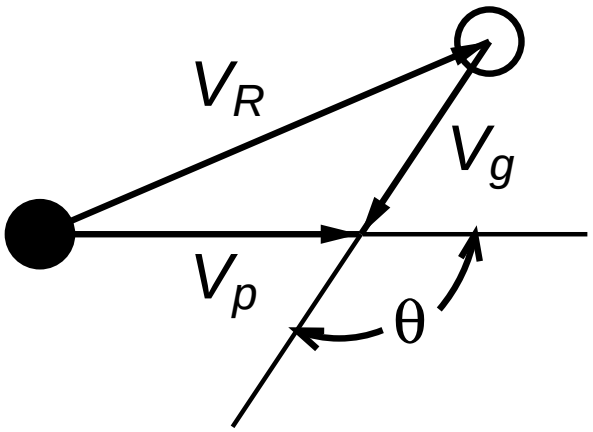

Figure 2.3: v_p, v_g, v_R and θ.

ν is obtained by integrating 2.71 within whole velocity space.

$$\nu = \int_{v_g=0}^{\infty}\int_{\theta=0}^{\pi}\int_{\phi=0}^{2\pi} d\nu \tag{2.73}$$

Assuming that the density and the temperature of the gas are uniform, integration with ϕ simply becomes 2π:

$$\nu = 2\pi^{\frac{1}{2}} {b_{pg}}^2 n_g \alpha^{3/2} \int_0^{\infty} dv_g \int_0^{\pi} \sin\theta d\theta v_R {v_g}^2 \exp\left(-\alpha {v_g}^2\right). \tag{2.74}$$

We now transform the integration variable from (v_g, θ) to (v_g, v_R). Range of the v_R then becomes from $|v_p - v_g|$ to $v_p + v_g$, while the Jacobian is:

$$\frac{\partial(v_g,\theta)}{\partial(v_g,v_R)} = \begin{vmatrix} \frac{\partial v_g}{\partial v_g} & \frac{\partial v_g}{\partial v_R} \\ \frac{\partial \theta}{\partial v_g} & \frac{\partial \theta}{\partial v_R} \end{vmatrix} = \frac{\partial\theta}{\partial v_R} = \frac{v_R}{v_p v_g \sin\theta}. \tag{2.75}$$

Using these, equation 2.74 can be rewritten as:

$$\nu = A\int_0^{\infty} dv_g \frac{v_g}{v_p} \exp\left(-\alpha {v_g}^2\right) \int_{|v_p - v_g|}^{v_p+v_g} {v_R}^2 dv_R \tag{2.76}$$

where $A = 2\pi^{\frac{1}{2}} {b_{pg}}^2 \alpha^{3/2}$.

Integration with v_R is given as follows:

$$\int_{|v_p-v_g|}^{v_p+v_g} {v_R}^2 dv_R = \begin{cases} \frac{2}{3}(v_p^3 + 3v_p {v_g}^2) & (v_g > v_p) \\ \frac{2}{3}({v_g}^3 + 3v_g {v_p}^2) & (v_g < v_p). \end{cases} \tag{2.77}$$

By substituting eq. 2.77 into eq. 2.76, we obtain:

$$\nu = A' \left\{ \int_{v_p}^{\infty} (v_p^2 v_g + 3{v_g}^3) \exp(-\alpha {v_g}^2) dv_g + \frac{1}{v_p} \int_0^{v_p} ({v_g}^4 + 3v_p^2 {v_g}^2) \exp(-\alpha {v_g}^2) dv_g \right\}, \quad (2.78)$$

where $A' = \frac{2}{3}A$.

The first term of equation 2.78 is:

$$\begin{aligned} & v_p^2 \int_{v_p}^{\infty} v_g \exp(-\alpha {v_g}^2) dv_g + 3 \int_{v_p}^{\infty} {v_g}^3 \exp(-\alpha {v_g}^2) dv_g \\ = & \left(v_p^2 + \frac{3}{\alpha} \right) \int_{v_p}^{\infty} v_g \exp(-\alpha {v_g}^2) dv_g - 3 \left[\frac{{v_g}^2 \exp(-\alpha {v_g}^2)}{2\alpha} \right]_{v_p}^{\infty} \\ = & \left(v_p^2 + \frac{3}{\alpha} \right) \left[-\frac{1}{2} \frac{\exp(-\alpha {v_g}^2)}{\alpha} \right]_{v_p}^{\infty} - 3 \left[\frac{{v_g}^2 \exp(-\alpha {v_g}^2)}{2\alpha} \right]_{v_p}^{\infty} \\ = & \frac{\exp(-\alpha {v_p}^2)}{\alpha} \left\{ 2{v_p}^2 + \frac{3}{2\alpha} \right\}. \end{aligned} \quad (2.79)$$

Likewise, the second term is:

$$\begin{aligned} & \frac{1}{v_p} \int_0^{v_p} {v_g}^4 \exp(-\alpha {v_g}^2) dv_g + 3v_p \int_0^{v_p} {v_g}^2 \exp(-\alpha {v_g}^2) dv_g \\ = & \frac{1}{v_p} \left[-\frac{{v_g}^3 \exp(-\alpha {v_g}^2)}{2\alpha} \right]_0^{v_p} + \left(\frac{3}{2\alpha v_p} + 3v_p \right) \int_0^{v_p} {v_g}^2 \exp(-\alpha {v_g}^2) dv_g \\ = & -\frac{{v_p}^2 \exp(-\alpha {v_p}^2)}{2\alpha} + \left(\frac{3}{2\alpha v_p} + 3v_p \right) \left\{ \left[-\frac{v_g \exp(-\alpha {v_g}^2)}{2\alpha} \right]_0^{v_p} + \frac{1}{2\alpha} \int_0^{v_p} \exp(-\alpha {v_g}^2) dv_g \right\} \\ = & -2\frac{{v_p}^2 \exp(-\alpha {v_p}^2)}{\alpha} - \frac{3\exp(-\alpha {v_p}^2)}{4\alpha^2} + \left(\frac{3}{2\alpha v_p} + 3v_p \right) \frac{1}{2\alpha^{3/2}} \int_0^{\sqrt{\alpha} v_p} \exp(-y^2) dy, \end{aligned} \quad (2.80)$$

where y is defined by $y = \sqrt{\alpha}\, v_g$. Combining 2.79 and 2.80 gives:

$$\frac{3\exp(-\alpha {v_p}^2)}{4\alpha^2} + \left(\frac{3}{2\alpha v_p} + 3v_p \right) \frac{1}{2\alpha^{3/2}} \int_0^{\sqrt{\alpha} v_p} \exp(-y^2) dy. \quad (2.81)$$

Now we define the function Ψ:

$$\begin{aligned} \Psi(x) &= x \exp(-x^2) + (2x^2 + 1) \int_0^x \exp(-y^2) dy \\ &= x \exp(-x^2) + (2x^2 + 1) \frac{\sqrt{\pi}}{2} \operatorname{Erf}(x). \end{aligned} \quad (2.82)$$

$\operatorname{Erf}(x)$ is the Gaussian Error function which is defined by:

$$\operatorname{Erf}(x) = \frac{2}{\sqrt{\pi}} \int_0^x \exp(-y^2) dy. \quad (2.83)$$

The value of this function is in between zero to unity.

By using 2.82, equation 2.81 becomes:

$$\frac{3}{4v_p\alpha^{5/2}}\Psi(v_p\sqrt{\alpha}). \tag{2.84}$$

Finally, the collision frequency ν and the mean free path λ are obtained as follows.

$$\begin{aligned}\nu &= A'\frac{3}{4v_p\alpha^{5/2}}\Psi(v_p\sqrt{\alpha}) \\ &= \frac{2\sqrt{\pi}{b_{pg}}^2 n_g kT_g}{m_g v_p}\Psi\left(v_p\sqrt{\frac{m_g}{2kT_g}}\right)\end{aligned} \tag{2.85}$$

$$\begin{aligned}\lambda \equiv \frac{v_p}{\nu} &= \frac{m_g {v_p}^2}{2\sqrt{\pi}{b_{pg}}^2 n_g kT_g}\frac{1}{\Psi\left(v_p\sqrt{\frac{m_g}{2kT_g}}\right)} \\ &= \frac{m_g {v_p}^2}{2\sqrt{\pi}{b_{pg}}^2 P_g}\frac{1}{\Psi\left(v_p\sqrt{\frac{m_g}{2kT_g}}\right)}\end{aligned} \tag{2.86}$$

$P_g = n_g kT_g$ is the gas pressure.

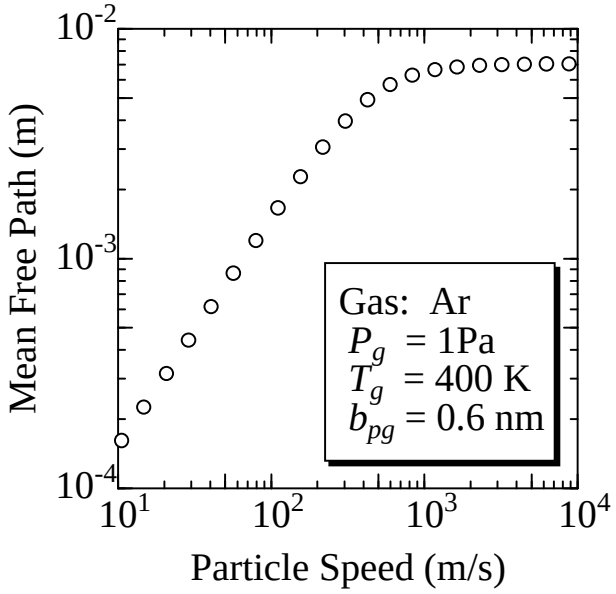

Figure 2.4: Dependence of the particle mean free path on its speed.

Figure 2.4 shows the dependence of the particle MFP on its speed, calculated by eq. 2.86. It is the case for an Ar gas of 1 Pa and 400 K. The latter condition leads the mean speed of Ar atoms about 460 m/s. The maximum collision parameter is set to 0.6 nm. It is rather larger

than the one used in the hard-sphere model, since we use the potential scattering so that even the large collision parameter may cause the deflection of the particle which cannot be neglected at lower energies (see figure 2.2). The value of 0.6 nm is chosen in this study so that the cosine of the scattering angle θ_s in equation 2.42 is less than 10^{-5} when the relative kinetic energy $\mu v_R^2/2$ is 10^{-3} eV.

The MFP dependence on the particle speed v_p can be separated into two regions by the relation between v_p and the thermal speed of gases. When v_p is much faster, gas particles can be regarded as stationary targets. In this case, the MFP becomes the constant value which has been used in the MC simulation ignoring gas motion. On the other hand, when v_p is much slower, *the particle* can be taken as immobile. In this region, the collision frequency approaches to constant, hence the MFP becomes proportional to v_p. From figure 2.4, it is clearly understood that ignoring the gas motion leads to the overestimation of MFP in lower energy region.

2.5.2 Determination of the velocity of colliding gas

In this subsection, we describe how to determine the colliding gas speed v_g and the relative speed v_R from the pseudo-random number w, based on the discussion in the previous subsection. Once v_g and v_R are given, collision angle θ (see fig. 2.3) can easily be deduced.

We assume that the particle p has the speed v_p just after some collision (or the ejection from the target). Firstly, we calculate the mean free path λ with eq. 2.86, and then the free path of p using the method described in 2.3.1.

Now we define the function ν' of the variable v_g by (see equation 2.76):

$$\nu'(v_g) = A \int_0^{v_g} dv_g' \frac{v_g'}{v_p} \exp\left(-\alpha {v_g'}^2\right) \int_{|v_p - v_g|}^{v_p + v_g} v_R^2 dv_R. \tag{2.87}$$

With this, speed of the colliding gas v_g can be determined by the condition:

$$w = \nu'(v_g)/\nu \tag{2.88}$$

where w is a pseudo random number in $(0, 1]$.

Once v_p and v_g are given, another w is generated and used to determine v_R, from the following relation:

$$\begin{aligned} w &= \frac{\int_{|v_p - v_g|}^{v_R} v^2 dv}{\int_{|v_p - v_g|}^{v_p + v_g} v^2 dv} \\ &= \frac{v_R^3 - |v_p - v_g|^3}{(v_p + v_g)^3 - |v_p - v_g|^3} \end{aligned} \tag{2.89}$$

In the simulation program, distribution function of v_g, which depends on v_p and random number w, is approximated by two dimensional spline function so that the calculational complexity is reduced. The detail of the program used in this study will be described in appendix A.

The examples of the $\boldsymbol{v_R}$ distribution are shown in figure 2.5. In these, environmental gas is assumed to be an argon with the temperature of 400 K. Each subfigure represents the cases of $v_p = 300$ m/s, 1000 m/s and 3000 m/s, respectively. Z-axis of these figures are taken to be the

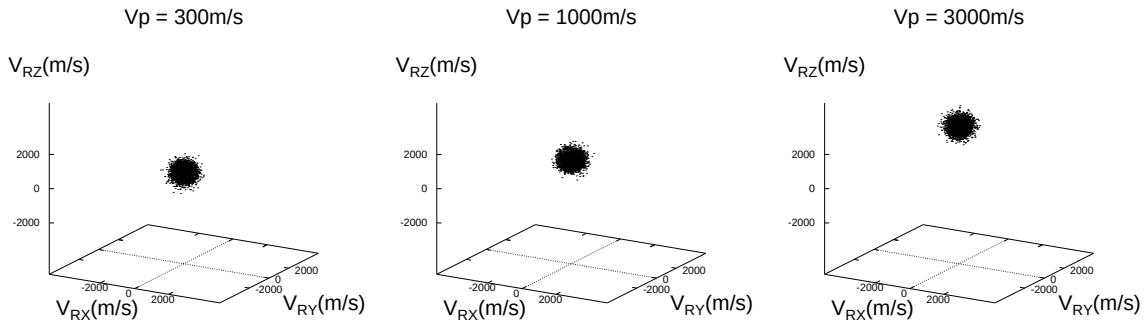

Figure 2.5: Dependence of v_R distribution on v_p.

direction of the particle p. v_R is randomly determined 5000 times using the eqs. 2.87, 2.88 and 2.89, and plotted.

Centers of distribution seem to be at about $(0, 0, v_p)$, but they are not actually. As can be seen in eq. 2.71, the distribution of v_R is given by the multiplication of the Maxwellian and the relative speed v_R. Hence, if v_g is equal, the probability of the collision becomes higher where v_R is large. In other words, the particle p tends to be collided more by the gases whose velocity is opposed to it. Also note that the colliding gas velocity cannot be determined simply by the Maxwellian, which was the method used in the report of Turner *et al.* in [153].

2.5.3 Particle velocity after the scattering

Since our treatment includes the motion of gas particles, the determination of the particle velocity after the scattering is slightly complicated. Since we prepare this subsection to discuss it.

First of all, the following two definitions are introduced.

1. The velocity vector of the sputtered particle p before the collision has the form:

$$\boldsymbol{v_p} = v_p \left(\sin\theta_p \cos\phi_p, \sin\theta_p \sin\phi_p, \cos\theta_p\right) \tag{2.90}$$

   in the laboratory system. v_p is an absolute value of the speed. θ_p and ϕ_p are the azimuthal/polar angle of vector $\boldsymbol{v_p}$ in the polar coordinate.

2. Three dimensional rotational transforms $\mathrm{R_Y}(\theta)$ and $\mathrm{R_Z}(\phi)$ are defined as follows:

$$\mathrm{R_Y}(\theta) = \begin{pmatrix} \cos\theta & 0 & \sin\theta \\ 0 & 1 & 0 \\ -\sin\theta & 0 & \cos\theta \end{pmatrix} \tag{2.91}$$

$$\mathrm{R_Z}(\phi) = \begin{pmatrix} \cos\phi & -\sin\phi & 0 \\ \sin\phi & \cos\phi & 0 \\ 0 & 0 & 1 \end{pmatrix}. \tag{2.92}$$

$\mathrm{R_Y}(\theta)$ denotes the clockwise rotation around $(0,1,0)$ direction by θ, and $\mathrm{R_X}(\phi)$ does around $(0,0,1)$ by ϕ.

Using these, following relation can be deduced:

$$\mathrm{R_Y}(-\theta_p)\mathrm{R_Z}(-\phi_p)^{\mathrm{T}}\boldsymbol{v_p} = (0,0,v_p) \tag{2.93}$$

where ^{T} means the transposition of the vector.

Now we consider the following coordinates:

I The laboratory system.

II The coordinate whose z axis is parallel to the velocity of the particle p.

II' The coordinate that includes the gas velocity vector within its xz plane, in addition to the condition of II.

III The coordinate whose z axis is parallel to the relative velocity vector between p and g, and the velocity vectors of both p and g are included in the xz plane.

In the following, we will obtain conversion rules between these coordinates. We use the format $\boldsymbol{v}^I$ to denote the Cartesian representation of the vector in the coordinate I, and likewise for II, II' and III. We also define the operator $\mathrm{T_{I\to II}}$, etc., which transform these vector representations:

$$\boldsymbol{v}^{(\mathrm{II})} = \mathrm{T_{I\to II}}\boldsymbol{v}^{(\mathrm{I})} \tag{2.94}$$

Remember that the velocity of the particle p in coordinate I is given by 2.90. As apparently from equation 2.93, one of the operations which makes this vector parallel to the z axis is given by:

$$\mathrm{T_{I\to II}} = \mathrm{R_Y}(-\theta_p)\mathrm{R_Z}(-\phi_p). \tag{2.95}$$

Hence the reverse operation is:

$$\mathrm{T_{II\to I}} = \mathrm{R_Z}(\phi_p)\mathrm{R_Y}(\theta_p). \tag{2.96}$$

In the coordinate II, the colliding gas speed v_g and the relative speed v_R can be determined using the method described in 2.5.2. Now we introduce the velocity vectors $\boldsymbol{v_p}$ and $\boldsymbol{v_g}$ for particles p and g, respectively, and $\boldsymbol{v_R}$ for the relative velocity between them. If we express these vectors in II, we obtain:

$$\boldsymbol{v_p}^{(\mathrm{II})} = v_p(0,0,1) \tag{2.97}$$

$$\boldsymbol{v_g}^{(\mathrm{II})} = v_g(\sin\theta_g\cos\phi_g, \sin\theta_g\sin\phi_g, \cos\theta_g) \tag{2.98}$$

$$\boldsymbol{v_R}^{(\mathrm{II})} = v_R(\sin\theta_R\cos\phi_R, \sin\theta_R\sin\phi_R, \cos\theta_R) \tag{2.99}$$

θ_g and θ_R are given so as to fulfill the following three conditions simultaneously:

$$\cos\theta_g = \frac{{v_p}^2 + {v_g}^2 - {v_R}^2}{2v_pv_g} \tag{2.100}$$

$$\cos\theta_R = \frac{{v_p}^2 + {v_R}^2 - {v_g}^2}{2v_pv_R} \tag{2.101}$$

$$v_g\sin\theta_g = -v_R\sin\theta_R \tag{2.102}$$

ϕ_g and ϕ_R are the identical value, which is obtained by the random number uniformly distributing within $0 \sim 2\pi$.

Using θ_R and ϕ_R, we can define the $\mathrm{T}_{\mathrm{II}\to\mathrm{II}'}$, $\mathrm{T}_{\mathrm{II}'\to\mathrm{III}}$ and their inverses.

$$\mathrm{T}_{\mathrm{II}\to\mathrm{II}'} = \mathrm{R}_{\mathrm{Z}}(-\phi_R) \tag{2.103}$$
$$\mathrm{T}_{\mathrm{II}'\to\mathrm{II}} = \mathrm{R}_{\mathrm{Z}}(\phi_R) \tag{2.104}$$
$$\mathrm{T}_{\mathrm{II}'\to\mathrm{III}} = \mathrm{R}_{\mathrm{Y}}(-\theta_R) \tag{2.105}$$
$$\mathrm{T}_{\mathrm{III}\to\mathrm{II}'} = \mathrm{R}_{\mathrm{Y}}(\theta_R) \tag{2.106}$$

Note that the components of $\boldsymbol{v_p}$, $\boldsymbol{v_g}$ and $\boldsymbol{v_R}$ in coordinate II' are:

$$\boldsymbol{v}_p{}^{(\mathrm{II}')} = v_p(0,0,1) \tag{2.107}$$
$$\boldsymbol{v}_g{}^{(\mathrm{II}')} = v_g(\sin\theta_g, 0, \cos\theta_g) \tag{2.108}$$
$$\boldsymbol{v}_R{}^{(\mathrm{II}')} = v_R(\sin\theta_R, 0, \cos\theta_R) \tag{2.109}$$

and that of $\boldsymbol{v_R}$ in III is:

$$\boldsymbol{v}_R{}^{(\mathrm{III})} = v_R(0,0,1). \tag{2.110}$$

In this coordinate III, we can obtain the relative velocity vector $\boldsymbol{v_R}'$ after the potential scattering (We use ´ for the values after the scattering) by using the method described in 2.3.2. Once $\boldsymbol{v_R}'$ is yielded, we simply trace back the conversions.

Summarizing, the velocity vector $\boldsymbol{v_p}'$ of the particle p after the collision is, in the laboratory system, determined by solving:

$$\boldsymbol{v}_p'{}^{(\mathrm{I})} = \mathrm{T}_{\mathrm{II}\to\mathrm{I}}\boldsymbol{v_p}'{}^{(\mathrm{II})} \tag{2.111}$$
$$\boldsymbol{v}_p'{}^{(\mathrm{II})} = \mathrm{T}_{\mathrm{II}'\to\mathrm{II}}\boldsymbol{v}_p'{}^{(\mathrm{II}')} \tag{2.112}$$
$$\boldsymbol{v}_p'{}^{(\mathrm{II}')} = \boldsymbol{v}_G{}^{(\mathrm{II}')} + \frac{m_g}{m_p+m_g}\boldsymbol{v}_R'{}^{(\mathrm{II}')} \tag{2.113}$$
$$\boldsymbol{v}_R'{}^{(\mathrm{II}')} = \mathrm{T}_{\mathrm{III}\to\mathrm{II}'}\boldsymbol{v}_R'{}^{(\mathrm{III})} \tag{2.114}$$

where $\boldsymbol{v_G}^{(\mathrm{II}')}$ is given using θ_g appeared in equation 2.100:

$$\boldsymbol{v_G}^{(\mathrm{II}')} = \left(\frac{m_g v_g \sin\theta_g}{m_p+m_g}, 0, \frac{m_p v_p + m_g v_g \cos\theta_g}{m_p+m_g}\right) \tag{2.115}$$

2.6 Particle transport after the thermalization

Until the previous section, we have discussed the Monte Carlo simulation of the particle transport. As pressure increases, however, computational complexity of the MC calculation becomes very large. For example, under the condition of 10 Pa and 300 K, if you set the maximum collision parameter to be 7 Å, mean free path λ (ignoring the gas motion) becomes 2.69×10^{-4} m, which is much smaller than the size of the ordinary vacuum chamber.

After sputtered particles lose their initial energy and are thermalized [3], their motion can be described by the 3-dimensional random walk. In this stage, the number of collisions before the dispersion of its position spreads x is approximately $(x/\lambda)^2$. Hence, the calculation amount of the MC simulation increases proportional to the square of the pressure.

The random walk type transport can be described with the diffusion equation, if the mean free path is much smaller than the chamber size. On applying it to the sputter deposition problem, we have to consider only the steady state (time-independent) condition, where the diffusion coefficient is not necessary as discussed later. In this section, we discuss the description of the diffusion process of the sputtered particles using Poisson equation, based on the idea reported by Petrov *et al.* [109].

2.6.1 Diffusion equation

The diffusion equation of particles in time-dependent form is:

$$\frac{\partial \eta(\boldsymbol{x}, t)}{\partial t} = D\Delta\eta(\vec{x}, t) + \rho(\boldsymbol{x}, t), \tag{2.116}$$

where η is spatial density of particles, D is the diffusion coefficient, and ρ is a distribution function of particle sources. In the current problem, ρ can be regarded as the thermalization points of the sputtered particles where they start the diffusive transport. Since $\partial n/\partial t = 0$ in the steady state, equation 2.116 becomes the Poisson's equation.

If we assume that the sticking coefficient of the particle at the chamber boundary is unity, the flux from outside of the boundary is always zero regardless of the value of particle density η near the wall. Hence, we can use the boundary condition for ordinary chamber boundary:

$$\eta = 0. \tag{2.117}$$

The value to be calculated is the particle flux F onto the boundary:

$$F = D\mathrm{grad}\,\eta \cdot \boldsymbol{n}, \tag{2.118}$$

where $\boldsymbol{n}$ is the normal vector of the boundary surface. Since we have the partial differential equation of second order with Dirichlet boundary condition, F at each boundary can be determined by solving the equation.

2.6.2 Relationship with MC simulation

In this subsection, we consider the case where we trace N_{MC} particles with MC simulation. By this MC simulation, we see the life of particles; the ejection from the target, the collision and scattering with the gas atoms, etc. The particles may be reached at the chamber boundary before they thermalized in the chamber. For these particles, we obtain the arrival number of them on each chamber boundary segments, as well as their angular/energy distributions. With the MC calculation, we also obtain the distribution of the thermalized positions of the particles, as described above. We used it as the source term of the Poisson's equation.

[3] see 1.3.1 for the definition of "thermalization"

Now we consider the time T_{MC} corresponding to the trial of N_{MC} particles in actual deposition experiment. If we express the thermalized position of the particle i by $\boldsymbol{x_i^{Th}}$, the source term ρ in the Poisson's equation can be written as:

$$\rho(\boldsymbol{x}) = \frac{1}{T_{MC}} \sum_{\text{Thermalized}} \delta^3(\boldsymbol{x_i^{Th}} - \boldsymbol{x}) \tag{2.119}$$

And the diffusion equation in steady state becomes:

$$D\Delta\eta + \frac{1}{T_{MC}} \sum_{\text{Thermalized}} \delta^3(\boldsymbol{x_i^{Th}} - \boldsymbol{x}) = 0 \tag{2.120}$$

We must treat two kinds of particles in a same time scale: the first includes the particles which reached the chamber wall during the Monte Carlo step (*i.e.*, before the thermalization), and the second includes the particles arrived at the wall via diffusive treatment. Now let us consider the node S_j of the chamber boundary. The number of particles of the first kind, which reach at this boundary during the time T_{MC}, can be obtained directly from the MC calculation. We write it as N_j^{En}. On the other hand, the number of diffusive particles reached at S_j during T_{MC} is:

$$N_j^{Th} = T_{MC} S_j F = T_{MC} S_j D \text{grad}\, \eta \cdot \boldsymbol{n}. \tag{2.121}$$

If we define θ as:

$$\theta \equiv T_{MC} D\eta, \tag{2.122}$$

eq. 2.120 becomes

$$\Delta\theta + \sum_{\text{Thermalized}} \delta^3(\boldsymbol{x_i^{Th}} - \boldsymbol{x}) = 0, \tag{2.123}$$

and eq. 2.121 becomes:

$$N_j^{Th} = S_j \text{grad}\theta \cdot \boldsymbol{n}, \tag{2.124}$$

which gives the number of particles N_j^{Th} deposited at the node j after the thermalization.

In above, we described that the boundary condition of the chamber wall is Dirichlet type; $\eta = 0$. However, it causes a problem if we apply this condition to the erosion track of the target. As discussed in 2.2.1, the particle deposited on the erosion track must immediately be ejected again to reproduce the depth profile of the erosion track, which would be obtained by the experiment.

In this study, we use the Neumann condition ($\nabla\eta = 0$) at the boundary nodes representing the erosion track. Ideally, we should record the re-deposition profile of the diffusive particles, feedback it to the MC calculation, and iterate this procedure until the erosion profile converges. This strategy, however, will make the calculation procedure too complicated, so we decided to use the former simplified model.

Summarizing, the problem in this section is to solve the equation 2.123, under the boundary conditions $\nabla\eta = 0$ (Neumann) for the erosion track, and $\eta = 0$ (Dirichlet) for others. The solution is the flux of the particles (in eq. 2.124) at the boundaries where the Dirichlet condition was applied.

2.6.3 Boundary integral equation

In the following part of this section, we discuss the boundary element method (BEM) to solve the problem submitted at the end of the previous subsection. The BEM method has been proposed by Brebbia and Wrobel [14]. We would like to note that the doctoral thesis of Wrobel [170] has been particularly consulted on applying this method to the axisymmetric coordinate.

We show the equation to be solved again:

$$\begin{aligned} \nabla^2\theta(x) + \frac{h(x)}{k} = 0 \quad &: \quad \text{in}\Omega \\ \theta = 0 \quad &: \quad \text{at}\Gamma \\ \nabla\theta \cdot \boldsymbol{n} = 0 \quad &: \quad \text{at}\Gamma' \end{aligned} \tag{2.125}$$

where Ω denotes the considering volume (3D), Γ and Γ' denote its boundaries (2D). To convert this problem into boundary integral equation, we introduce the function θ^* called "fundamental solution", which satisfies the following relation in Ω:

$$k\nabla^2\theta^*(x,y) + \delta^3(x-y) = 0 \tag{2.126}$$

In eq. 2.126, x and y are points in Ω. δ^3 is the Dirac's 3D delta function. Operator ∇^2 may effect either x or y. The solution of eq. 2.126 is:

$$\theta^*(x,y) = \frac{1}{4\pi r k}, \tag{2.127}$$

where $r = |x-y|$.

Next, we integrate the equation 2.125 using this fundamental solution in Ω, e.g.:

$$\int_\Omega \left(\nabla^2\theta(x') + \frac{h(x')}{k} \right) \theta^*(x,x') d\Omega(x') = 0. \tag{2.128}$$

$d\Omega(x')$ means that the integration is performed with x'. Since the term in the parenthesis is always zero in Ω, this equation is always satisfied.

If we execute the partial integration twice and use the relation in eq. 2.126, we obtain:

$$\frac{\theta(x)}{k} + \int_\Gamma \theta(x') q^*(x,x') d\Gamma(x') - \int_\Gamma q(x')\theta^*(x,x') d\Gamma(x') = -\frac{1}{k}\int_\Omega h(x')\theta^*(x,x') d\Omega(x'), \tag{2.129}$$

where $q = \frac{\partial}{\partial n}\theta$ and $q^* = \frac{\partial}{\partial n}\theta^*$. $\frac{\partial}{\partial n}$ denotes the derivative by x' along the boundary normal which heads for the outside of the chamber. In other words, it is:

$$\frac{\partial}{\partial n} = \boldsymbol{n} \cdot \nabla'. \tag{2.130}$$

where $\boldsymbol{n}$ is a surface normal heading for the outside of the boundary. Equation 2.129 means that once θ and q are determined on the boundary Γ, θ at any x in Ω can also be determined.

Now we apply the equation 2.129 for x_s on the boundary. In this case, θ^* and q are singular at $x_s = x'$, so we must introduce the coefficient $c(x_s)$:

$$c(x_s)\frac{\theta(x_s)}{k} + \int_\Gamma \theta(x') q^*(x_s,x') d\Gamma(x') - \int_\Gamma q(x')\theta^*(x_s,x') d\Gamma(x') = -\frac{1}{k}\int_\Omega h(x')\theta^*(x_s,x') d\Omega(x') \tag{2.131}$$

If the boundary at x_s is smooth, $c(x_s)$ is 1/2. If not, $c(x_s)$ is given by $1/2\pi$ times the solid angle of Ω from x_s.

Equation 2.131 gives the restriction to θ and q on the boundary in functional sense. In the problem of the second partial derivative equation, usually the value of either θ or q is given on the whole boundary, and the counterpart will be derived using equation 2.131. When both θ and q are determined on the whole boundary in such way, the value at any point inside the region can be derived using the equation 2.129.

2.6.4 Axisymmetric case

In the problem we are considering in this study, the system is axisymmetric. So we rewrite the equation 2.131 here using the polar coordinate. The radial, polar, and azimuthal coordinates of point x are denoted as $R(x)$, $\phi(x)$ and $Z(x)$, respectively.

$$\begin{aligned} c(x_s)\frac{\theta(x_s)}{k} &+ \int_{\bar{\Gamma}} \theta(x) \int_0^{2\pi} q^*(x_s, x') d\phi(x') R(x') d\bar{\Gamma}(x') \\ &- \int_{\bar{\Gamma}} q(x) \int_0^{2\pi} \theta^*(x_s, x') d\phi(x') R(x') d\bar{\Gamma}(x') \\ &= \int_{\bar{\Omega}} \frac{h(x_s)}{k} \int_0^{2\pi} \theta^*(x_s, x') d\phi(x') R(x') d\bar{\Omega}(x'). \end{aligned} \tag{2.132}$$

in which only θ^* and q^* are dependent on ϕ.

When we express the points x and x' in polar coordinate, the distance r between these two points is:

$$r = \left[R(x)^2 + R(x')^2 - 2R(x)R(x')\cos\{(\phi(x) - \phi(x')\} + \left\{Z(x) - Z(x')\right\}\right], \tag{2.133}$$

Hence, from eq. 2.127, the integration is:

$$\begin{aligned} \bar{\theta}^* &= \int_0^{2\pi} \theta^*(x_s, x') d\phi(x') \\ &= \frac{4K(m)}{\sqrt{a+b}}, \end{aligned} \tag{2.134}$$

where $K(m)$ is the complete elliptic function of 1st kind, and m is:

$$\begin{aligned} m &= \frac{2b}{a+b} \\ a &= R^2(x_s) + R^2(x') + [Z(x_s) - Z(x)]^2 \\ b &= 2R(x_s)R(x') \end{aligned}$$

Note that m has the value between $-1 \leq m \leq 1$.

Similarly, we also obtain:

$$\begin{aligned}\bar{q^*} &= \int_0^{2\pi} q^*(x_s, x')d\phi(x') \\ &= \frac{4}{\sqrt{a+b}}\left\{\frac{1}{2R(x')}\left[\frac{R^2(x_s)-R^2(x')+[Z(x_s)-Z(x')]^2}{a-b}E(m)-K(m)\right]n_R(x')\right. \\ &+ \left.\frac{Z(x_s)-Z(x')}{a-b}E(m)n_Z(x')\right\}, \end{aligned} \tag{2.135}$$

where $E(m)$ is the complete elliptic function of 2nd kind, n_R and n_Z are R and Z components of the normal unit vector at the boundary x', respectively.

Substituting eqs. 2.134 and 2.135 into eq. 2.132, we finally obtain the expression:

$$\begin{aligned} c(x')\theta(x_s) &+ \int_{\bar{\Gamma}} \theta(x')\bar{q^*}(x_s, x')R(x')d\bar{\Gamma}(x') \\ &= \int_{\bar{\Gamma}} q(x')\bar{\theta^*}(x_s, x')R(x')d\bar{\Gamma}(x') + \int_{\bar{\Omega}} \frac{h(x')}{k}\bar{\theta^*}(x_s, x')R(x')d\bar{\Omega}(x'). \end{aligned} \tag{2.136}$$

2.6.5 Boundary element method

Boundary element method (BEM) is a technique to solve the boundary integral equation in which you discretize the boundary into nodes, approximate $\bar{\theta}$ and $\bar{q}$ on it with simple functions including a few parameters, build and solve simultaneous linear equations of these parameters, and determine the approximate solutions for $\bar{\theta}$ and $\bar{q}$. With BEM, we first split the boundary Γ into nodes. In this study, we assume that each node has line form for simplicity.

For the "simple functions" on the nodes, there are some candidates depending on the number of parameters, e.g.:

- constant element (with one parameter)
- linear element (with two parameters)
- parabolic element (with three parameters)

Note that the "element" denotes the type of approximate function defined on each boundary node, and has nothing to do with the form of the node. Also note that you can select the constant element for $\bar{\theta}$ while the linear one for $\bar{q}$, and the like. In the following of this study, we use the constant element for both $\bar{\theta}$ and $\bar{q}$.

We split the boundary $\bar{\Gamma}$ into n linear nodes, and denote them as $\bar{\Gamma}_i\,(i = 1 \ldots n)$. The both ends of the $\bar{\Gamma}_i$ are denoted by $x_1^{(i)}$ and $x_2^{(i)}$. 1 and 2 are chosen such that the region $\bar{\Omega}$ comes left side of the vector $x_2^{(i)} - x_1^{(i)}$. As the representative point of $\bar{\Gamma}_i$, we choose:

$$x^{(i)} = \frac{x_1^{(i)} + x_2^{(i)}}{2} \tag{2.137}$$

On $\bar{\Gamma}_i$, $\bar{\theta}$ and $\bar{q}$ are approximated by the constant value θ_i and q_i, respectively.

The integration on the boundary (eq. 2.136) can be split into these nodes:

$$\begin{aligned} c(x^{(i)})\theta_i &+ \sum_j \int_{\bar{\Gamma}_j} \theta_j \bar{q^*}(x^{(i)}, x') R(x') d\bar{\Gamma}(x') \\ &= \sum_j \int_{\bar{\Gamma}_j} q_j \bar{\theta^*}(x^{(i)}, x') R(x') d\bar{\Gamma}(x') + \int_{\bar{\Omega}} \frac{h(x')}{k} \bar{\theta^*}(x^{(i)}, x') R(x') d\bar{\Omega}. \end{aligned} \tag{2.138}$$

Since θ_j and q_j can be moved outside the integration, equation 2.138 becomes:

$$c_i \theta_i + \sum_j q^*_{ij} \theta_j = \sum_j \theta^*_{ij} q_j + B_i \tag{2.139}$$

where

$$c_i = c(x^{(i)}) \tag{2.140}$$

$$q^*_{ij} = \int_{\bar{\Gamma}_j} \bar{q^*}(x^{(i)}, x') R(x') d\bar{\Gamma}(x') \tag{2.141}$$

$$\theta^*_{ij} = \int_{\bar{\Gamma}_j} \bar{\theta^*}(x^{(i)}, x') R(x') d\bar{\Gamma}(x') \tag{2.142}$$

$$B_i = \int_{\bar{\Omega}} \frac{h(x')}{k} \bar{\theta^*}(x^{(i)}, x') R(x') d\bar{\Omega}. \tag{2.143}$$

In the current problem, either θ_i or q_i is known on every node. Hence eq. 2.139 can be regarded as the simultaneous linear equations.

Now we define:

$$\begin{aligned} H_{ij} &= \begin{cases} c_i + q^*_{ij} & (i = j) \\ q^*_{ij} & (i \neq j) \end{cases} \\ G_{ij} &= \theta^*_{ij}. \end{aligned} \tag{2.144}$$

Using these, equation 2.139 can be expressed in the matrix form:

$$\boldsymbol{H\Theta} = \boldsymbol{GQ} + \boldsymbol{B}. \tag{2.145}$$

Since N_1 of $\boldsymbol{\Theta}$ and N_2 of $\boldsymbol{Q}$ should be known ($N_1 + N_2 = N$), this simultaneous equations can be solved.

In the diffusion problem of the sputtering deposition, source term is given by the sum of delta functions, as shown in 2.119. It can be regarded as the sum of ring sources with constant intensity of $1/2\pi R(x)$ in the axisymmetric coordinate. Therefore, $h(x')/k$ becomes:

$$\frac{h(x')}{k} = \sum_{\text{Thermalized}} \frac{1}{R(x_p)} \delta^2(x_p - x'). \tag{2.146}$$

Hence the integrations in $\bar{\Omega}$ in equation 2.143 are simply replaced by the function value at x_p, which gives:

$$B_i = \sum_{\text{Thermalized}} \bar{\theta}(x^{(i)}, x_p). \tag{2.147}$$

2.6.6 Comparison with MC method

To check the validity of this diffusive approach, comparison with the MC method was performed. Results are shown figure 2.6. As described above, axisymmetric chamber was assumed in both calculations, and its boundary was split into nodes as shown in the bottom-left subfigure in fig. 2.6. The form of this chamber boundary is basically the same with the one actually used in the experiments (see section 3.1.2), where the nodes from 1 to 9 represent the target surface, and nodes from 31 to 45 represent the substrate holder.

A source of particles was set in this chamber, and both simulations were performed. Several source positions were tested, and three of them are shown in figure 2.6. By taking the center of the target surface as an origin, point A is at $(R, Z) = (0, 4)$, B is at $(4, 2.5)$, and C is at $(2, 1)$ (in cm unit). Please note again that we are considering the axisymmetric case. Therefore, that the source is actually a ring form, and its strength is proportional to R^{-1} if we see it in 3D system.

MC calculation was performed for 10^5 of Cu atoms which started at the source position with zero kinetic energy. The argon gas environment was assumed with the temperature of 400 K and the pressures of 2, 5 and 10 Pa. Born-Mayer potential was used for the scattering potential, and the collision/scattering events was treated as described in section 2.5. Since the gas motion is also included in this scattering model, the Cu atoms would start the motion by the collision impact by an ambient argon gas atom.

Results of the calculation are shown in subfigures of A, B and C corresponding to the location of the particle source. The deposition flux given by BEM calculation is represented in red-broken line, while that of MC is in marks. The agreement of both is fairly good, but is relatively poor at nodes where the distance from the particle source is near. It may reflect the "constant element" model of the BEM we used, in which the flux is assumed to be constant on each node, and representative point of each node (x_i in eq. 2.137) is located at the center of them. At nodes near the source, the relative difference of the distance between the source and the boundary becomes large, hence the flux should be over- or under-estimated. If we would split the node finer, or would use "linear element model" or "parabolic element model" for the flux function, this problem might be overcome.

The edge effect of the BEM [14], which is originated by the singularity of the diffusion equation there, also makes worse the agreement of the BEM result at corner nodes (c.f. nodes 9, 10, 37 and 38 in this case). But in most cases where the MC simulation is applied, the interest is mainly in a uniformity of the profile in the midst of the substrate holder (*i.e.*, away from edges or corners), hence we probably don't have to get into this problem so seriously.

It is also observed that the higher the gas pressure the better the agreement becomes. It is because of the shorter mean free path in high pressures, which is infinitesimal in BEM case. The error caused by this effect will be reduced by setting the lower thermalization threshold energy, where more particles reach the boundary in the MC step. It will be discussed later in the next section.

Both calculations were executed by a PC with Intel Pentium III (750 MHz). The computation time is summarized in table 2.2. The reduction of the computation time is obvious. In the simulation of actual sputter deposition process, you have to sum up the right hand side of the equation 2.146 for every thermalized particle. Therefore, when we obtain the elapsed time of BEM, $\bar{\theta}(x^{(i)}, x_p)$ is re-calculated 10^5 times (same with the particle number in MC) and summed

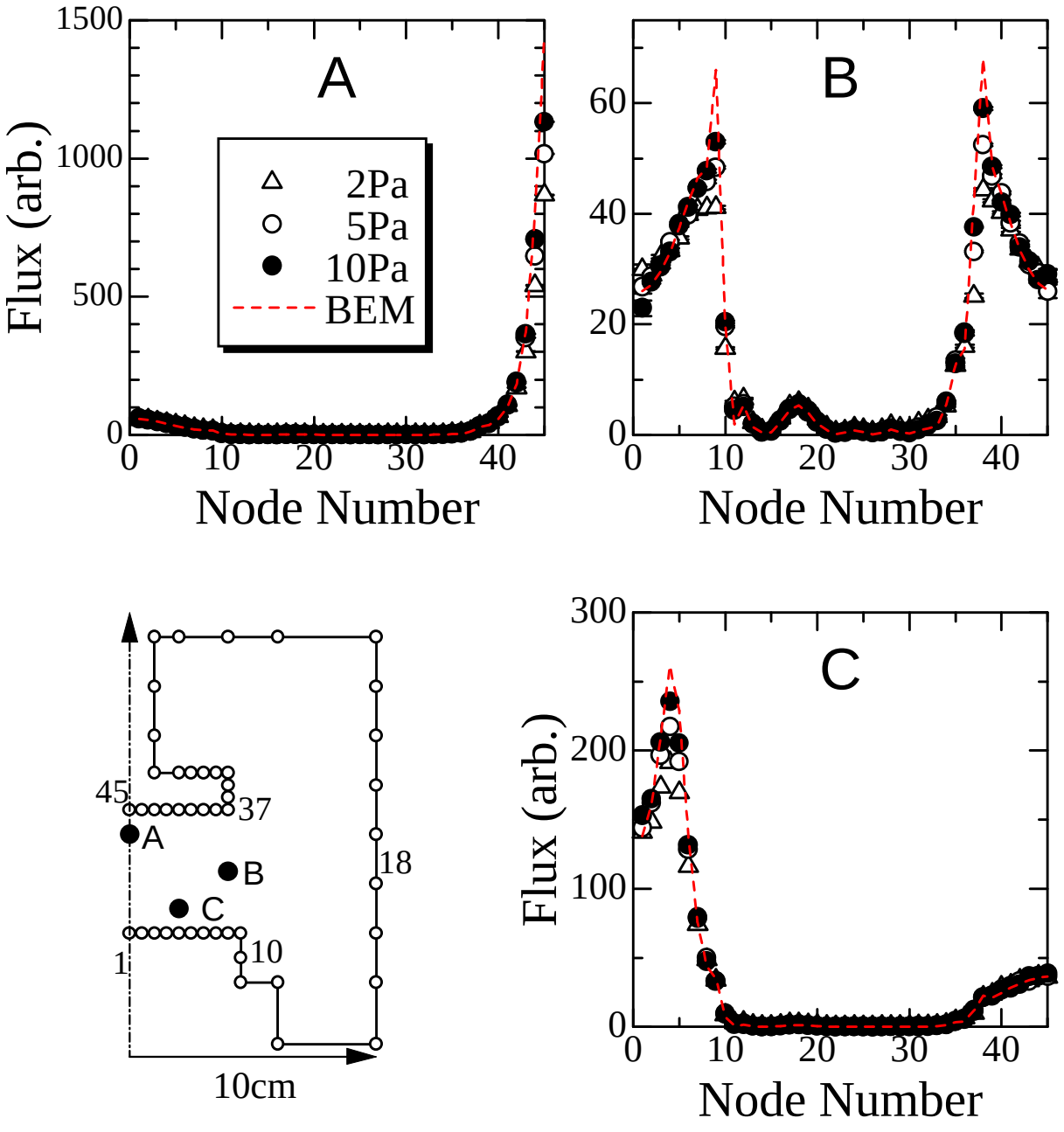

Figure 2.6: Comparison between the BEM simulation with MC. Bottom-left shows the cross section of axisymmetric chamber, where three points of A, B and C denotes the particle source.

Source	BEM	MC (2 Pa)	MC (5 Pa)	MC (10 Pa)
A	18.3	93	401	1375
B	18.6	142	689	2519
C	16.2	89	386	1306

Table 2.2: Times consumed to calculate the result of figure 2.6. The values are in seconds.

up at each nodes.

2.6.7 Thermalization threshold

The BEM procedure described above is used combining with the MC method in the actual simulation program. At first, the particle ejected from the target is treated by MC, where it is gradually decelerated by the collision with gases. When its energy becomes lower than the "thermalization threshold" specified before the simulation, the MC step for that particle is over and the particle position is recorded as $\boldsymbol{x_i^{Th}}$, which is regarded as one of the particle sources and used in the right hand side of eq. 2.119. After the MC calculation for all the particles is over, BEM calculation is performed.

The problem arisen here is how to determine this thermalization threshold. When you select a large value, MC step will be quickly over and the computational time can be reduced. But the motion of the sputtered particle may not go into the random diffusion at such high energy, so the accuracy of the calculation result may be degraded. Hence we tried several calculations by changing this threshold, and evaluated the calculation time and the profile of the particle flux on the substrate holder. For the MC step, procedures described through 2.2 –2.5 are applied (They will be summarized in section 3.1.2 in the next chapter). Copper and argon are selected as the target material and the sputter gas, respectively. As a sputter chamber, the left bottom of fig. 2.6 is used.

Figure 2.7 (a) shows the dependence of the computation time to calculate the thickness profiles for 10^5 of sputtered atoms on the thermalization threshold. Horizontal axis is the threshold energy in the unit of kT, where T is the gas temperature set to 400 K here. Cases of gas pressures of 2 Pa and 10 Pa are presented. The computer used for this calculation is IBM PC clone with Intel Pentium III (733 MHz) CPU, the same one used in the previous section 2.6.6. The computation time was about 5–20 min, and increased as the the threshold energy decreased. On comparing the different pressures, the 10 Pa case showed steeper increase at lower threshold energy region. At high threshold energy as high as 1 kT, most of the particles are thermalized shortly after the sputtering ejection. It only needs a few times of collision, so the computation time does not differ so much. On the other hand, as the threshold becomes smaller, more collisions are required for the particle to have —accidentally— smaller energy than the threshold.

In lower pressures, where the mean path of the particle becomes longer, significant part of the particles may reach the chamber wall before they thermalized. Therefore, less calculation

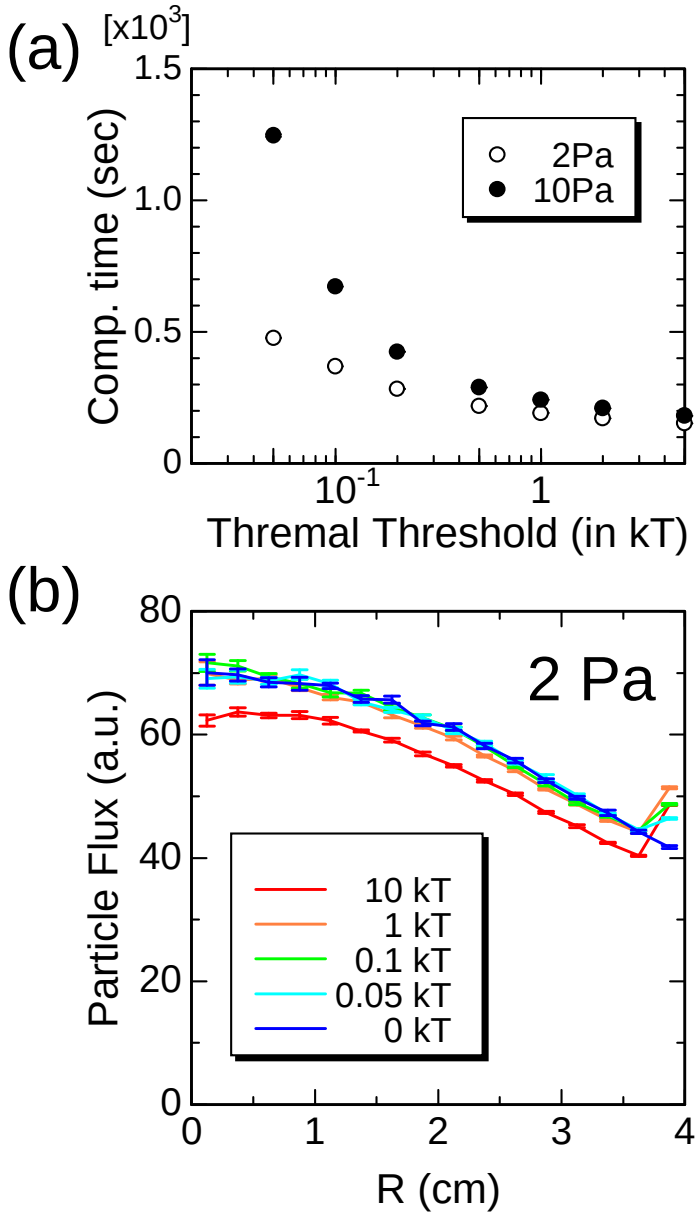

Figure 2.7: Effect of the thermalization threshold on the particle transport simulation combining MC and BEM. Upper figure is the calculation time dependence on the threshold, while the lower figure gives the resultant flux dependence at substrate.

time is needed. Moreover, at higher pressures, sputtered particles are more likely to stay near the erosion track because the diffusion coefficient becomes small. So the particles tend to go back and stick to the erosion track, where they will be re-ejected. It may also result in the computation time consumption. When threshold energy was set to 0 K (in other words, BEM treatment was used and only MC calculation was performed), computation time was 674 ± 3 (s) for 2 Pa and 15355 ± 65 (s) for 10 Pa.

In figure 2.7 (b), flux of sputtered particles at the boundary nodes on the substrate holder face is displayed. The substrate holder face corresponds to the node 37 to 45 in figure 2.6 (a) (the mesh fineness has been modified, though). The horizontal axis is the distance from the symmetrical axis. When the threshold energy is greater than 1 kT, the flux becomes smaller. On the other hand, for the smaller energies, the flux values stay within the calculation error, and are also identical to the result of zero threshold energy case (*i.e.*, no BEM case). The flux at the node near the corner edge ($R = 3.75$ cm) shows a slightly higher flux than its neighbors, which may be caused by the edge effect originated in the BEM calculation as mentioned earlier. The smaller flux at higher threshold energy ($kT \sim 10kT$) is because of the following reason: the sputtered copper atoms are considered to be thermalized near the target (and treated as the particle source of random diffusion), before they completely lose the initial momentum toward the substrate. In other words, the centroid of the particle source profile becomes (mistakenly) far away from the substrates in higher threshold energy cases.

Summarizing, it is preferable to set the thermal threshold to lower value for the accurate simulation, but more computation time is necessary in this case. In this study, we determined the threshold at $0.1kT$ as the compromise of these two requirements.

Chapter 3

Results and Discussions

In this chapter, we perform the simulation based on the theory described in the previous chapter, and show its results. By comparing them with experiments, the validity of models and assumptions is checked out. At the same time, dependence of film properties on deposition conditions (especially gas pressure) are studied with both experiment and simulation, and the origin of these behaviors is discussed from the viewpoint of the particle transport.

In 3.1, the experimental apparatus used in this study is briefly described. At the same time, methods and assumptions used in the simulation are summarized. For the latter, the discussion in the previous chapter is referred from each item.

In 3.2, we simulate the behaviour of high energy copper atoms injected into argon gas. Time evolutions of copper atoms in both velocity and real spaces are visualized. Especially, the effect of the thermal motion of colliding gas atoms is studied. By introducing the gas motion using the method in section 2.5, it is shown that the velocity distribution of sputtered atoms approaches to the Maxwellian with the same temperature of the ambient gas after some period of time. On the contrary, if the gas motion is neglected, the speed of the sputtered atom is monotonically decreased.

In 3.3, sputter deposition process of the copper film is simulated. Deposition experiment is actually performed, and the reproducibility of the thickness profile of the copper film by the simulation is studied. The dependence of the profile on the distance between the chamber wall and the substrate is investigated. The pressure dependence of the profile is also studied by means of the thickness ratio between two substrate holder faces facing toward / away from the target (BFR), which has been proposed by Motohiro [90]. He has found that the relative thickness on the back face shows a maximum in the middle pressure region by experiment. This behaviour is reproduced by our simulation model, and the reason of the decrease (and the approach to constant) in high pressure region is discussed.

In 3.4, we investigate the compositional deviation of LaB_6 sputter deposited films from the target, and its dependence on gas pressure. Its behaviour is resemble to the previous studies mentioned in section 1.5; as the gas pressure increases from the very low pressure region, the film content of the lighter element (boron in this case) decreases at first, passes a minimum, and recovers to the stoichiometry at high pressures. It is reproduced both by the experiment and the simulation. Using the simulation, it is shown that this behaviour is originated from the

mass difference between La and B, which affects the scattering process of these atoms with the argon gas atom.

Finally in 3.5, we introduce a novel method to calculate the spatial density of sputtered atoms using the MC simulation. As will be shown in section 3.2, by introducing the thermal motion of colliding gas atoms, the sputtered atom does not stop and its motion can be traced until they reach the chamber wall. With this method, the residual time of each sputtered atom is calculated. Combining this residual time with the deposition rate (*i.e.* the particle flux on the wall) obtained by the experiment, atomic density can be deduced. We show the calculation results for the Cu sputtering plasma, and discussed its correspondence with the optical emission from copper neutral atoms in the discharge plasma.

3.1 Experimental Apparatus and Simulation policies

3.1.1 Sputtering chamber

Sputter chamber used in this study is shown in figure 3.1. This is based on a commercial sputter deposition system (Nichiden Varian: SPF-210B), with some extra features being added. Inner diameter of the chamber is 20 cm, and the height is 16.5 cm. Target is a disk form whose diameter is 8 cm. Substrate holder is located above the target, and the distance between them is variable. Because of the shutter motion, the symmetrical axis of the target and the substrate holder displaces from that of the chamber by 3 cm.

A SmCo magnet and a steel yoke are located under the target to form a slightly-unbalanced magnetron field. The field strength just above the target is about 0.2 T. With this magnetic field, erosion track was formed on the target as a ring with 2 cm in radius. In this study using Cu and LaB_6 as target materials, the track had about 2 cm width in both cases. The depth profile of them are shown in figure 3.2. Note that they were formed by the deposition experiments in various discharge conditions, hence they should be regarded as some kind of average.

Argon was used as a discharge gas, and its pressure during the sputtering was changed from 1 to 20 Pa. The gas pressure was monitored by a Schultz gauge. Flow rate of the argon gas was kept at 10 sccm with a mass flow controller (Nippon-Tylan SG-3Al-000), and the pressure was set by throttling the conductance of two evacuation valves connected in parallel to the large flow-rate type turbo molecular pump (Osaka Vacuum TG200). Both DC and RF discharges can be generated by switching the DC power source (Advanced Energy MDX-1.5k) and the RF power source (Tokyo High-Power model A300).

On comparing experimental results with simulations, we should note that the measure of discharge gauge is not the pressure itself but the particle density [101]. Between the gauge value of the pressure P_G and the gas density n_G, the following relation can be applied:

$$n_G = \frac{P_G}{kT_G}, \tag{3.1}$$

where T_G is the specific temperature given by the maker of the Schultz gauge, which is 296 K in the model we used.

Though the gas density is more essential than the pressure for the particle transport, it is rather unfamiliar in experimental fields. In the following discussion, therefore, we use the eq. 3.1

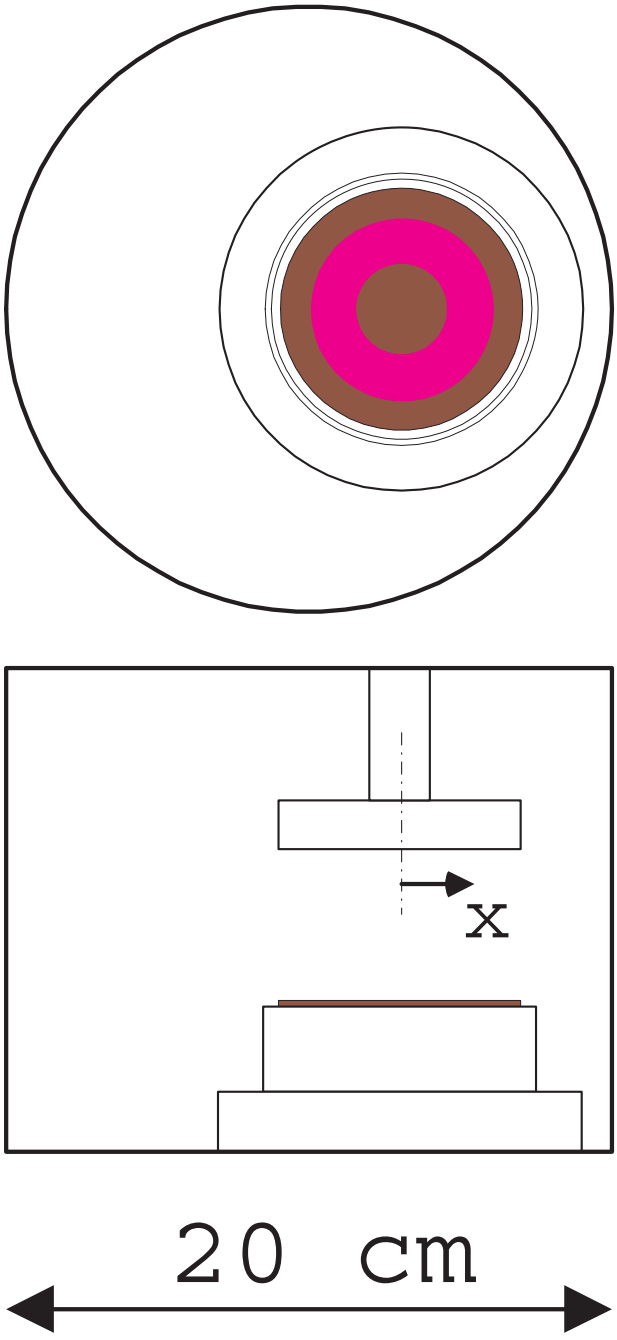

Figure 3.1: Sputter chamber for film deposition experiments.

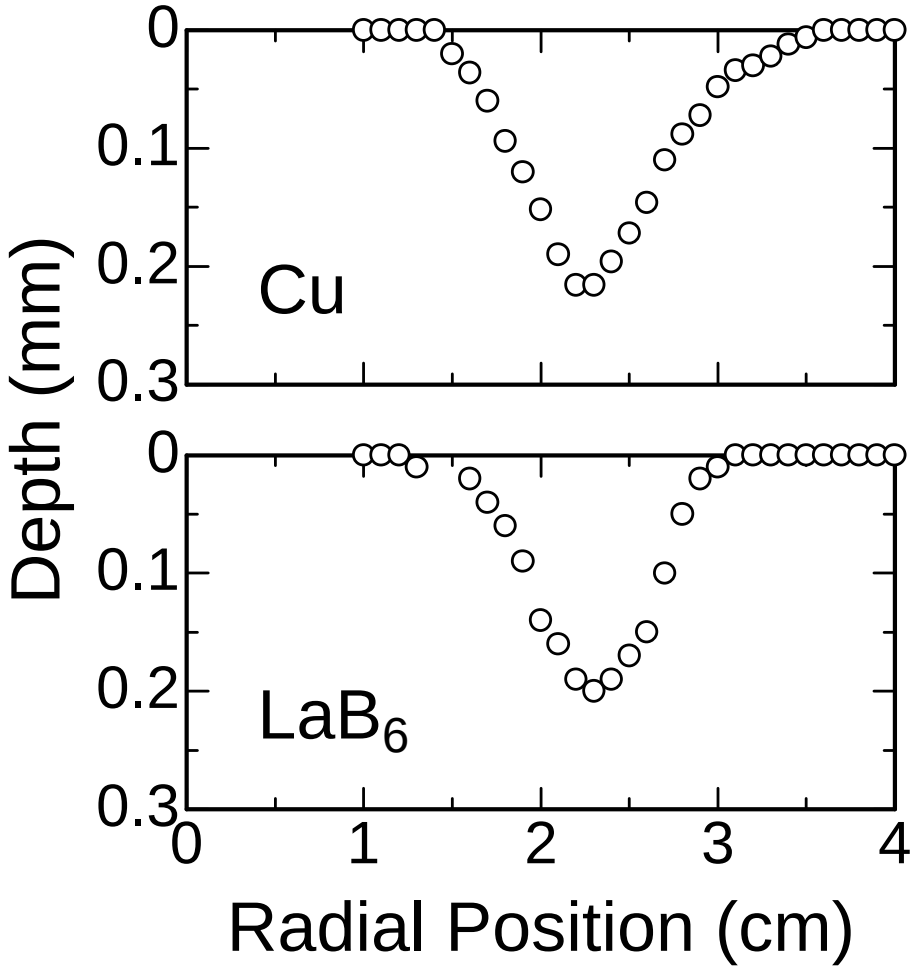

Figure 3.2: Radial depth profile of erosion tracks formed on Cu and LaB_6 targets.

inversely, and display the value in pressure unit. So if the pressure value appears in the text in this chapter, please regard it as the density implicitly.

3.1.2 Summary of simulation policies

In this section, models, methods and assumptions of the simulation used in this study are summarized. Most of them have already been described in the previous chapter. Citation to them are added on each item if possible.

1. The sputter chamber (*i.e.*, boundary) is assumed to be axisymmetric to simplify the simulation. Note that in the experimental apparatus, symmetric axis of the target–substrate system is 3 cm apart from that of chamber.

2. All the sputtered particles are atoms. It is partly because that the collision and scattering between molecules and clusters are difficult currently. But for the cases covered in this study (Cu and LaB_6), we believe this assumption is adequate.

3. The ejection position of sputtered atoms on the target is determined so that the depth profile of the erosion track is reproduced (section 2.2.1). These depth profiles used in this study are shown in figure 3.2, which have been actually measured on each target. If the sputtered atom comes back to the erosion track and sticks there during the Monte Carlo step, it will be re-ejected from there immediately.

4. On ejection from the target, the angle and energy distributions of sputtered atoms are ruled by the cosine distribution and the Thompson's formula, respectively (sections 2.2.2 and 2.2.3).

5. The pressure and the temperature of the ambient gas are uniform in the chamber.

6. The mean free path (MFP) of the sputtered atom is determined using the method described in section 2.5.1, and the actual free path on each event is deduced by the method in section 2.3.1 with this MFP value.

7. The speed and the direction of the colliding gas atom to the sputtered atom are determined using the method in section 2.5.2.

8. The scattering between the sputtered atom and the gas atom are calculated based on the potential scattering framework. The Born-Mayer potential with the parameters given by Abrahamson is used as the scattering potential (section 2.3.3).

9. The speed and the direction of the sputtered atom after the scattering is determined as described in section 2.5.3.

10. When the sputtered atom arrives on the chamber boundary, it sticks there with the probability of unity (section 2.4). However, if the boundary belongs to the erosion track region, the atom will be re-ejected as mentioned above.

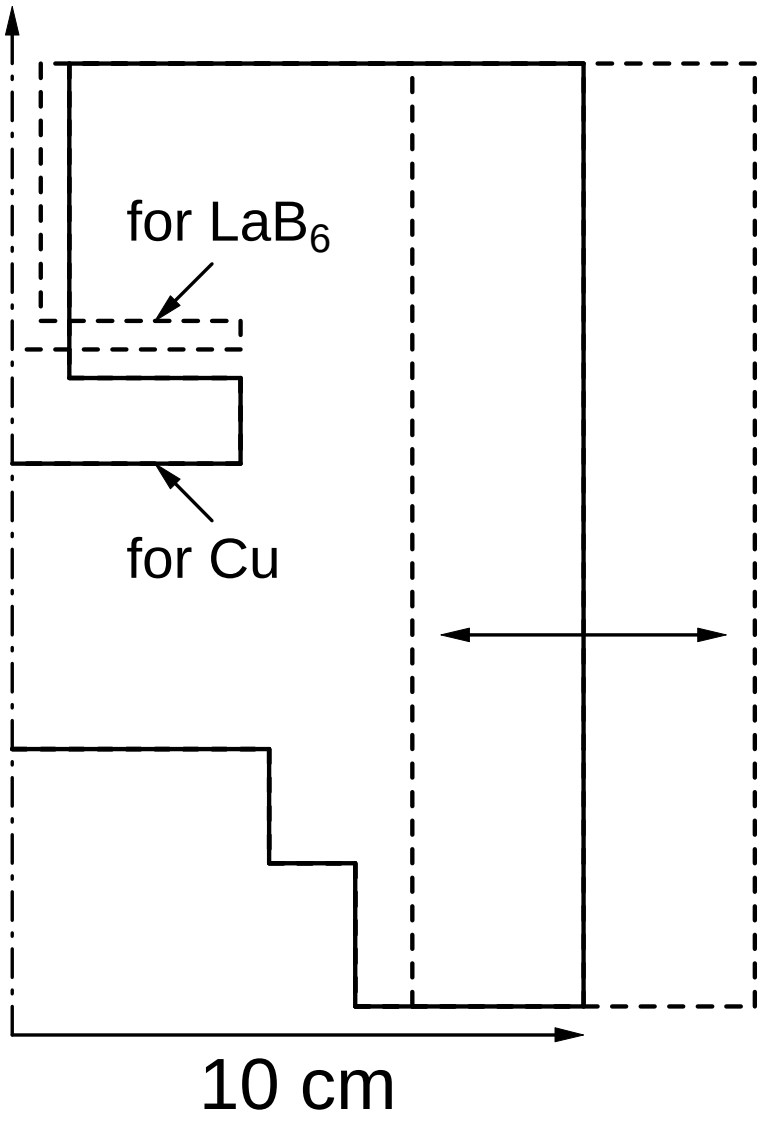

Figure 3.3: Axisymmetrical chamber boundary used with MC simulation. Location (and shape) of the substrate holder differs for LaB_6 (3.4) and for Cu (3.3 and 3.5) depositions. Radius of the chamber wall is changed to study the effect of it in 3.3.

11. When the kinetic energy of the sputtered atom becomes less than the specified threshold, it is regarded as "thermalized" there, and treated as the particle source with the strength of unity. These sources are summed up, and the diffusion equation corresponding to this source term is solved after the MC calculation is over. The particle flux deduced by this procedure is added to the flux of the atoms arrived to the wall before the thermalization (section 2.6.2).

12. The thermalization threshold energy is assumed to be 0.1 kT, where k is the Boltzmann's constant and T is the gas temperature (section 2.6.7).

13. The boundary condition of the diffusion equation on normal boundary is the Dirichlet condition of zero density, and the one on the erosion track is the Neumann condition with zero flux (section 2.6.2).

14. The diffusion equation is solved by the Boundary Element method (BEM) as shown in section 2.6.5.

3.2 Deceleration and diffusion of high energy atoms in gases

In this section, we simulate the behaviour of high energy atoms injected into gas environment; deceleration by the collision with gas atoms and diffusion. Especially, we discuss the difference between two cases: whether the thermal motion of gas atoms is included or not. The situation with copper atoms and argon gas was studied.

On simulating the time evolution of the velocity distribution, 5000 copper atoms were injected into the gas at 0 s, to the positive direction of the z axis with 5 eV of kinetic energy. Then, the snapshots were taken after some periods of time. On calculating the elapsed time, we assumed that the copper atom changed the speed just instantly at collision points, and flew at the constant speed between two collisions (in other words, integration of the time in potential scattering framework was not made). The gas density is set to 10 Pa in the unit of vacuum gauge indication (see eq. 3.1).

Figure 3.4 shows the result. Snapshots taken at 2, 10 and 50 μs are plotted in the velocity space. Figures (a), (c) and (e) are the results considering the gas motion with temperature $T_g = 400$ K, while (b), (d) and (f) are the ones calculated with $T_g = 0$, *i.e.*, neglecting the gas motion. The range of each axis (V_x, V_y and V_z) in figure 3.4 is taken from -3000 to 3000 m/s. The speed of the copper atom at kinetic energy of 5 eV is about 3900 m/s. And if copper atoms are ruled under the Maxwellian with the temperature 400 K, their mean speed is $\sqrt{8kT/\pi m} = 365$ m/s.

Cu atoms are put at $V_z = 3900$ m/s at 0 s, and their directions are quickly scattered. If you estimate the effective collision radius between Cu and Ar atoms to be 3 Å (see figure 2.2), the mean free path of copper in 10 Pa (gauge value) of Ar gas is deduced to be about 1.4 mm from eqs. 2.26 and 3.1. Therefore, in 2 μs, copper atom of 3900 m/s speed will collide 5 times with argon gas atoms. Actually, since the speed of the copper atom decreases by each collision, this may be reduced to 3 times or so.

After that, the velocity distribution converges toward the origin of the velocity space as the time goes by. The cases with $T_g = 400$ K and with 0 K look similar at 10 μs, while these are

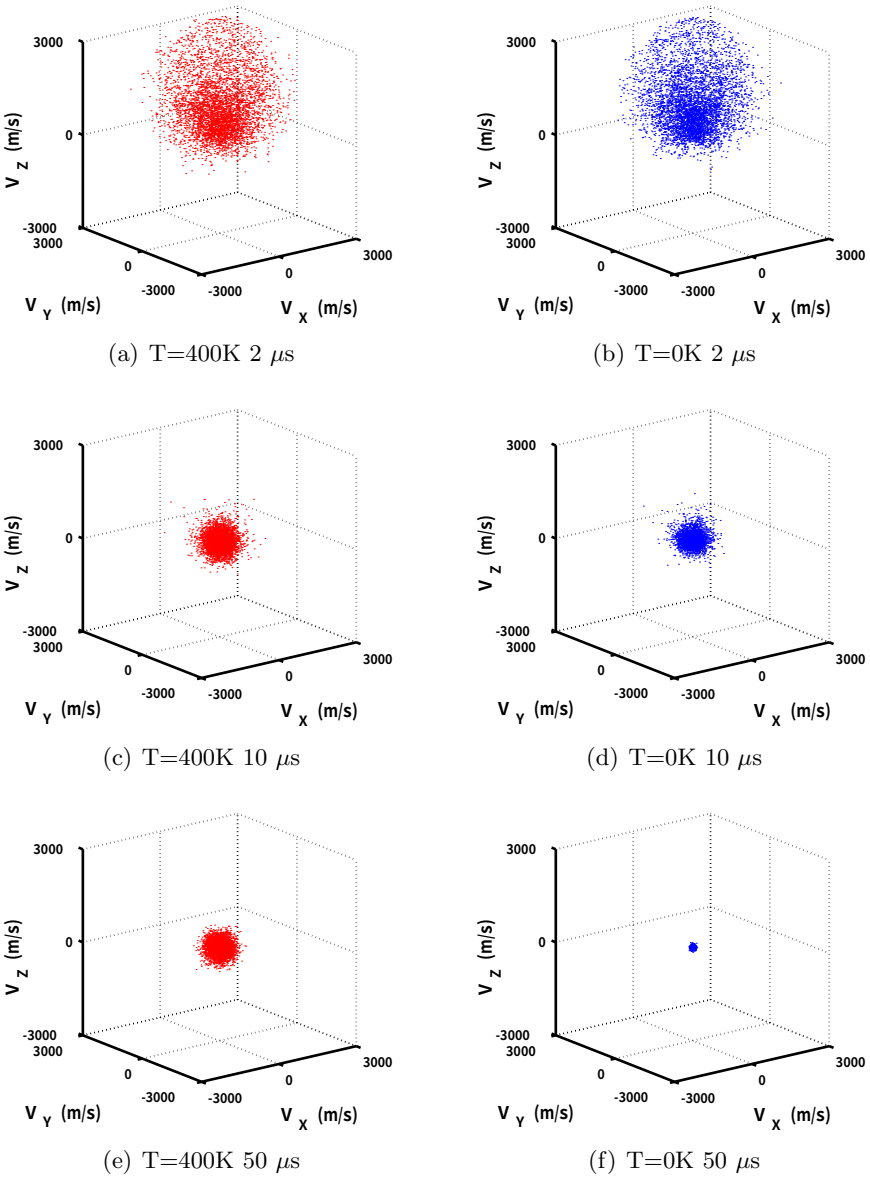

(a) T=400K 2 μs (b) T=0K 2 μs

(c) T=400K 10 μs (d) T=0K 10 μs

(e) T=400K 50 μs (f) T=0K 50 μs

Figure 3.4: Time evolution of the velocity space distribution of 5000 Cu atoms injected with 5 eV into Ar at 10 Pa. Left subfigures ((a), (c) and (e)) are the cases where the gas temperature is 400 K, while the right ones ((b), (d) and (f)) are the cases with the gas temperature is 0 K (e.g., gas motion is neglected).

clearly different at 50 μs. In the former case ($T_g = 400$ K), the velocity distribution keeps some size as large as the thermal speed (385 m/s), while in the latter case ($T_g = 0$ K), the distribution continuously converges into a very small volume. With finite gas temperature, the velocity of copper should approach to the equilibrium with the gas. On the other hand, if the gases are immobile, copper atoms always decelerated on each collision event and their speed approaches to zero.

Figure 3.5 shows the elapsed time dependences of the speed distribution of these copper atoms ("speed" means the absolute value of the velocity). Figure 3.5 (a) is the case where the argon gas temperature is 400 K, corresponding to the figure 3.4 (a), (c) and (e). On the contrary, figure 3.5 (b) is the zero gas temperature case, corresponding to the figure 3.4 (b), (d) and (f). Times when the snapshot is taken are in the range of 2–50 μs, which are also the same with figure 3.4. On calculating the profiles shown in figure 3.5, however, 10^5 of particles are traced.

The function drawn in a solid line in fig. 3.5 (a) is the Maxwellian appeared in eq. 2.70:

$$f(v_g) = \frac{4}{\sqrt{\pi}}\alpha^{\frac{3}{2}} {v_g}^2 \exp\left(-\alpha {v_g}^2\right), \tag{2.70$'$}$$
$$\alpha = \frac{m}{2kT}$$

with m to be the atomic mass of copper ($63.54 \times 1.661 \times 10^{27}$ kg) and with T to be the same temperature with gas (400 K). You can see that the speed distribution of copper atoms is reproduced very well by the simulation considering the thermal motion of gases.

The velocity distribution $f_0(v_p)$ in $T_g = 0$ K environment seems to obey the scaling law:

$$\frac{f_0(\gamma v_p)}{\gamma} = \text{const} \tag{3.2}$$

with the scaling parameter $\gamma(t)$, which is found to have the time dependence

$$\gamma \propto t^{1.2\sim1.3}. \tag{3.3}$$

What determines this time exponent is left unclear at this time of writing. If argon atom is stationary, the rate of energy decrease is deduced from the scattering angle. As the copper speed (and kinetic energy) decreases, tail of the Born-Mayer potential becomes important, and the same scattering angle is obtained with larger collision parameter. This reduces the mean free path of the copper atom, and enlarge the time exponent. On the contrary, the time between the collision becomes larger as the speed decreases. This diminish the exponent. These two effects may compete each other and determine the time exponent.

The propagation process of copper atoms in *real* space has also been investigated, and are displayed in figure 3.6. The conditions are the same with fig. 3.4, 5000 of 5 eV copper atoms are injected at 0 s, along the positive direction of the z axis from the origin. Argon gas temperature is 400 K and the pressure is 10 Pa. x, y and z axes in fig. 3.6 are the coordinates in real space. Their range is from -5 to 5 cm, which is comparable with the size of the conventional sputter chamber. The allocation of subfigures is also identical with fig. 3.4; left sequence (a), (c) and (e) are the cases where the argon gas temperature is 400 K, while the right (b), (d) and (f) are

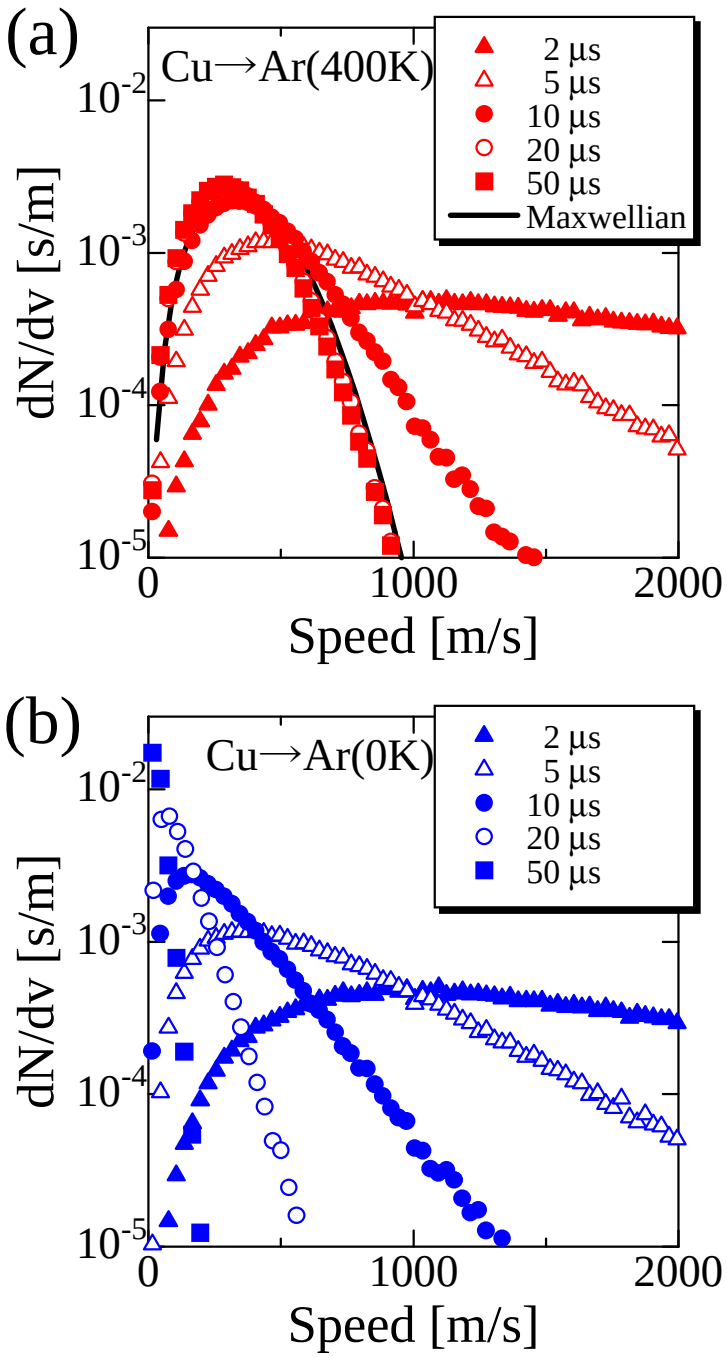

Figure 3.5: Time evolution of the energy distribution of Cu atoms injected at 0 s with 5eV into Ar gas of 10 Pa.

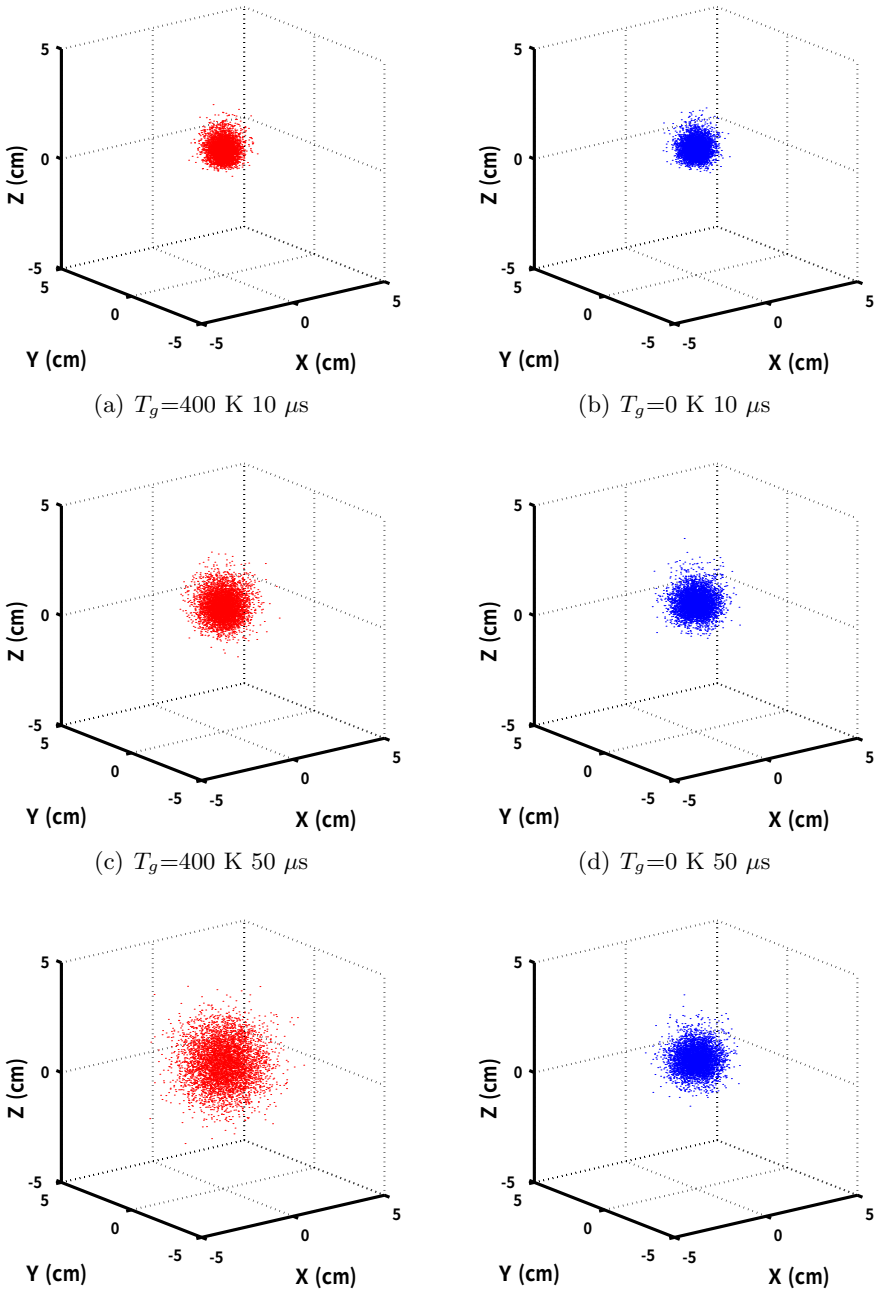

(a) T_g=400 K 10 μs (b) T_g=0 K 10 μs

(c) T_g=400 K 50 μs (d) T_g=0 K 50 μs

(e) T_g=400 K 200 μs (f) T_g=0 K 200 μs

Figure 3.6: Time evolution of the real space distribution of 5000 Cu atoms injected into Ar at 10 Pa.

the one with 0 K. The times to take the snapshots in this figure are 10, 50 and 200 μs. Note that they are different from those in fig. 3.4 to make clear the difference between two cases.

You can see in $T_g = 0$ K case that the position profile at 200 μs (f) is not so different from the one at 50 μs (d). On the other hand, in $T_g = 400$ K case, diffusion of copper particles proceeds until 200 μs. As shown in fig. 3.5, the difference between these two temperatures becomes significant since 50 μs or so. The velocity distribution approaches to the Maxwellian in 400 K case, while it converges to $v_p = 0$ by neglecting the gas motion. In the latter case, therefore, copper atoms are frozen at some point, and do not move anymore from there.

From the standpoint of the particle transport simulation, this "freeze" of copper atoms may not be the major problem if only the atomic flux on chamber wall is necessary, since the diffusion stage can be treated with the framework described in 2.6 using the Poisson's equation. In this framework, copper atoms, which have high energy initially, are decelerated during the ballistic transport process, and turn into the random diffusion. If the positional distribution, which starts from this frozen profile and evolutes under the diffusion equation in some period, would be similar to the one obtained in the finite temperature case, the flux profile in both cases should look alike each other.

It should be noted, however, that the gas motion *must* be incorporated when you have to consider the motion of sputtered atoms including the time parameter (as will be discussed in section 3.5). If you neglect it, sputtered atoms will stop inside of the chamber, hence it is completely impossible to deduce the time corresponding to the transport and/or diffusion.

3.3 Thickness profile of sputtered Cu films

In this section, we simulate the actual sputter deposition process, and compare the thickness profile with experiments. As in the case for general sputtering apparatus, the sputter target and the substrate holder is placed facing to each other in this study. It is shown that the thickness profile is affected by the distance between this target–holder system and the chamber wall. The reason of this effect is discussed from the standpoint of the particle transport.

During the sputter deposition at pressures not so low, films also deposit on chamber walls which cannot be seen directly from the target, by the diversion of sputtered atoms deflected by collisions with gas atoms. It has been reported by Motohiro that the thickness ratio on the back and front faces of the substrate holder (BFR) shows a interesting pressure dependence [90]. He observed that this BFR took a maximum at midst pressure and decreased in higher pressures. But in his study, the reason was not fully understood because of the limitation of simulation model and the computer performance. In this section, we apply our novel methods to this problem, and discuss the reason of it.

3.3.1 Experiment and simulation

The deposition experiment was performed with the apparatus described in section 3.1.1. Target was a copper metal disk with 4N purity. Argon was used as the sputter gas, and the discharge was generated with the DC power source. Corning 7059 glass substrates were used, which were set on both faces (front/back) of the substrate holder shown in fig. 3.1. Film thickness was measured by the multiple interferometer. Step was prepared by the cover glass mask with

0.12 mm thickness. To evaluate the effect of the neighbor wall, thickness profile was taken along the line passing both the symmetric axis of the substrate holder and that of the chamber. The former was taken to be the origin, and the positive direction of the measurement axis (x axis in figure 3.1) was chosen heading toward the nearer wall. Since these centers are eccentric, the thickness profile along the x axis is also asymmetric by $x = 0$.

The simulation was carried out in a similar manner with the previous section 3.2, where we have seen the behavior of copper atoms injected into the free space filled with argon gas. In addition to it, we used the methods described in section 3.1.2 to determine the position/energy/angle of the sputtered copper atoms from the target. The BEM treatment of the diffusive transport was also incorporated. We also considered the chamber boundary as shown in figure 3.3. To investigate the effect of the distance to the wall, three cases with chamber radii of 7, 10 and 13 cm were tried. These correspond to the nearest distance to the wall, actual radius of the chamber, and the furthest distance to the wall in the experimental apparatus, respectively.

Figure 3.7 is the snapshots of the position of copper atoms taken during this simulation. In this figure, argon gas pressure is assumed to be 10 Pa [1], and the gas temperature is 400 K. The outer radius of the boundary is 10 cm (not drawn). 5000 copper atoms are plotted in the figure; red points denote the atoms still flying in the chamber, while the blue ones denote the atoms already deposited on the wall. As you can see in this figure, most of the atoms are still flying even 200 μs has elapsed. At this time, all copper atoms are thermalized and its velocity profile obeys the Maxwellian. It means that the thermal motion of gases is important to simulate the particle transport in high pressure sputtering.

3.3.2 Thickness profile

Figure 3.8 shows the experimental and numerical results of the thickness profile of Cu films, for gas pressures of 2 Pa and 10 Pa. Horizontal axis is the position along the x axis, as described previously. Nearer wall of the chamber is located at the positive side $x = 7$ cm, while the further wall is at $x = -13$ cm. The profile is normalized by the largest thickness, which was not always at $x = 0$. The results on both front and back faces are plotted simultaneously, the much smaller data are those at back face.

The marks in the figure are the experimental results, while the lines are simulation results. Since our program code can only account for the axisymmetric cases, we performed the simulation for two cases, with chamber radius of 7 cm and 13 cm, which were the nearest and the furthest distances between the target center and the chamber wall, respectively. The result of 13 cm is plotted in a solid line in the region of $x < 0$, while that of 7 cm is plotted in a broken line in $x > 0$.

It is observed on the front face that the film thickness takes the maximum at above the target center, and becomes thinner as going away from there. By comparing the both halves, nearer and further from the chamber wall, the decrease of the thickness is steeper on the nearer side ($x > 0$). It can be explained by considering the diffusion process. If the sticking coefficient of the particle is unity on the chamber wall, it can be regarded as the boundary with zero particle density, as discussed in 2.6.1. Hence, nearer the chamber wall, smaller the density of particles. It

[1] Again, this is the vacuum gauge value and indicates the gas density (see eq. 3.1).

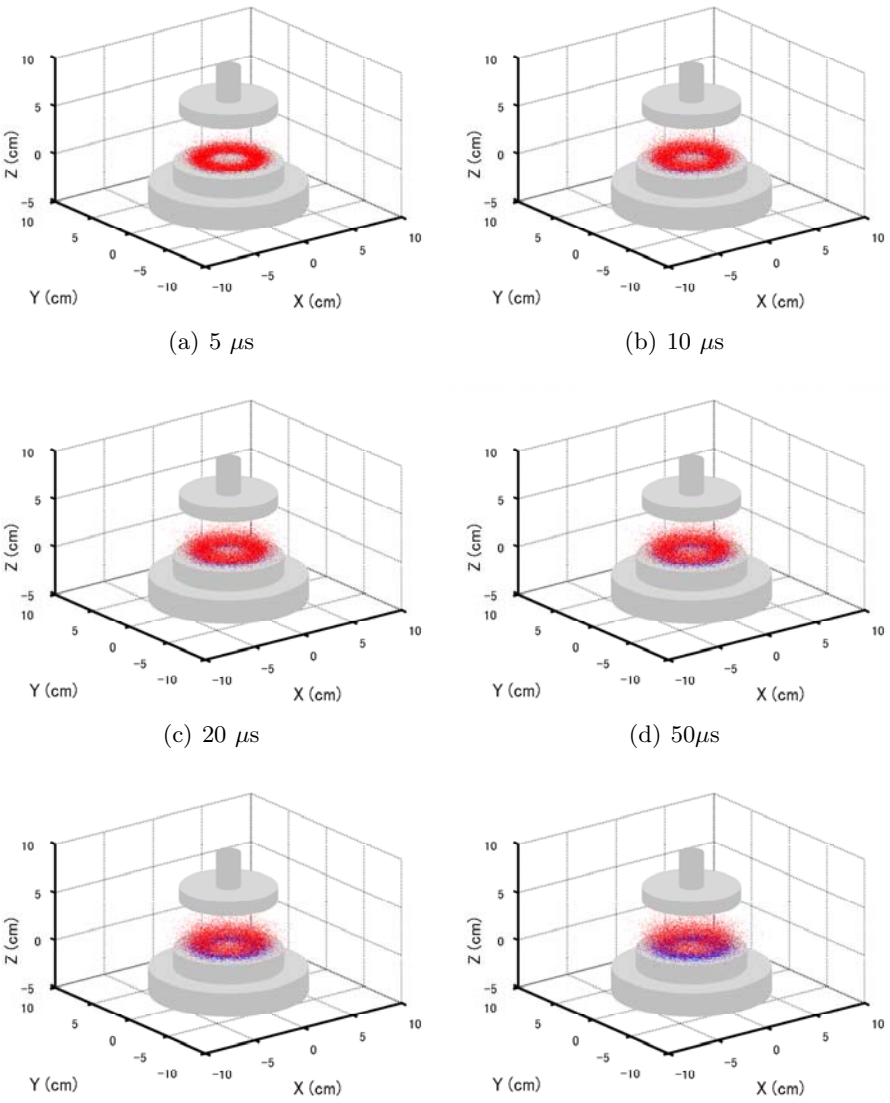

(a) 5 μs (b) 10 μs

(c) 20 μs (d) 50μs

(e) 100 μs (f) 200μs

Figure 3.7: Time evolution of the real space distribution of 5000 Cu atoms: Actual deposition condition is assumed where the argon gas pressure is 10 Pa and primary ion energy is 300 eV.

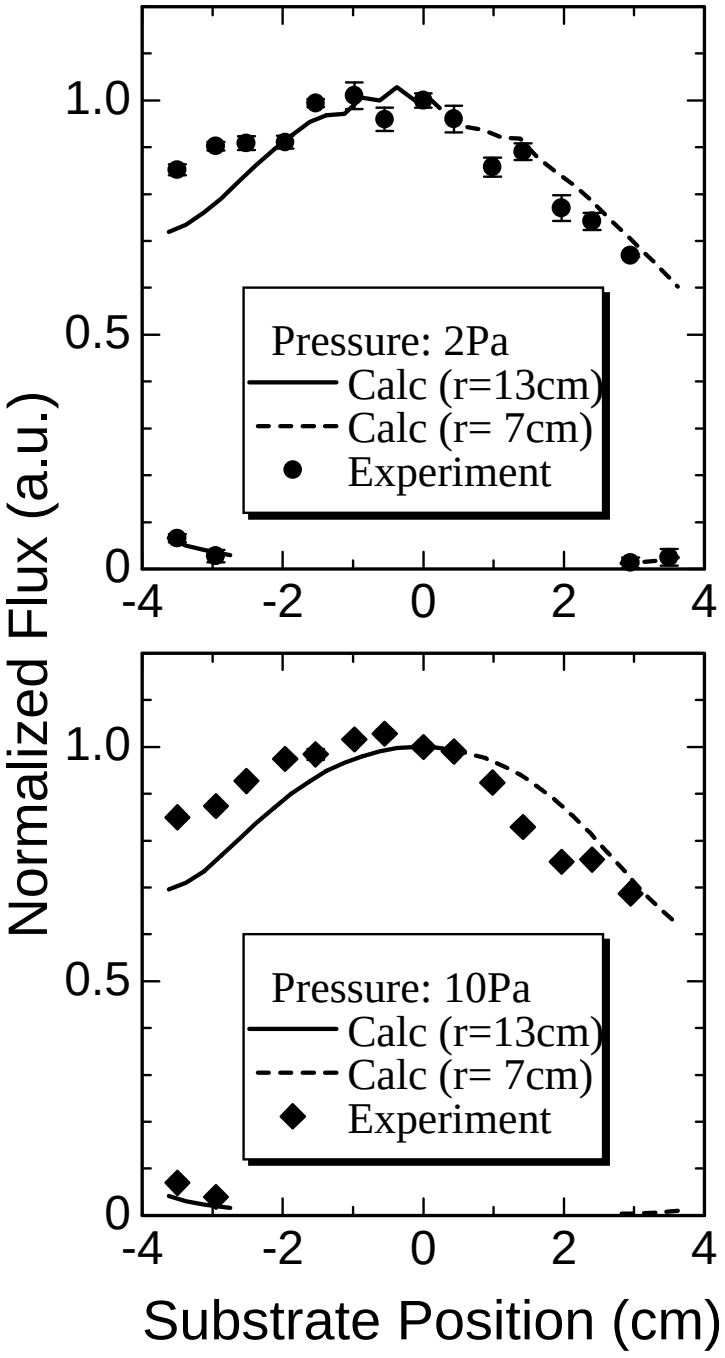

Figure 3.8: Thickness profile of sputter-deposited Cu films.

is reproduced by the simulation also. You can see that the dotted lines show the rapid decrease as they come far from the center on both 2 Pa and 10 Pa cases.

While the agreement between the experiment and the simulation was fairly wall on the nearer side ($x > 0$), it was rather poor on the further side ($x < 0$). The experimental result shows more moderate decrease there. It may be originated from the density gradient reflecting the surrounding wall configuration or the flow field of the argon gas, but we have no clear explanation for this yet anyway. If full-3D simulation would become possible in the future, it should be worth to evaluate this gradient with it.

3.3.3 Diversion of sputtered atoms onto the back face

As mentioned in the first part of this section, sputtered atoms are deflected by the collision with gases, hence they may arrive at the chamber wall which cannot be seen directly from the target. Now let us consider the thickness profile on the back face of the substrate holder, as schematically shown in figure 3.9. On the contrary to the front face, the profile on the back face becomes thinner as entering inside from the edge of the substrate holder.

In the low pressure limit, where no collision occurs, atoms cannot arrive at the back face. So you may think that the higher the pressure, the thicker the backface film is. But it is not true. On extremely high pressure, the relative thickness on the back face becomes thinner. Actually, the result of nearer half ($x > 0$) at 10 Pa lacks the experimental data on the back face, because they were too thin to be measured with the interferometer. In the following, we define the BFR (back-front ratio) as the thickness ratio of back/front faces at same x. We obtain the BFR on further wall side ($x < 0$) experimentally, and compare its pressure dependence with the simulation.

The pressure dependence of the BFR is shown in figure 3.9. In this figure, the experimental and simulation data are plotted with filled and open marks, respectively. It was taken on the further half ($x < 0$), 30 mm and on 35 mm from the center of the substrate holder (holder radius is 40 mm). The position $x = -35$ mm is nearer at the holder edge, hence the ratio is larger than at $x = -30$ mm. Experimental scatter was rather large because of the thin film thickness at back face, but the agreement of experiment and simulation on both location is satisfactory. And it also should be noted that the tendency of BFR in this figure agrees well with the results reported by Motohiro [90].

This BFR behavior can be explained considering the transition of the particle transport, from the ballistic one to the diffusive one. As mentioned above, at the low pressure limit, sputtered atoms cannot deposit on the back face. As the pressure increases, the particles come to be able to arrive there by the scattering, and the arrival rate increases gradually. At higher pressures, the sputtered atoms tend to be thermalized before they deposit on the wall. They are thrown away some distance from the target through ballistic transport, and are thermalized. From there, they start diffusion, which is actually the random walk in the MFP scale. In this region, the thermalization profile approaches nearer to the target as the gas pressure increases. It means that the diffusion source of the particles come closer to the substrate holder [2]. It results in the decrease of the atomic flux at the back face, since the distance from the source becomes

[2] see also section 2.6.

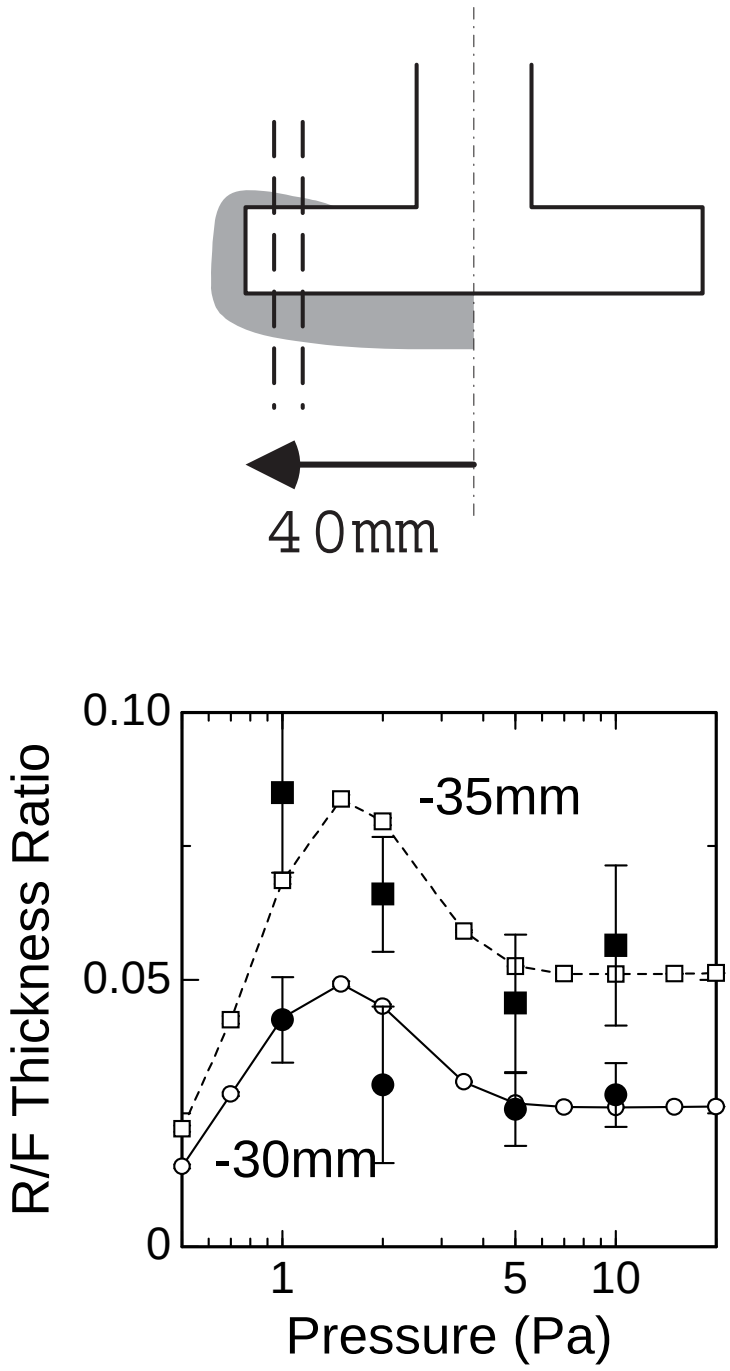

Figure 3.9: Ratio of deposition rates at front/back face of the substrate holder. Filled and open marks denote the experimental and simulation results,respectively.

relatively larger. At the high pressure limit, where all atoms are thermalized just after the ejection from the target, erosion track itself can be regarded as the particle source. Therefore, the BFR becomes constant in this region.

In figure 3.10, we show the gas pressure dependence of the thermalization profile obtained by the simulation for 10^6 copper atoms. The density of the thermalization atom is displayed by the color map in linear scale of arbitrary unit. Thermalization threshold was set to $0.1kT_g$, as described in section 3.1.2. Sputtered atoms may start the random diffusion at more higher energy, but fig. 3.10 should still give the information we need. As can be seen from the figure, the thermalization comes to significant at around 1.5–2 Pa, where the BFR takes the maximum in the simulation. Above this pressure, it is clearly shown that the thermalization profile approaches toward the target. Thus the BFR decreases in high pressures, and becomes constant.

3.3.4 Summary

In this section, we have simulated the sputter deposition process of copper films. The thickness profile on the substrate holder was changed by the distance from the chamber wall. When the wall was near, the profiles was thinner. It is also confirmed by the simulation, and can be explained by considering the chamber wall as the zero density boundary.

We then defined the BFR ratio (thickness ratio on back and front faces of the substrate holder), and investigated its pressure dependence. The simulation reproduces its behavior; BFR increases with increasing the gas pressure in low pressure region, and then decreases and approaches to constant. It also coincides with the experimental result reported by Motohiro.

The pressure dependence of the BFR can be explained as follows. In lower pressures, where the ballistic transport is dominant, the increase of the gas pressure causes more collisions and raise the BFR. On the other hand, at high pressures where the diffusive transport occurs, thermalization profile concentrate into the neighbors of the erosion track as the pressure increases. Thus the BFR decreases and approaches to the constant value, where the erosion track itself can be regarded as the particle source of the diffusion.

3.4 Composition of LaB_6 sputtered films

In this section, we study the compositional deviation of sputtered LaB_6 films and its gas pressure dependence. As mentioned in section 1.5, sputter deposition technique has been applied widely not only to elemental materials but also to compounds and alloys. In the sputter deposition of these multi component materials, it has been frequently observed that the composition of the film deviates from that of the target, which critically affects the physical properties of the film. In these investigations it has also been pointed out that the extent of the deviation depends on the gas pressure.

The reason for the compositional deviation may be classified into three categories corresponding to the stages of the sputter deposition; (1) processes on the target, (2) particle transport process through the ambient gas, and (3) processes on the substrate. As for the first stage (*i.e.* when the target material is sputtered), there may be the difference in angular- and energy-distributions and/or sputtering yield between composing elements. However, these should not depend strongly on the gas pressure. It has also been pointed out that the sputtering yield

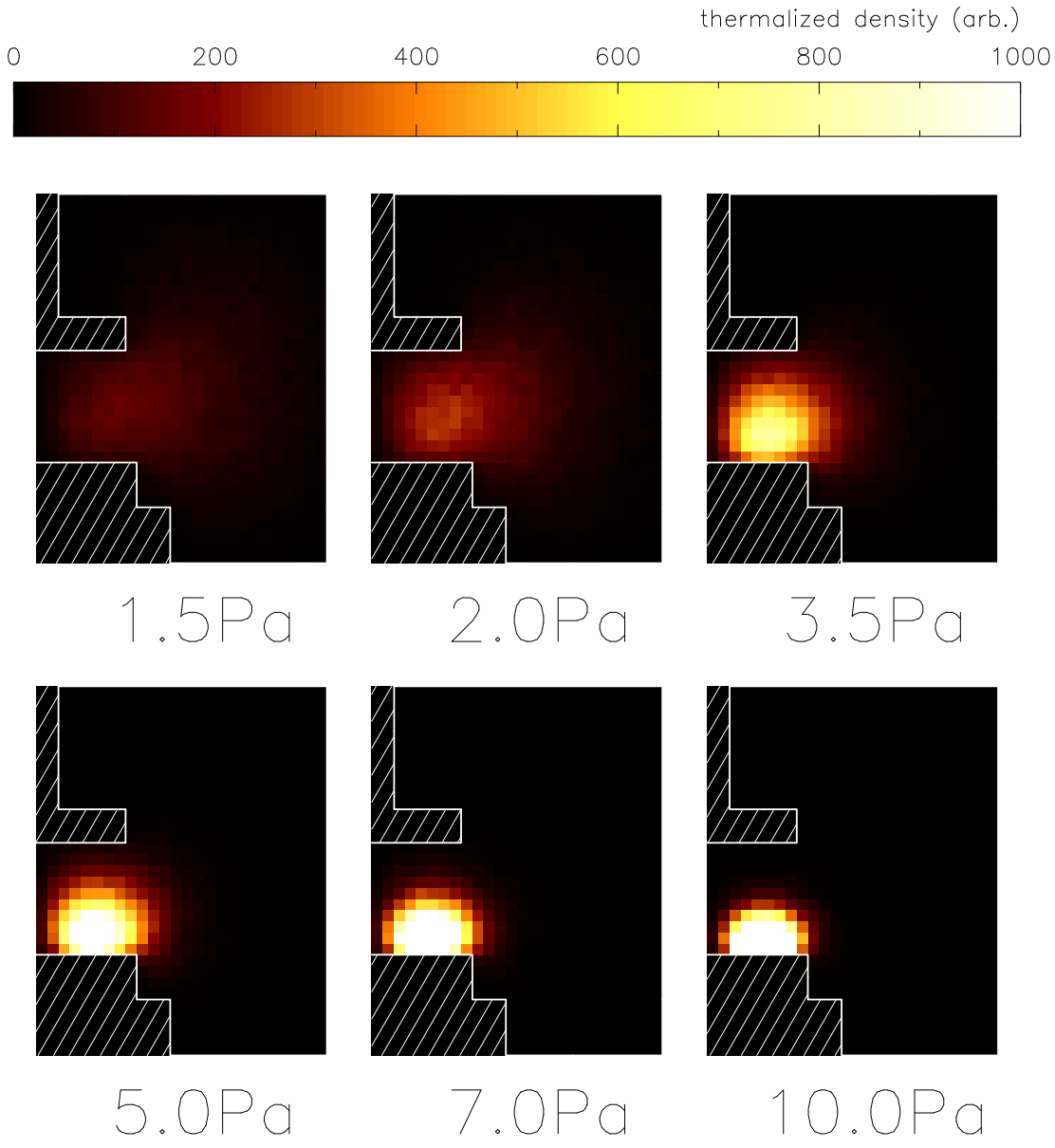

Figure 3.10: Distribution of thermalized positions of sputtered particles.

difference should be compensated by the resultant deviation of surface composition [169]. As for the second, the difference in scattering behavior of sputtered particles has been pointed out [123, 173], which is also the main subject in this section. As for the third, the difference in sticking coefficient or re-sputtering rate may cause the compositional shift. For example, the effects of negatively ionized oxygen molecules have been intensively studied for oxide film deposition [32,127]. But in case of non-reactive sputtering, where the generation of negative ion hardly occurs, this effect can be neglected.

In the present study, we concentrate on the second stage. In a standard sputter-deposition system, inert gas of 0.1–10 Pa is introduced to generate the plasma discharge. In this case, sputtered atoms experience several times of collision by ambient gas atoms. As shown in section 3.2, they gradually lose their energy and change directions with these collisions, and their motion become more diffusive rather than ballistic. Flux of sputtered atoms arrived on substrate should be strongly affected by the number of collision events, which is dependent on the gas pressure.

In this section, we have sputtered LaB_6 and studied the compositional dependence of deposited films on the gas pressure by both experiments and MC simulation. LaB_6 is the material which has preferable features for hot cathode; e.g., high melting point, low vapor pressure, and low work function. Preparation of LaB_6 films by sputtering technique has already been reported by several authors [94,126], in which the compositional shift problem is also pointed out.

To study the compositional deviation problem, LaB_6 happens to be suitable because of the following reasons. Difference in the mass between lanthanum and boron is extremely large, so that the difference in the scattering behavior with argon gas atom is emphasized. In addition, La–B system is in solid phase independent of the composition as high as 2000 K [57]. Therefore the desorption of deposited atoms can be neglected. And finally, it has already been confirmed that only single atoms (no clusters) were observed with mass spectroscopy measurement in sputtering of LaB_6 [59]. Hence we can apply a simple simulation model.

3.4.1 Experiments

Lanthanum boride (LaB_x) films were deposited using the sputtering apparatus described in section 3.1.1. Target was a sintered LaB_6 disk of 99.9 % purity, and the target-substrate distance was set to 7cm. For LaB_6 deposition, RF power source was used. RF power applied to the target was 100 W. Argon was used as a discharge gas, and its pressure during the sputtering was changed from 2 to 15 Pa. For conditioning the target surface, pre-sputtering was carried out for an hour before opening the shutter and starting deposition.

Films of 200–300 nm thickness were deposited on the $22 \times 15\,\mathrm{mm}^2$ of (boron free) Soda-Lime glass substrate. The composition of the films were determined by ICP-Mass (Inductively coupled plasma with mass spectrometer) method where the films were dissolved by nitric acid, and the concentration of La and B in the solutions were measured. By dividing them with the film area and the deposition time, atomic fluxes of two elements were deduced.

Figure 3.11 is the result of the ICP-Mass measurement. A process pressure dependence of the atomic fluxes is shown in (a), and the B/La ratio of the flux is shown in (b). The atomic flux dependence on the gas pressure can be separated into two regimes at around 5 Pa. In low pressure region, atomic flux of both elements gradually decreased with increasing the pressure. Decrease of boron was slightly faster than La, hence the composition of the films gradually

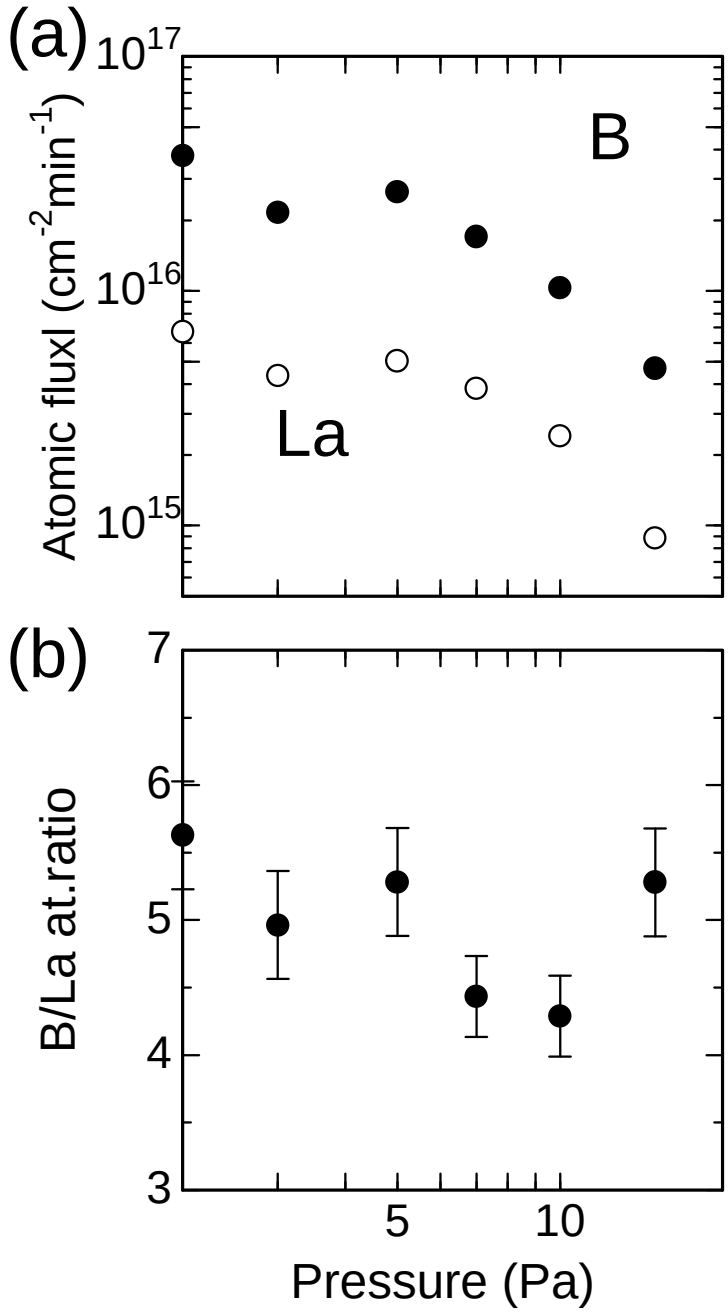

Figure 3.11: Result of ICP-Mass measurements of LaB_6 sputtered films: (a) atomic flux (b) B/La ratio.

shifted to La-rich. In higher pressures, on the other hand, the flux sharply dropped, but the ratio of the two elements recovered to the target composition. Deposition rate of the films was also measured by the multiple interferometry. It was decreased constantly with pressure increase; 7.3 nm/min at 0.5 Pa and 0.5 nm/min at 15 Pa. These values agreed with the one calculated from the flux in fig. 3.11 (a) and atomic density of LaB_6.

At the process pressure less than 3 Pa, deposited films had purple-gray color, as reported previously [94] for stoichiometric LaB_6 film. In these pressures, target also exhibited fresh purple surface as before the sputtering. On the contrary, at higher pressures, the films looked like in metallic gray, and target were covered with griseous-colored overlayer except for the erosion tracks, on which the target surface still looked like that at lower pressures.

3.4.2 Simulation

The Monte Carlo simulation has been carried out as described in section 3.1, except for the following point. In this simulation, we supposed that all sputtered particles had the identical energy when they ejected from the target. It is because, as far as we know, there is no established theory for the energy distribution of the sputtered particles from compounds. We also assumed that the ejection energy was identical for B and La. In the sputtering theory, energy transfer is governed by the value Γ_{sg} defined by:

$$\Gamma_{sg} = \frac{4M_sM_g}{(M_s + M_g)^2} \tag{3.4}$$

where M_s and M_g are mass of colliding two atoms. Here the Γ_{sg} for La with Ar (0.69) and that for B with Ar (0.67) are nearly equal. That's why we assumed the same ejection energy for both B and La. The simulation was carried out with ejection energies of 5 and 10 eV. As described above, all of sputtered particles were assumed to be atoms.

The chamber boundary shown in figure 3.3 was used. The distance between the target and the substrate was set to 7 cm in accordance with the experiment. Reflecting the form of substrate holder used in the experiment, the thickness of the holder and the rod hanging the holder were thinner in this simulation. One million (10^6) atoms were traced for both lanthanum and boron, and the numbers of them arrived at the substrate position were counted. Actually the 10 trials with 10^5 atoms were performed, and the calculation error was evaluated. The resultant B/La ratio was multiplied by 6 and plotted to compare with the experimental results.

Figure 3.12 shows the composition of sputtered LaB_6 films obtained by the simulation. For comparison, experimental result is also shown in (a) again, while (b) is the simulation result. B/La values are plotted for different ejection energies (5 and 10 eV) and on different positions away from the center of the substrate holder (nodes of 0–5 mm, 10–15 mm, and 20–25 mm). Reflecting the large distance between the target and the substrate, significant dependence on the substrate position is not observed. Simulation does reproduce the dependence of film composition on gas pressure; B/La is stoichiometric at low pressure, decreases with increase in gas pressure, passes a minimum, and recovers to 6 again in high pressure region. The minimum of the B/La is about 4 both in experiment and in simulation. However, the pressures at which the B/La becomes minimum are different. In experiment, it appears at around 10 Pa,

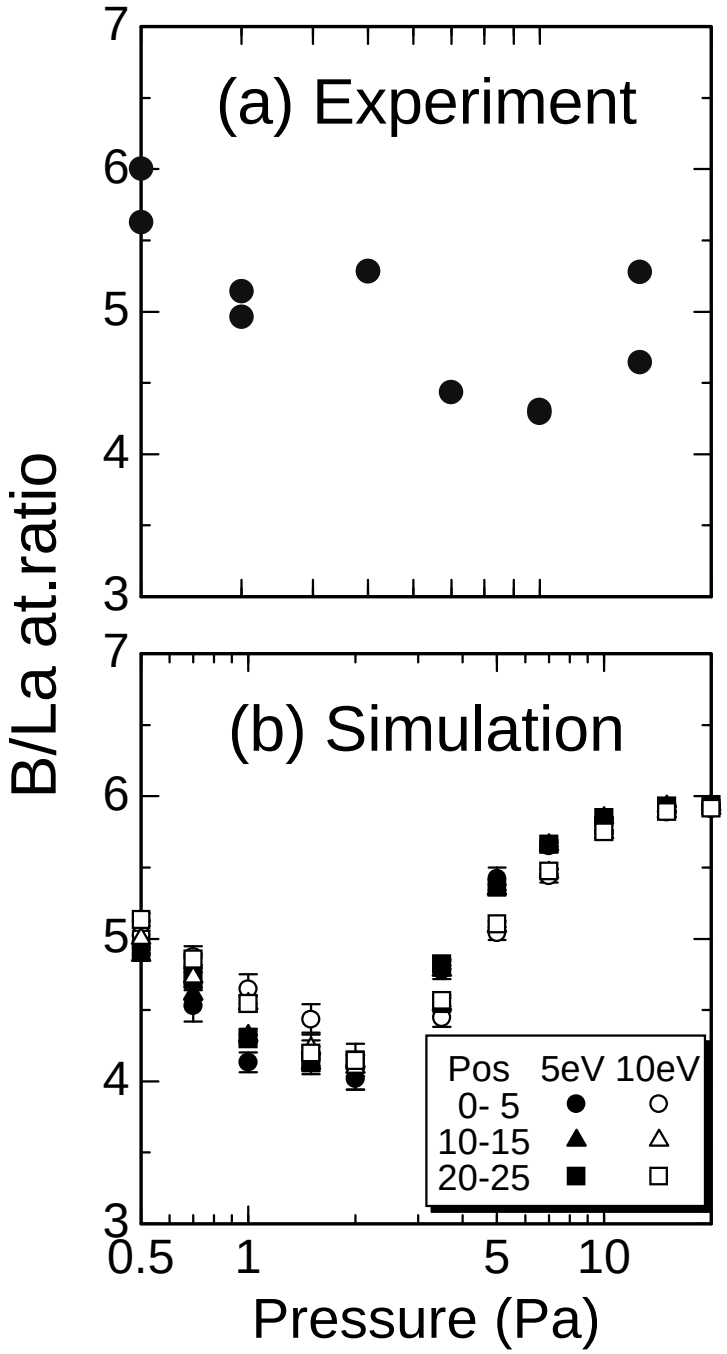

Figure 3.12: Composition of sputtered LaB_6 films: (a) experimental result, (b) simulation result for ejection energies of 5 and 10 eV's. For (b), composition at different radii are plotted (see text).

while it does at 2–3 Pa in the simulation, and slightly shifts to the higher pressure with high ejection energy (10 eV).

3.4.3 Mass difference effect on energetic particle transport

In this subsection, we discuss the origin of the "U-shaped" dependence of B/La ratio on gas pressure, in view of the particle transport process of B and La atoms.

Neglecting the motion of argon gas atom, boron atom may be scattered backward by ambient argon atoms, while no backscatter occurs for lanthanum. This is shown in figure 3.13, which is the scattering angle of B and La atoms in laboratory system calculated using the formulation in section 2.3.2. This applies for atoms in the initial ballistic transport stage, since sputtered atoms from the target initially have energy as high as several electron volts, hence much faster than Ar atoms.

The difference can be understood as follows: When the sputtered atom collide with the gas atom, its velocity after the collision is given by the eq. 2.45:

$$\boldsymbol{v}_s{}' = \frac{m_s \boldsymbol{v}_s + m_g \boldsymbol{v}_R{}'}{m_s + m_g} \tag{2.45$'$}$$

where m_s and m_g are the mass of sputtered atom and gas atom, respectively, and $'$ denotes the values after the scattering. If the sputtered atom is much faster than the gas atom, the absolute value of relative velocity $\boldsymbol{v}_R$ $(= \boldsymbol{v}_g - \boldsymbol{v}_s)$ is almost identical with $\boldsymbol{v}_s$. Furthermore, in the elastic scattering, the absolute value of $\boldsymbol{v}_R$ does not change, but only the direction changes. Hence, the absolute values of $\boldsymbol{v}_s$ and $\boldsymbol{v}_R{}'$ in eq. 2.45 are equal. If the sputtered atom is heavier than gas atom $(m_s > m_g)$, initial velocity $\boldsymbol{v}_s$ affects $\boldsymbol{v}_s{}'$ more strongly than $\boldsymbol{v}_R{}'$, and vise versa.

In the center of mass system, the angle between $\boldsymbol{v}_R$ and $\boldsymbol{v}_R{}'$ is 2π (*i.e.* opposite direction) when the collision parameter b is zero. And as b becomes larger, the angle decreases toward zero at $b = \infty$ (see figure 2.1). Therefore, for the lighter atom, backscattering can occur in the laboratory system at small b. For the heavier atom, on the other hand, it does not occur and only forward scattering is allowed.

As carried out in section 3.2, time evolution of the velocity distribution of B and La atoms are displayed in figure 3.14. (a), (c) and (e) are for boron, while (b), (d) and (f) are for lanthanum. The atoms are injected into the argon environment at 0 s along the positive direction of z axis, with the initial kinetic energy of 5 eV. The temperature of argon gas is assumed to be 400 K, and the effect of thermal motion of gas atoms is taking into account. The gas pressure is set to 3 Pa, where the B/La ratio shows the minimum in the simulation (see 3.12). Snapshots are taken at 10, 20 and 50 μs, which is slightly later as compared to fig. 3.4, reflecting the lower pressure of the gas (and larger MFP). Since their masses are quite different, the scale of the velocity axes also differs for B ($-10000 \sim 10000$ m/s) and for La ($-3000 \sim 3000$ m/s).

The difference between the elements reflects the difference in scattering angle with argon gases shown in fig. 3.13. In boron case, their direction is quickly scattered and the velocity profile looks centrosymmetric already at 10 μs. After that, the profile converges into the Maxwellian keeping the symmetry. On the other hand, in La case, the profile preserves the initial momentum to the z direction, and seems to "drift" into the Maxwellian as a whole. The energy distribution of boron atoms converges to Maxwellian earlier than that of lanthanum, because the speed of

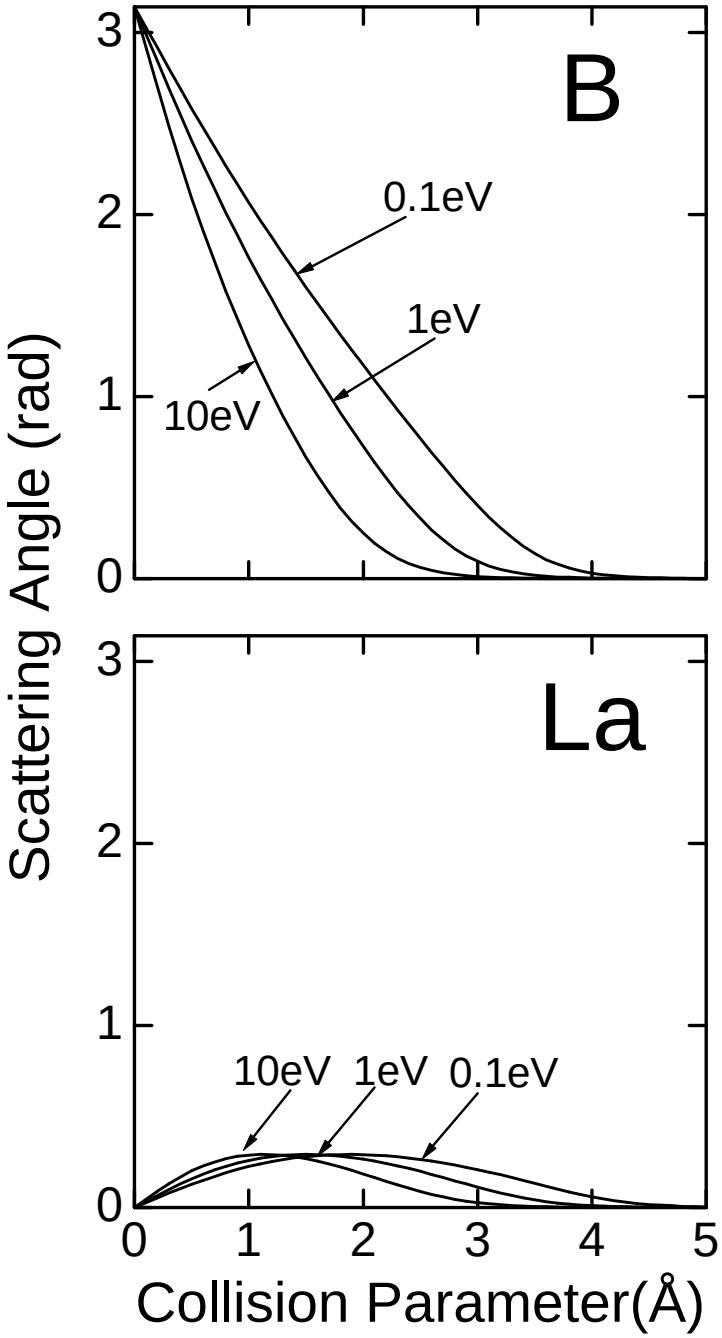

Figure 3.13: Scattering angle of B and La atoms when they collide with an stational Ar atom.

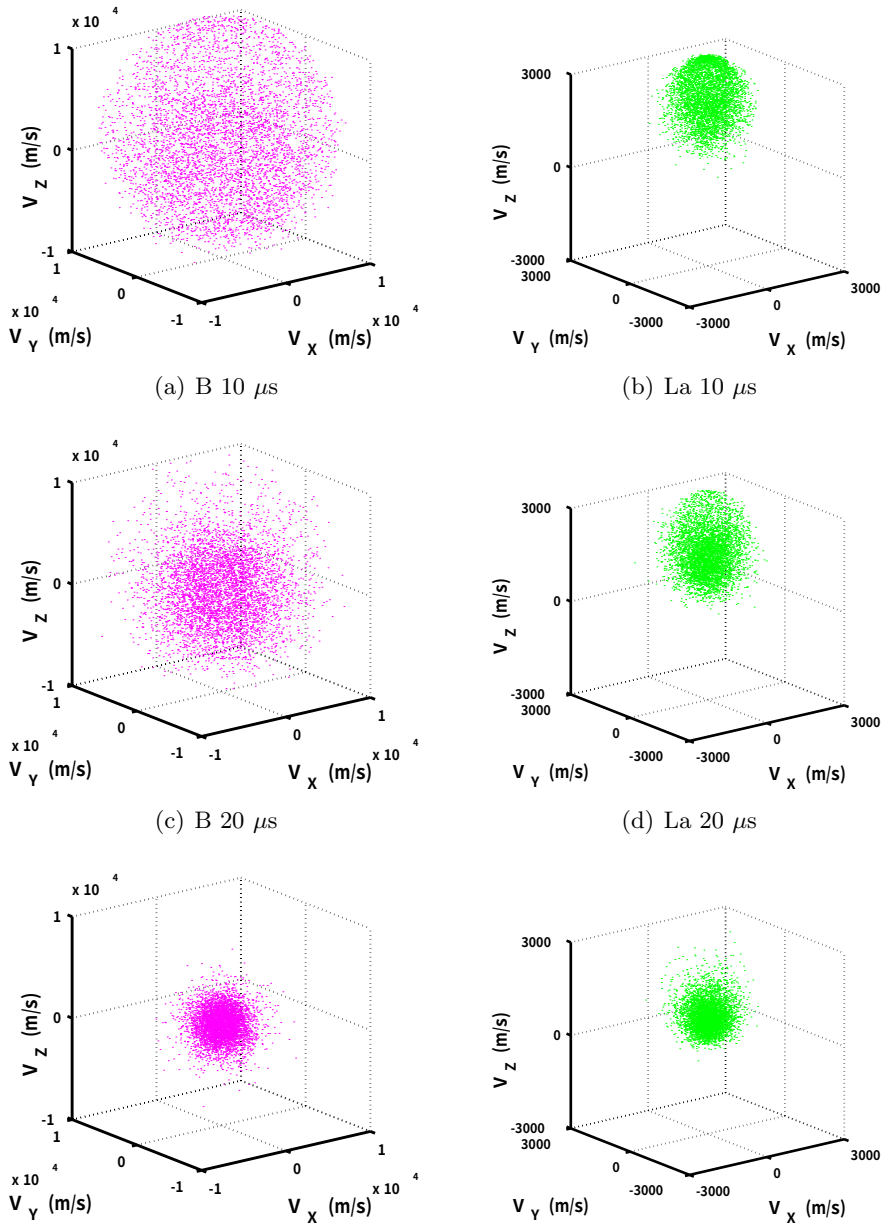

(a) B 10 μs

(b) La 10 μs

(c) B 20 μs

(d) La 20 μs

(e) B 50 μs

(f) La 50 μs

Figure 3.14: Evolution of the velocity distribution of B and La atoms in an Ar environment with 3 Pa and 400 K. At 0 second, particles are injected along the z axis to the positive side, with a kinetic energy of 5 eV. (a), (c) and (e) are for boron and (b), (d) and (f) are for lanthanum. In these graphs, 5000 particles are displayed.

boron atoms is faster than that of lanthanum atoms when their kinetic energies are identical. Boron atoms experience more collision than lanthanum in a same interval, and are decelerated more.

Next we show the transport of these atoms in the real space. Figure 3.15 shows how these high energy particles spread in the gas environment. Conditions are the same with figure 3.14. B or La atoms are injected at 0 second from the origin toward the (0,0,1) direction with the energy of 5 eV. The pressure and the temperature of Ar gas are 3 Pa and 400 K, respectively.

Two clear differences are observed between boron and lanthanum in their transport properties; one is whether the centroid of the distribution shifts from the origin or not, and the other is the rate of dispersion. The propagation of lanthanum atoms is strongly biased to the region $z > 0$ while the area where they spread is rather limited. On the other hand, the boron atoms propagate into not only $z > 0$ but also $z < 0$, and are dispersed promptly in the argon atmosphere.

These behaviors in real space reflect the time evolution of the velocity distribution shown in fig. 3.14. Boron atoms are scattered in its direction before they are decelerated, hence they spread in real space homogeneously. On the other hand, lanthanum keeps the initial momentum along the z axis, they seem to be impinged into the $z > 0$ initially, and diffuse from there. Since we fix the initial energy in both cases, the lighter boron is dispersed more quickly. It also should be noted that the mean free path becomes larger for faster particles as shown in section 2.5.1, which may also affect the faster dispersion of boron.

3.4.4 Discussion and summary

Now we consider the reason for the compositional deviation of LaB_6 sputtered films based on the discussion in the previous subsection.

In low pressures, where the ballistic transport is dominant, the boron content decreases gradually with increasing the gas pressure. This is originated from the difference in the scattering behavior with argon gas atom; boron may be backscattered, while lanthanum is not. As the pressure increases and more collisions occur in this region, arrival probability of boron onto the substrate decreases more rapidly, because they tend to be deflected more by the collision than lanthanum.

On the other hand, at higher pressures, B/La ratio recovers to six (the stoichiometric value) as the gas pressure increases. It is explained by considering the thermalization of sputtered atoms. As described in section 3.3, sputtered atoms are more likely to be decelerated as the gas pressure increases. When their energy decreases down to the thermal energy of the ambient gas (thermalized), their transport is no more ballistic but diffusive. If, in this stage, the thermalization point (*i.e.*, source of the diffusion) is same, the arrival probability at the substrate is also same independent of the diffusion coefficient (see section 2.6.2). In other words, the mass difference does not affect the transport anymore in the diffusive transport. However, the thermalization profile of lanthanum atoms distributes further from the target (nearer from the substrate) than boron, La flux is still larger than B. But at high pressure limit, where the thermalization of both elements occur just above the erosion track, there is no difference between the thermalization profiles of La and B, hence the ratio of atomic fluxes on the target recovers to stoichiometry.

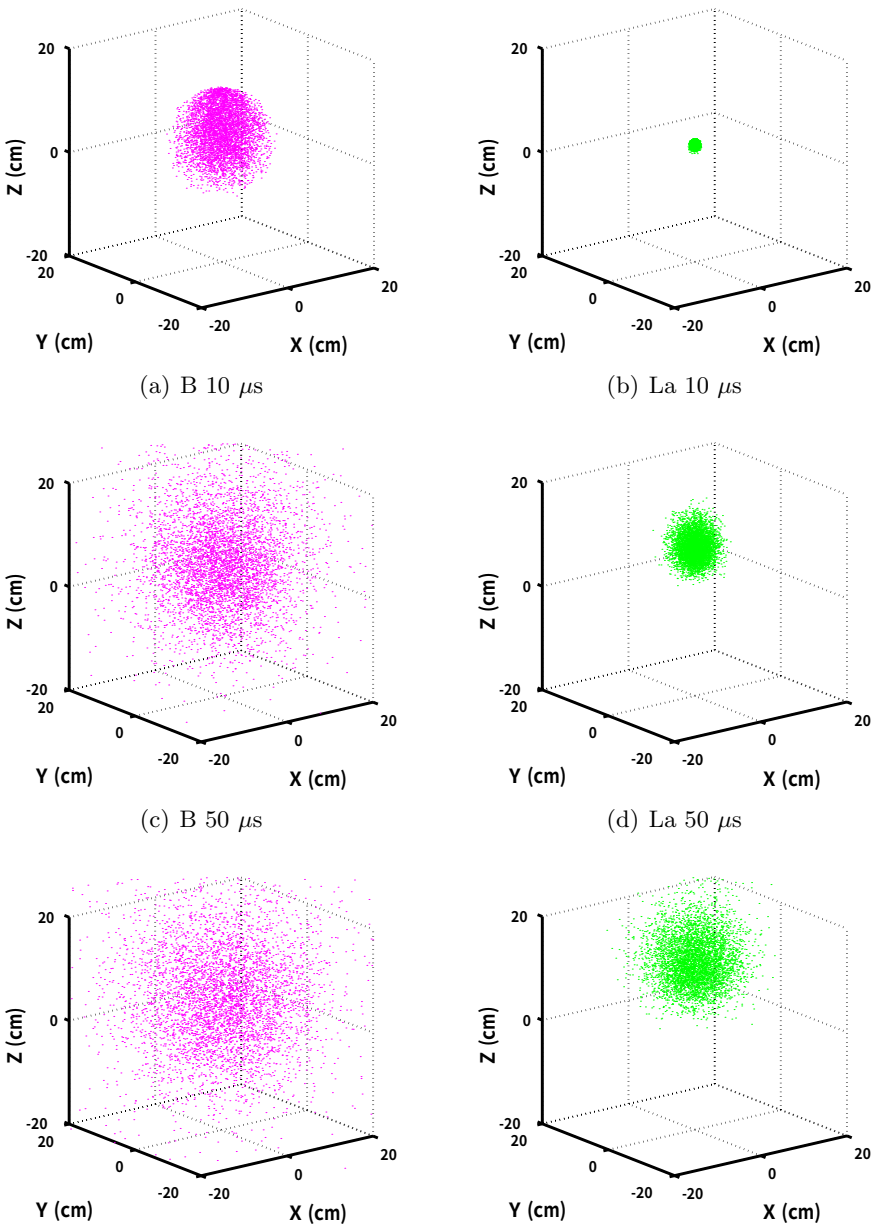

(a) B 10 μs (b) La 10 μs

(c) B 50 μs (d) La 50 μs

(e) B 200 μs (f) La 200 μs

Figure 3.15: Propagation of the B and La high energy atoms in Ar gas. Conditions are the same with figure 3.14. (a), (c) and (e) are for boron, and (b), (d) and (f) are for lanthanum. Also 5000 particles are displayed.

The gas pressure where the B/La ratio shows the minimum was inconsistent between experiment and simulation. This pressure corresponds to the transition of the transport from ballistic to diffusive. Thus in the simulation, the deceleration of atoms should be overestimated. As listed in section 3.1, the gas pressure is assumed to be uniform in the simulation. But at high pressure and high discharge power, it has been proposed that the gas density becomes smaller near the target (see section 1.1.4). Assuming this effect, the gas density near the target is lower than the gauge value in the experiment, which raises the minimum pressure. In the simulation, the minimum pressure became higher when ejection energy was set to higher value (10 eV). It is because more collision is required before the thermalization. Summarizing, the ejection energy of sputtered atoms and the gas pressure may reflect the gas pressure at the B/La minimum. In the simulation in this section, we simply assumed the identical (and constant) ejection energy for both B and La. If more proper model for this ejection energy would be developed in the future, more quantitative discussion should be possible.

In actual sputter deposition, backscattered boron atoms will deposit onto the target. When they do on the erosion track, they are re-ejected again by the following (re)sputtering. But if they deposit on the non-erosion track part of the target, they will be accumulated there unless the sputtering rate is faster than the deposition rate. As predicted by figure 3.14, boron is more likely to go back to the target surface, hence boron content may be higher there. The experimentally observed target color degradation at high pressures also suggests this backscattering and deposition of sputtered particles, mainly boron maybe.

In summary, we have shown the strong dependence of B/La atomic ratio on process pressure in sputter deposition process of LaB_6 films from both experiments and Monte Carlo simulation study. The film composition is almost stoichiometry in both low and high pressure limits, but shows a minimum as low as B/La=4 in the midst pressure. The depletion in boron in lower pressure was explained by the difference in scattering angle distribution between B and La in ballistic transport stage. Since boron is more likely to be scattered backward by the collision with argon gas atom, the arrival of it on the substrate decreases more than lanthanum as the gas pressure increases. Recovery of B/La ratio at higher pressures stems from the thermalization and following diffusive transport of sputtered atoms. When the pressure is not high enough, lanthanum tends to thermalize further from the target (*i.e.*, nearer from the substrate), so arrival flux of it is larger. On the contrary, at high pressure limit, the thermalization profile of both B and La atoms approaches to the target neighbor. Therefore, the flux ratio of both elements at the substrate is identical to the target composition.

3.5 Density of sputtered atoms in the plasma

In this section, we describe a novel method to evaluate the spatial density of sputtered particles using Monte Carlo simulation.

While the effect of energetic particles on deposited films has intensively been studied by many researchers, the spatial density of them has rarely been investigated. It is probably due to the unimportance of it to the processes of conventional sputtering (in contradiction to CVD). However, it has recently attracted attentions because of the recent development of ionized sputtering [117], as well as the fundamental interests to the magnetron plasma. Some

experiments using optical absorption [9, 25], and its variants [78] have been reported, but the theoretical studies are rather scarce. One of such efforts includes the versatile model of IPVD process by the group at Univ. of Illinois [39]. They elucidated the particle density combining the MC approach and diffusive approach. In their case, it is necessary to assume the diffusion coefficient of Cu in Ar gas environment.

From purely particle-oriented viewpoints, it is possible to deduce the density of sputtered particles from the residual time of each particles and the ejection frequency of them from the target. For example, if 10 particles are ejected from the target per one second, and if each particle stays for 10 seconds in the chamber, 100 particles should be found there on the average. Similarly, if you split the chamber volume into cells and evaluate the residual time in each of them, you can obtain the atomic density profile. Also note that the ejection flux of the sputtered atoms from the target should be proportional to the incident flux on other chamber boundaries, including substrates. Therefore, if this proportional constant is known, you can calculate the density from the residual time and the deposition rate.

The residual time of sputtered particles can be calculated by the Monte Carlo simulation method. To do this, the MC method must be extended so that it can treat properly the motion of particles after they are "thermalized", where their energy become comparable to the thermal energy of gases. In other words, the colliding gas motion must be incorporated into the MC framework, or the sputtered atom is monotonically decelerated and stops its motion after some collisions (as discussed in section 3.2). Our model described in 2.5 is well suited for this purpose; the motion of sputtered atoms in this case approaches the Maxwellian distribution in this case (see figs. 3.4 and 3.5).

The introduction of the effect of thermal gas atoms has partially been done by Turner *et al.* in 1989 [153] (see section 1.6.2). They applied their method to the gas density calculation, and showed that the gas density increased with increase in gas pressure. However, the absolute values of them were not shown since the ejection frequency is not taken into account.

This method is applied to the DC magnetron plasma of Cu/Ar. The calculation result is compared with the previous reports as well as with our OES measurement of this magnetron plasma. For the latter, the "self absorption" effect of a certain line from the Cu neutral is discussed. This effect is caused by the reabsorption of the emitted photon by another copper neutrals, and reflects the spatial density of them in the plasma environment.

3.5.1 Density calculation

To calculate the residual time of sputtered particles in the chamber, MC simulation described in 3.1.2 is used, except for the BEM treatment of diffusion process. The motion of each atom is throughly followed until it reached the chamber wall. The gas temperature is assumed to be 400 K, and gas density is assumed to be uniform in the chamber.

Chamber boundary used in this MC simulation is shown in figure 3.16. It is basically the same with the one used in section 3.3. The radius of the chamber is set to 10 cm. In addition, the region between the target and the substrate holder was also split into meshes at intervals of 5 mm, in each of which the atomic density was calculated.

At first, the residual time of sputtered particles are calculated. Since the speed of the particle between two collision events is constant, the time can be deduced by the segment length of the

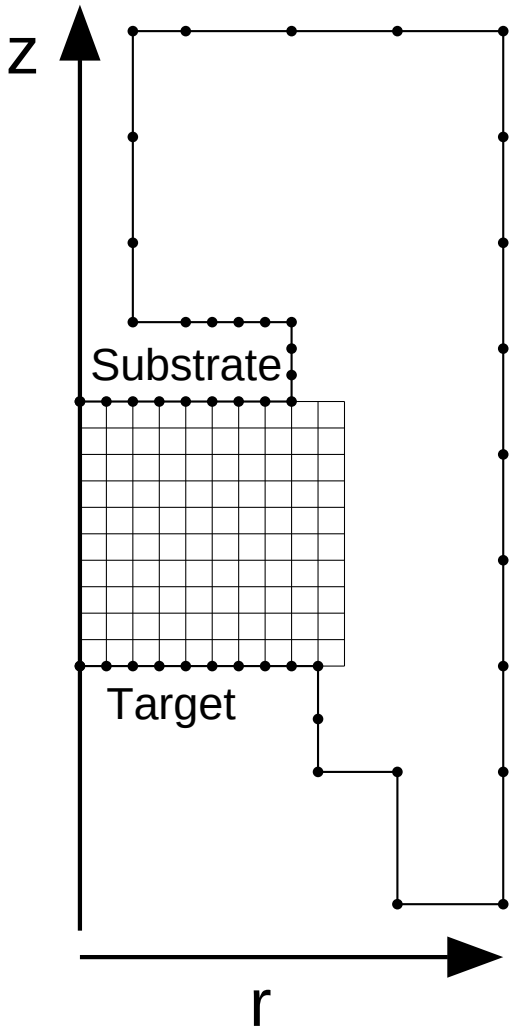

Figure 3.16: Chamber model used in the MC simulation for atomic density evaluation: upward arrow at the left is the symmetric axis. Chamber boundary is split into nodes, whose ends are shown as black dots. The region between the target and the substrate holder is also split into meshes at intervals of 5 mm for both r and z axes.

particle path, cut by the cell boundary. The time in each meshed cell was summed up for all the particles. Now let us pick one of these cells up, and denote the residual time of it as T_C. If we can elucidate the time T_{MC} corresponding to the ejection of whole particles in the MC simulation, the atomic density n_C at the cell is given by:

$$n_C = \frac{T_C}{T_{MC} V_C} \tag{3.5}$$

where V_C is the volume of the cell.

With the same simulation, in which T_C is calculated, numbers of arrival particles are recorded on each boundary nodes. They are divided by the area of these nodes, and the areal density of arrival particles ρ_{MC} are obtained. By comparing ρ_{MC} with the experimentally obtained atomic flux there, the T_{MC} can be derived. If the atomic flux per unit time and unit area is measured to be F_{EXP}, T_{MC} is given by:

$$T_{MC} = \rho_{MC}/F_{EXP}. \tag{3.6}$$

Substituting this relation into eq. 3.5, n_C can be obtained.

The simulation was performed for $10^4 \sim 10^5$ particles, and was repeated several times with different seeds of pseudo random number sequence to evaluate the scatter of the simulation result. It was found that typical value of the error in the residual time was less than 1%, and the error in the deposition flux at the substrate was 6% at most.

The experiment to measure the deposition rate was identical with the one described in section 3.3. Target was 8 cmϕ disk of 4N Cu. Substrate holder was positioned 5 cm above the target. Argon was used as a discharge gas, and its flow rate was kept constant at 10 sccm. Pressure was changed between $2 \sim 10$ Pa by throttling the evacuation valve. DC power was applied to the Cu target cathode to generate a glow discharge. DC power was fixed 100 W throughout the experiment. Film thickness on the substrate holder was measured by multiple interferometry, and deposition rate was obtained by dividing it by the deposition time.

Deposition rate is converted into the atomic flux as follows. Atomic density of copper bulk is given using copper bulk density $\rho = 8.93\,\mathrm{g/cm^3}$, copper atomic weight $U = 63.546$, and the atomic mass unit $\mu = 1.66054 \times 10^{-27}\mathrm{kg}$:

$$\begin{aligned} n_{\mathrm{Cu}} &= \rho/(U\mu) \\ &= 8.93\,(\mathrm{g/cm^3})/\left(63.546 \times 1.66054 \times 10^{-24}\,(\mathrm{g})\right) \\ &= 8.46 \times 10^{22}\,(\mathrm{atoms/cm^3}). \end{aligned}$$

With this, deposition rate given in nm/s becomes:

$$\begin{aligned} 1(\mathrm{nm/s}) &= 10^{-7}\,(\mathrm{cm/s}) \times 8.46 \times 10^{22}\,(\mathrm{atoms/cm^2 s}) \\ &= 8.46 \times 10^{15}(\mathrm{atoms/cm^2 s}) \end{aligned} \tag{3.7}$$

Figure 3.5.1 shows the pressure dependence of the deposition rate obtained by the experiment. Plotted data were measured at the center of the substrate holder. Deposition rate was almost constant until 10 Pa, and decreased at 20 Pa. It was as large as 0.1 nm/s, which corresponded to about $10^{15}\,\mathrm{atoms/cm^2\,s}$. It should be noted that the atomic flux profile by this simulation has reproduced the thickness profile by experiment fairly well as shown in section 3.3.

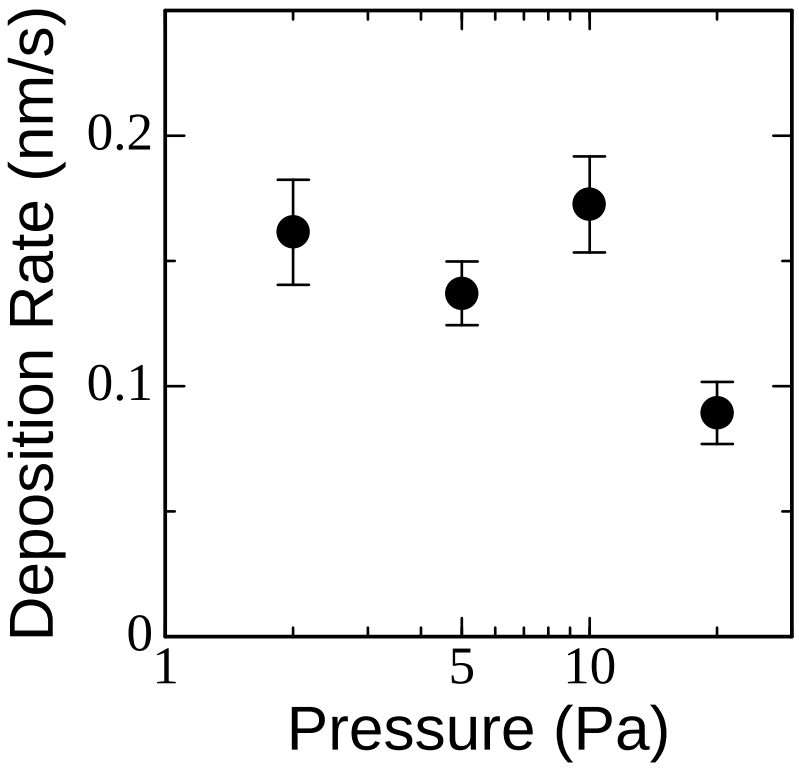

Figure 3.17: Pressure dependence of deposition rate at the center of the substrate holder (experimental result).

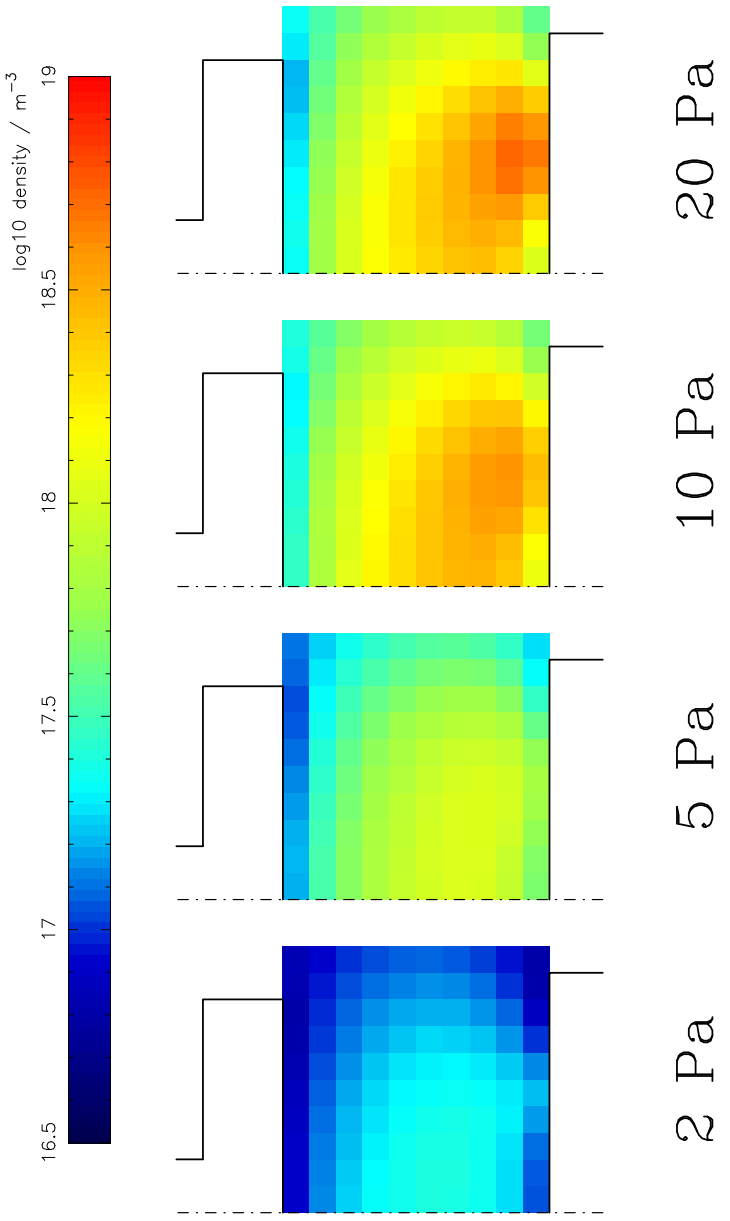

Figure 3.18: Density profile of Cu atoms. Black lines denote the target and the substrate holder. Scale is shown at the top in logarithm.

Using the deposition rate in fig. 3.5.1 and the residual time / the arrival atom density obtained by the simulation, spatial profile of copper atomic density was obtained at four different gas pressures. The results are shown in figure 3.18. Black lines in the figure represent a part of chamber boundary shown in figure 3.16. The Dot-dash line at the left of each profile is the symmetrical axis. Ejection of sputtered particles occurs, as shown in fig. 3.2, at around 2 cm away from the axis on the target surface, which is placed at the bottom of the profile. The color scale of the density is located at the top, with which the logarithm of atomic density is mapped to the color between $10^{16.5} \sim 10^{19}$ m^{-3}.

It is observed that the atomic density increases as the pressure of the discharge gas increases. At higher pressures, mean free path of the sputtered particle becomes shorter. Moreover, sputtered particles are quickly decelerated by collisions with gases and thermalized at high pressures, which also contributes to reduce the mean free path (see section 2.5.1). It reduces the diffusion coefficient of sputtered atoms [3], which result in the higher density. At each pressure, the atomic density is largest at the region nearest to the erosion track, which is the source of particles. On the other hand, the density decreases steeply as the chamber boundary approaches. We have assumed in the simulation that the particle arrived at the boundary adsorbs there with the sticking coefficient of unity. In the diffusion transport model, it corresponds to the boundary condition of zero density. The rapid reduction of the density near the wall at higher pressures means that most atoms are in the diffusive stage, rather than in a ballistic one. If, as an extreme case, particles do not experience any collision until they reach the wall, the atomic density profile stem just from a spread of particle flux as they come away from the target, and should not show the rapid decrease near the chamber wall.

The atomic density of $10^{17} \sim 10^{18}$m^{-3} agrees in order with the experimental results by Dony *et al.* [25]. They sputtered aluminum by argon in an RF magnetron sputtering apparatus. At argon pressure of 10.6 Pa, they have yielded 2.2×10^{17}m^{-3} with the RF power of 20 W, and 4.8×10^{17}m^{-3} with 30 W. Our result seems slightly larger than theirs, even considering the difference in discharge power. It may be due to the larger sputtering yield of Cu than Al (see reference [73] for example), or the gas rarefaction effect [115,152] we neglected in the simulation, which reduces the gas density near the target and hence reduces the atomic density of sputtered particles.

3.5.2 Optical emission measurements

Optical emission (OE) from the plasma discharge reflects many important characteristics of it, such as the density of neutral/ion species, electron density and its energy distribution [82]. Therefore, Optical Emission Spectroscopy (OES) measurement has been recognized as a suitable method for plasma diagnostics.

There have also been many reports applying OES to the magnetron sputtering plasma. For example, dependence of emission intensities on discharge power [82] or gas pressure [26, 27] have been studied, and the excitation process of neutral / ion species were discussed. OES has also been applied to the observation of magnetron plasma, where the profile of the power injection is hardly predicted because of the spatially inhomogeneous magnetic field [84, 132]. As for a

[3] see chapter XIII of reference [56].

rather special case, self-sustained mode in magnetron sputtering where discharge is maintained without argon supply has been observed by OES [110]. Since the enhancement of ionization of depositing materials has recently attracted attention in the field of plasma processing for microelectronics [117], OES will be used more in the future.

In this study, we have developed an OE acquisition system based on a commercially available reflex camera, and performed the OE measurement with spatial resolution. A single plano-convex lens made of synthesized quartz with a focal length of 55 mm is used for imaging. The lens can focus from 20 cm to infinity with this system. An iris is placed before the lens, whose diameter was fixed at 30 mm in this experiment. At the film plate of the camera, a receptacle of an optical fiber is mounted, and a quartz optical fiber is connected to it. With this optical system, we can set the focal point easily as we look the object through a view screen of the finder. The other end of the quartz fiber is connected to the entrance of the "polychromator (Soma Optics Ltd., S-2210)" which consists of a grating and 1024 channel CCD linear array sensors, which enables an uptake of whole spectrum simultaneously. The optical emission can be observed with a range of 185∼525 nm with 0.34 nm resolution.

With this measurement system, Cu sputtering plasma was observed through a quartz view-port mounted on the sputter chamber as shown schematically in figure 3.19. The data were acquired by opening the shutter, the time of which was set to $1 \sim 2$ s in this study. The degradation of the transmittance by the view-ports could be neglected in this experimental condition. OES spectra were measured by focusing the camera on the position $5 \sim 10$ mm above the center of the target.

Typical OE spectra from the argon DC magnetron plasma with a copper target are shown in figure 3.20. The unit of the vertical axes of these figures is output of A/D converter of CCD array sensors. Emission lines have been identified using the ATMLINE, atomic line database provided by Kyoto University Data Processing Center [48]. Several emission lines could be assigned to Cu neutrals, Ar neutrals and Ar ions, and a part of them is listed in Table 3.1. The lines chosen as representatives of respective species are marked as (*), whose dependences on discharge parameters will be discussed in the following. Though it has been reported that Cu ion lines are observed at 213.6 nm [112] and at 404 nm [110], such peaks could not be separated clearly from other peaks around them in our system.

The Ar pressure dependence of intensities of (*) lines in Table 3.1 are shown in Fig. 3.21. The upper figure shows the results at the focal point of 5 mm above the center of the target, while the lower one shows that of 10 mm. DC discharge power was fixed at 100 W. The intensities of emission lines from Ar neutral/ion (420.1, 488.0 nm) are not strongly influenced by the Ar pressure, while those of the lines assigned to Cu neutral (324.8, 510.6 nm) increases with increasing the Ar pressure. These behaviors of emission lines agree with the reports on the magnetron plasma [26, 27], and on the ECR plasma [112].

In general, the electron density of the glow discharge plasma (including magnetron discharges) increases with increasing gas pressure. On the other hand, the electron temperature decreases with increasing pressure. Since it requires more than 10 eV to excite Ar atoms, the intensity of Ar emission does not increase even if electrons with medium and lower energies are generated steadily at high pressures. On the other hand, Cu neutrals can be excited with energies of $3 \sim 4$ eV, their emission intensities become stronger with increasing gas pressure. In addition, the spatial density of Cu atoms in the plasma becomes larger at high pressures, which

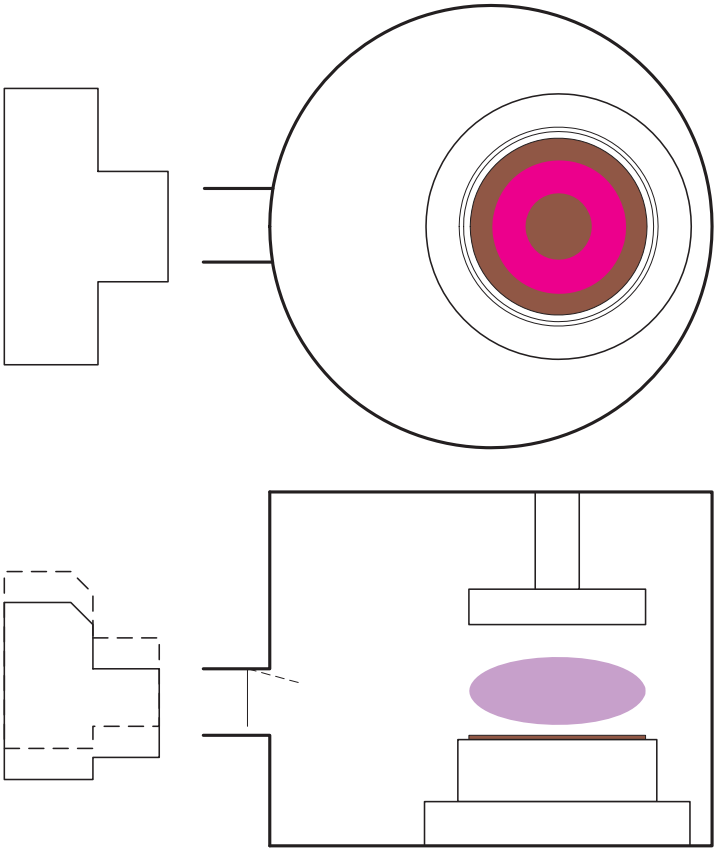

Figure 3.19: OES observation system.

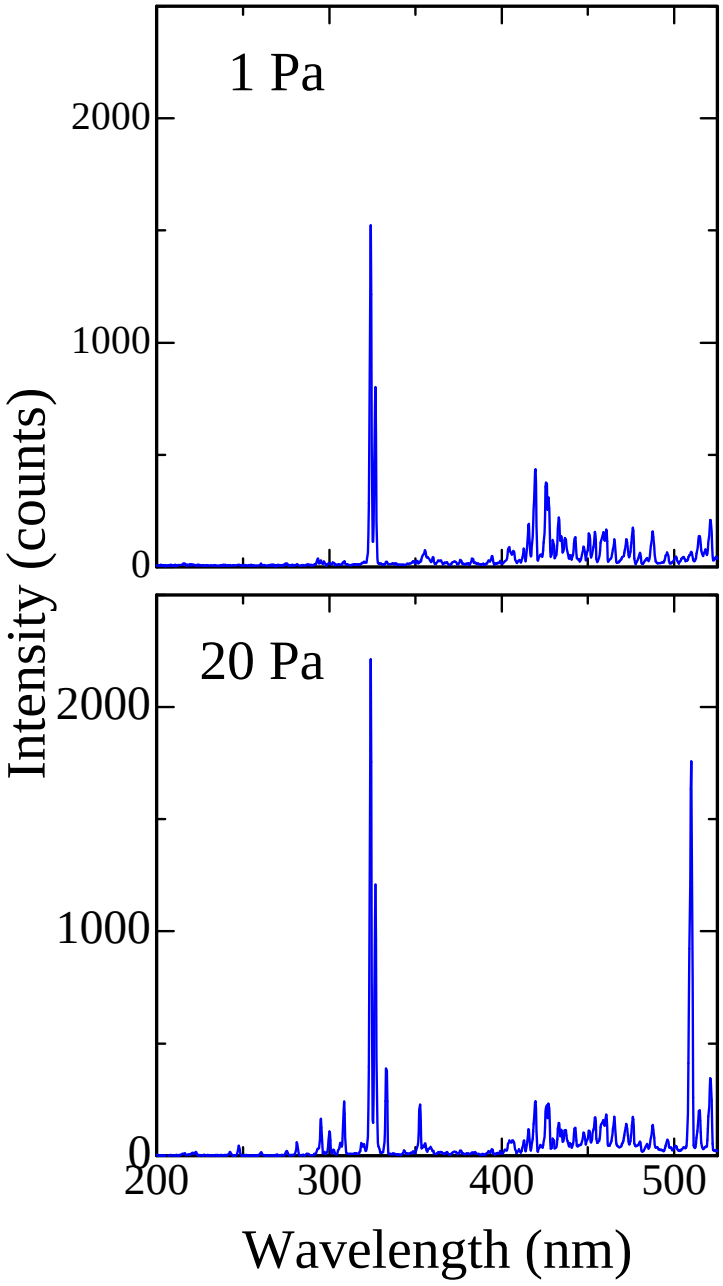

Figure 3.20: Optical emission spectra from DC sputter plasma with Cu target and Ar gas. Left: Ar pressure = 1 Pa, DC Power = 100 W, DC current = 0.15 A. Right: Ar pressure = 20 Pa, DC Power = 100 W, DC current = 0.26 A.

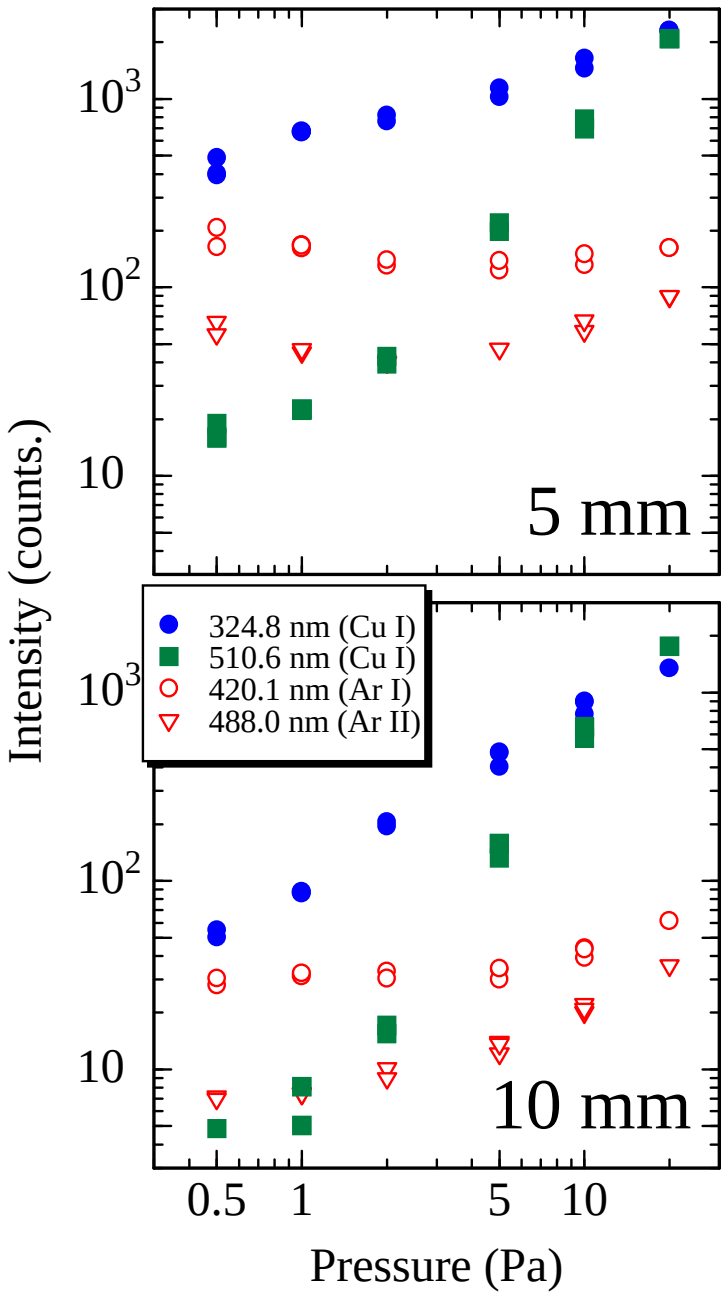

Figure 3.21: Pressure dependence of optical emission intensities from Cu/Ar magnetron sputter plasma.

Type	Wavelength (nm)	Upper Level (eV)	Lower Level (eV)
Cu I (*)	324.8	3.817	0
Cu I	327.4	3.786	0
Cu I (*)	510.6	3.817	1.389
Cu I	521.8	6.192	3.817
Ar I (*)	420.1	14.499	11.548
Ar I	425.9	14.735	11.828
Ar I	427.2	14.525	11.623
Ar II	442.6	19.549	16.749
Ar II(*)	488.0	19.680	17.140

Table 3.1: Emission lines assigned by ATMLINE. (*) lines are displayed in the following figures.

also contributes to the increase of Cu emission intensities. The Cu density increase also brings the consumption of the electrons of higher/medium energies, which may result in the "colder" plasma at higher pressures [112].

In figure 3.21, it is also shown that the intensity of 510.6 nm copper line increases much more steeply than 324.8 nm line with increasing pressure. And by comparing the results of 5 mm with those of 10 mm, ratios of argon intensities at 5 mm and at 10 mm are almost constant at any pressure, while the copper intensities at 10 mm increase more rapidly than at 5 mm as the pressure increases. Normally the plasma should be confined nearer to the target at higher pressures, hence it is interesting why the emission from 5 mm becomes less stronger in this case. The reason of these phenomena will be discussed in the next subsection.

Power dependences of OE intensities for several gas pressures are shown in Fig. 3.22. The observation position of these is 5 mm above the target. OE intensities of Ar lines are roughly proportional to the DC power P, while those of Cu are proportional to P^2. The latter may reflect: (1) flux of sputtered Cu atoms are proportional to P and (2) the excitation probability in the plasma is proportional to electron density n, which is also proportional to P. As consistent with Fig. 3.21, the peak intensity of 510.6 nm Cu line is much smaller than 324.8 nm Cu line at 1 Pa, but becomes comparable at 20 Pa. At 20 Pa, the 510.6 nm line intensity increases more rapidly than the 324.8 nm line with increasing the discharge power.

3.5.3 Self absorption effect of optical emission

In this subsection, we discuss the discharge parameter dependence of two emission lines from Cu neutrals, namely the lines at 324.8 nm and at 510.6 nm. The difference in pressure, power and positional dependence of them are considered relating to the atomic density of the copper.

As already shown in table 3.1, these two lines share the initial state at 3.817 eV. More

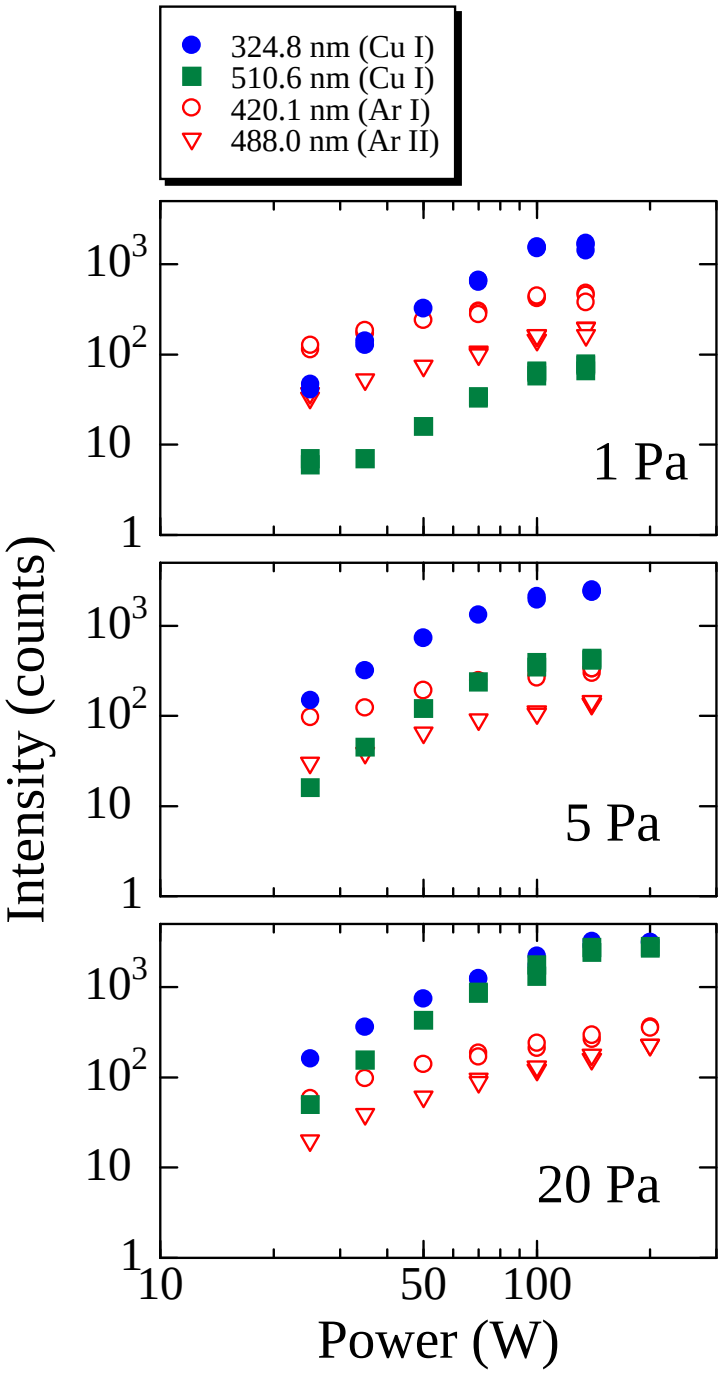

Figure 3.22: Discharge power dependence of optical emission intensities from Cu/Ar magnetron sputter plasma.

concretely, their initial and final states are [4]:

$$\begin{aligned} 324.8\text{nm} &: 4p\,^2\mathrm{P}^\circ_{1\,1/2} \rightarrow 4s^2\,\mathrm{S}_{1/2} \\ 510.6\text{nm} &: 4p\,^2\mathrm{P}^\circ_{1\,1/2} \rightarrow 4s^2\,^2\mathrm{D}_{2\,1/2} \end{aligned}$$

It should be noted here that the initial state of these two lines are identical, and that the final state of the former line is the ground state so that it is absorbed again by ambient Cu atoms at ground state. Assuming that the temperature of the electron system of copper atoms is comparable to the electron temperature of the plasma, most of the copper atoms should be at ground state. Hence, 324.8 nm emission can be reabsorbed by another copper atoms (at ground state) existing in the plasma, which is known as "self absorption effect". This means that the plasma with high atomic density of Cu is opaque for the light of 324.8 nm, while it is still transparent for the 510.6 nm lines since Cu atoms at the excited level $4s^2\,^2\mathrm{D}_{2\,1/2}$ are much less than those at ground state. Since the probabilities of these transition should be unchanged unless the induced emission occurs, the relative intensity of 510.6 nm light emission increases as the copper density increases.

According to the atomic absorption theory [162], the integration of the absorption spectrum $\kappa(\nu)$ for atoms with density N is given by:

$$\int \kappa(\nu) d\nu = \frac{\pi e^2}{mc} N f. \tag{3.8}$$

where f is an absolute oscillator strength, which is about 0.434 for 324.7 nm spectrum line of Cu neutral. Since the pressure is low in this case, the collisional broadening which gives the Lorentz profile should be weak. Hence the Doppler broadening rules the absorption spectrum, and it becomes a gaussian with the width $\Delta\nu$ of:

$$\Delta\nu = \frac{\nu_0}{c}\sqrt{\frac{2\ln 2\, kT}{M}}. \tag{3.9}$$

If we substitute this gaussian profile into eq. 3.8, the inverse of the absorption coefficient at the peak of the spectrum is:

$$\frac{1}{\kappa(\nu_0)} = \frac{6.64 \times 10^{14}}{N[\mathrm{m}^{-3}]}[\mathrm{m}] \tag{3.10}$$

at 300 K. It gives the decay length of the 324.7 nm emission. At the Cu density of $10^{17} \sim 10^{18}$, which has been obtained previously by the simulation, decay length is $6.6 \sim 0.66$ mm. It agrees the more gentle increase of 324.7 nm emission intensity at higher pressures where the Cu density is high, compared to the increase of unabsorbed emission at 510.6 nm.

This optical reabsorption process can also explain why the Cu intensities at 10 mm above the target increase more rapidly than at 5 mm with increasing the Ar pressures. The emission originated from nearer to the target must travel the thicker layer of dense Cu atmosphere so that the escape probability is smaller. In addition, copper atoms at 10 mm above the target may be excited by 324.8 nm photons originated from the dense plasma near the target, which also reduce the difference of emission intensity.

[4] Identification of the initial/final states is based on the ATMLINE database at Kyoto University Data Processing Center [48] and NBS databook compiled by Moore [86].

3.5.4 Summary

In summary, a novel method to evaluate the density profile of sputtered particles has been developed using Monte Carlo simulation. It has come to possible by the introduction of the gas motion into the MC, which is one of the achievements of this study. The method was applied to the Cu/Ar magnetron plasma, and the Cu atomic density of $10^{17} \sim 10^{18}\mathrm{m}^{-3}$ was obtained near the target, with DC discharge power of 100 W and gas pressures of $2 \sim 20$ Pa. The density increases with increasing the Ar pressure, and the spatial profile of Cu density can be explained considering the diffusion process of sputtered Cu atoms.

The same Cu/Ar plasma was observed by OES. It was found that the two emission lines from Cu atom (324.7 nm and 510.6 nm) showed different dependence on discharge parameters. The former is found to be reabsorbed by the ambient copper atoms at ground state, and the decay length of the 324.7 nm emission is deduced using the density value obtained by the simulation. As a result, some millimeters to submillimeters of decay length is obtained, which can explain the behavior of optical emission lines from Cu atom.

Chapter 4

Conclusion

In this thesis, we have studied the transport process of sputtered atoms from target to substrate, with both experiment and with computer simulation. Two new models have been proposed to extend the conventional Monte Carlo method, for more realistic simulation in high gas pressure environment. These models were implemented into the FORTRAN program code, and the computer simulation was performed. By comparing the simulation results with experiments, the validity of the model could be confirmed. The reasons of the experimentally observed phenomena have also been discussed from the viewpoint of particle transport process, and new understandings have been obtained.

In chapter 1, the background of this study was described. In sections 1.1–1.5, various problems relating to the sputter deposition process were reviewed. Theoretical reports and considerations were mainly treated, and relationships of them with the particle transport process was also discussed. In the next section (1.6), historical review of the studies on Monte Carlo (MC) simulation of particle transport process was presented. Latest achievements in this field were covered as well as possible, and the position and the significance of this study were shown.

In chapter 2, physical backgrounds of the simulation model were described. In sections 2.1–2.4, conventional MC models for particle transport problem were presented, and those which used in this study were mentioned in detail. The following two sections are the ones originally developed in this study. In section 2.5, we have introduced the thermal motion of ambient gas atoms into collision problem of the sputtered particles, and deduced the velocity (*i.e.*, speed and angle) profile of the colliding gas atoms and their dependencies on the particle speed. And in section 2.6, we have developed the method to treat the random diffusion transport of sputtered particles using Poisson's equation. The numerical method to solve this equation using the Boundary Element method (BEM) has also been described. By combining the MC and BEM methods, it was proved that the particle transport process could be solved in applicable periods of time with commercially available personal computers.

In chapter 3, we have applied the simulation to several problems in sputter deposition and shown the results. Firstly in section 3.1, we described experimental setup, with which the deposition experiment was performed and was compared with the simulation. Subsequently, the simulation methods, which had been explained in chapter 2, were summarized again.

In section 3.2, we applied the simulation to the deceleration process of high energy copper

atoms injected into argon gas environment without boundary. Especially, effect of the thermal motion of gas atoms were investigated by comparing the cases with gas temperatures of 400 K and 0 K. In the former, energy distribution of Cu atoms well reproduces the Maxwellian, while in the latter, gas atoms were immobile, it approaches zero since Cu atoms lose their energy on collision monotonically. It governs the time evolution of the spread of Cu atoms in real space; if the gas motion is neglected, the dispersion of Cu atoms effectively stops at some size. For example, this size is the order of centimeters when Ar pressure is 10 Pa. As a result, it has been proved to be important to consider the thermal motion of gases when you simulate the particle transport process in high pressure environment.

In section 3.3, thickness profile of the sputtered copper film has been investigated. It was shown that the profile changed by the distance between the substrate holder and the chamber wall. When the distance is small, film thickness decreases more steeply as apart from the holder center and close to the wall. It could be explained by the model introduced in section 2.6, where the chamber wall is regarded as the boundary with zero atomic density. When you prepare the film by sputter deposition in high pressure, it also deposits on the faces from which the target cannot be seen directly. It is because of the diversion of sputtered atoms caused by the scattering by gas atoms. It had been reported that the ratio of film thickness on substrates facing toward / away from the target (BFR ratio) showed the maximum at midst gas pressure [90]. It was also confirmed with our experiments that this BFR ratio decreased and approached constant at higher pressures where the diffusive transport became dominant. Using the simulation developed in this study, this tendency was reproduced well, and the reason was elucidated as follows. With the second extension of the simulation using the Poisson's equation, thermalization points of the sputtered atoms are treated as the particle sources. At pressures where the BFR ratio is maximum, these points distribute around the substrate holder so that the flux at the backface increases relatively. On the other hand, at very high pressures, thermalization points concentrate to the neighbors of the erosion track resulting in the decrease of the relative flux at the backface.

In section 3.4, the pressure dependence of the film composition was considered in case of LaB_6 sputter deposition. When the process pressure changed from 0.2 to 20 Pa, boron content showed the minimum at around 7 Pa. It is because of the difference in scattering angle with Ar gas atom. Boron, the lighter atom, is more likely to be backscattered by the argon atom, hence the pressure increase in the ballistic transport region (*i.e.*, low pressures) results in the decrease of boron content. On the contrary at high pressures, where the diffusive transport is dominant, mass difference scarcely affect the particle transport, and the composition recovers to the stoichiometry. That is to say, the competition between the ballistic transport and the diffusive transport is the cause of the peak in pressure dependence.

In section 3.5, we have proposed the method to evaluate the atomic density in the sputtering plasma using MC simulation. This has been achieved by the first extension of MC in this study, with which the motion of sputtered atom can be traced even after the many times of collisions with gases. The proposed method was applied to the same situation with section 3.3 (Cu deposition), and copper atomic density was calculated to be $10^{17} \sim 10^{18}\,\mathrm{m}^{-3}$. The sputter plasma in this condition was measured experimentally using optical emission spectroscopy equipment. It has been observed that the copper emission line, whose transition includes the ground state as the final one, becomes small when Cu atomic density is high (e.g., high gas pressure and/or high discharge power). We have assumed that this is because this emission is re-absorbed by the

ground state copper atoms in the plasma, and have estimated the decay length of this emission using the atomic density value obtained by the simulation. With it, we could successfully explain the emission intensity reduction observed by the experiment.

4.1 Future works

By closing this thesis, we would like to point out the limitations in the simulation developed here, and to suggest the desirable researches and developments in the future. Among the conditions and assumptions summarized in section 3.1, we consider that four of these are not always adequate. These are listed in the following,

- In this simulation, the ejection position of the sputtered particle is determined so as to reproduce the depth profile of the erosion track actually measured after the deposition experiment (2.2.1). Therefore, it cannot be considered as the *a priori* model applicable to the design of sputter deposition equipments. Moreover, the experimentally measured erosion track depth is actually the results of many times of deposition experiments with different discharge conditions. If, for example, the gas pressure changes, the ion production profile (hence the ion flux onto the target) may also change. To overcome this problem, the simulation should incorporate such models that can calculate the ion production from the magnetic field configuration, as mentioned in section 1.1.2.

- The angle and energy distributions of sputtered atoms are simply assumed to be the cosine distribution and the Thompson's formula, respectively. This is partly because that there are no satisfactory models for roughened targets after some time of the sputtering, nor for targets of compounds or alloys. As referred in section 1.2, there have been some calculation codes treating the collision cascade inside of the target with Monte Carlo method. You should check out and validate them by experiments, and combine them with particle transport simulations.

- The density and the temperature of the sputter gas are assumed to be uniform in the chamber. As mentioned in section 1.1.4, gas density reduction effect, caused by the high energy flux near the target (neutralized and recoiled gas ions, sputtered atoms, etc.), has been proposed. To treat this, gas dynamics has to be taken into account by DSMC method (appeared in section 1.3.3) or others.

- The sticking coefficient of sputtered atoms on the chamber wall is assumed to be unity, while it actually should be (slightly or considerably) less than 1. For the latter, new boundary condition must be introduced to the BEM treatment of the diffusion process of atoms.

A part of these proposals has already been performed, which are mentioned in section 1.6.4. It is desirable that these efforts will be merged into the generic and comprehensive calculation model of the sputter deposition process in the future.

Appendix A

Implementation

In this appendix, we describe the simulation program used in this study. At the first section, some of the important algorisms and libraries are mentioned. In the second section, detailed of the program package is explained: availability and the usage of the program, our computing environment, contents in the distribution archive, and the structure of the program.

A.1 Algorisms and libraries

A.1.1 Integration

As shown in section 2.3.2, the integration which gives the scattering angle has a singularity at the lower limit of its range (eq. 2.40). In our program, we avoid this problem by using the Double Exponential (DE) formula for numerical integration.

In DE formula, the integration

$$I = \int_0^\infty f(x)dx, \tag{A.1}$$

is converted using

$$x = \exp\left(2\sinh t\right). \tag{A.2}$$

After this conversion and the discretization of the integration, we obtain the summation form:

$$I_h = h \sum_{i=-\infty}^{\infty} f(\exp(2\sinh(ih)))\, 2\cosh(ih)\, \exp(2\sinh(ih)). \tag{A.3}$$

The conversion given by eq. A.2 uses the fact that the trapezoidal rule gives extremely accurate result for the integration of analytical function if the integral region is infinite for both positive and negative ends. In addition, the function in the summation of eq. A.3 approaches to zero double exponentially for $-\infty$ and ∞.

In the program, we have another integrals given by (eqs. 2.141 and 2.142). They are the integrals of complete elliptic functions to construct the coefficient matrix of the BEM method. For these, we have used Newton Cotes (NC) method of 8th order, instead of the DE, because of the better convergence.

The Fortran source codes of DE and NC methods have been published in reference [87] with detailed descriptions of theoretical backgrounds. In the courtesy of Professor Mori, they have been approved to use and to distribute with this program package.

A.1.2 Random number generation

For Monte Carlo simulations, it is critically important to use a pseudo random number generator that has a long period as well as good "randomness" (for the measure of randomness, see [66] for example).

In this study, we have adopted the "Mersenne Twister (MT)" random number generator. It has many preferable features, especially for MC calculation. Following is the quotation from the Mersenne Twister Home Page at:

`http://www.math.keio.ac.jp/~matumoto/emt.html`

> Mersenne Twister(MT) is a pseudo random number generator developed by Makoto Matsumoto and Takuji Nishimura (alphabetical order) during 1996-1997. MT has the following merits:
>
> - It is designed with consideration on the flaws of various existing generators.
> - The algorithm is coded into a C source downloadable below.
> - Far longer period and far higher order of equidistribution than any other implemented generators. (It is proved that the period is $2^{19937} - 1$, and 623-dimensional equidistribution property is assured.)
> - Fast generation. (Although it depends on the system, it is reported that MT is sometimes faster than the standard ANSI-C library in a system with pipeline and cache memory.) Efficient use of the memory. (The implemented C-code mt19937.c consumes only 624 words of working area.)

The C program is also available from the above url. We have modified it slightly to make it callable from our Fortran routines. Reference [71] has given us a lot of information about the usage of Fortran program in Unix, as well as to build its interface to C.

A.1.3 Spline function

In our simulation, we have to utilize some functions that need large computational complexity, including some kinds of inverse functions which cannot be solved analytically. To reduce the computational load for these, we introduce the spline function [20] to approximate these functions.

Spline function is a set of k-th polynomials, each of which has its own domain given by splitting the domain of the original function. On each domain boundary, the 1st ... $(k-1)$-th derivative of the polynomials of adjoining domains are requested to be continuous. A sequence of points ("nodes") are selected in the original domain, and values of the original function (which may need complex calculation) are evaluated at each point. Then the factor of the polynomials are determined so as to let the constructing "spline function" cross these points simultaneously.

In the following, we mention the applications of the spline function in this study.

- The function to represent the erosion track on the target. As described in section 2.2.1, ejection positions of sputtered atoms are determined so as to reproduce the depth profile of the erosion track. This depth profile function is achieved by the 1D spline function using the actually measured points shown in figure 3.2.

- The mean free path of the sputtered atom as a function of its speed (eq. 2.86). As shown in fig. 2.4, the nodes are chosen at the same interval on the logarithmic axis of the kinetic energy of the atom. The 1D spline function is constructed using these nodes, and is utilized in the simulation.

- The speed of the colliding gas atom as a function of the sputtered particle speed v_p and pseudo random number w (eq. 2.88). This is the 2D spline function, where the first parameter is taken to be the log of the sputtered particle energy $\log E_p$, and the second parameter is w. Nodes are taken at the same interval on both of these axes, and the spline function is constructed.

  However, since the spline function is the polynomial by its nature, it does not give a good approximation for eq. 2.88 at $w \sim 0$ and at $w \sim 1$. Therefore, we give the range $[w_{\min}, w_{\max}]$ only in which the spline function apply. At $w < w_{\min}$, we deduce the v_g using $w \propto {v_g}^3$, which is the asymptotic function of eq. 2.80 at $v_g << 1$, while at $w > w_{\max}$, we directly solve eq. 2.81 by the bisection method to obtain v_g.

- The scattering angle χ_0 as a function of collision parameter b and the relational kinetic energy $E_r \equiv \mu {v_0}^2/2$ in the potential scattering problem (eq. 2.40). The one parameter is b while the other is $\log E_r$. The nodes are taken on both axes at the same interval, and the 2D spline function is deduced.

  Since this is the even function for b, $d\chi_0/db$ is zero at $b = 0$. It is possible to incorporate this restriction when constructing the spline function, but it has not been implemented yet.

The 1D and 2D spline functions used in this study has been implemented from scratch based on the reference [141].

When you construct the spline functions, you have to solve the linear simultaneous equations with the rank equal to the number of nodes. Since the coefficient matrix of this simultaneous equations is sparse, it is solved using the SPARSE library, which has been developed for solving large sparse linear systems. The SPARSE library can be obtained from:

`http://www.netlib.org/sparse/`

Though this is written in C, the procedure to use it from FORTRAN is also documented in their distribution archive. In our program, it is utilized after applying this modification.

A.1.4 Matrix calculation

In the boundary element method, you must solve the linear simultaneous equation given in eq. 2.145. It is done by the LAPACK library [4] which is a comprehensive FORTRAN library

for versatile linear algebra operations. It has been used in various fields for scientific calculations, including Finite Element Method, etc. The source code is in the public domain and is available at:

`http://www.netlib.org/lapack/`

A.1.5 Special functions

In section 2.6, we have used the complete elliptic functions of 1st and 2nd kind on calculating the fundamental solutions in axisymmetrical Poisson's problem (eqs. 2.134 and 2.135). The routines to calculate these functions have been taken from the SLATEC Library, which can be found at:

`http://www.netlib.org/slatec/`

SLATEC is also a well known library written in FORTRAN, which includes over 1400 of routines for scientific calculations. The result of the complete elliptic functions are checked with tables in reference [88] before applying the calculation to our simulation.

Another special function used in our simulation is the Gaussian error function (eq. 2.83). The g77 Fortran compiler we used (see below) has this routine in intrinsics as one of non-standard extensions, and we use it. If your Fortran compiler does not have this function internally, you can use the routine `derf.f` in the SLATEC.

A.2 Simulation Program

A.2.1 Availability and requirements

We named the simulation program used in this study as *HISPUT*. The archive including the whole sources is available from our web site at

`http://surf.ap.seikei.ac.jp/HISPUT/`

in a tar+gzip'ed archive. It has been developed using the CVS (Concurrent Versions System [1]). The access via Anonymous CVS will be available in the near future.

The sources are written mainly in Fortran, and partly in C. CPP preprocessing language is used also in some Fortran sources to enable/disable debugging codes, to modify maximum sizes of various arrays, and to specify basic physical constants. Two routines are written in C. One is the MT random number generator (see above), and the other is for the specifier of the FPU behaviour on error during the calculation.

We have used GCC (GNU Compiler Collection [2]) to compile our program. It currently contains C and Fortran compilers (which we have used), as well as ones for C++, Objective-C, Java, etc. It has been proved to be matured and stable during the long period of its development. The compilation/linking procedures are automated using "make" utility [3]. GNU version of make

[1] `http://www.cvshome.org`
[2] `http://gcc.gnu.org/`
[3] `http://www.gnu.org/software/make/`

has some extended syntaxes, and we use them. Therefore, automatic build may not work with traditional make utility.

On developing and executing the programs in this study, we have used Debian GNU/Linux operating system [4] running on IBM PC. Debian GNU/Linux is a freely available UNIX like system. It comes with more than 3000 software packages, which includes C/Fortran compilers, scientific libraries, graphic tools, etc. Version 2.2 (codename *potato*) is mainly used with some extra packages installed, e.g.:

- cpp, g77, gcc
- make
- lapack, lapack-dev, blas1, blas-dev
- slatec, slatec-dev

The last two items are packages of LAPACK and SLATEC libraries, respectively.

A.2.2 Directory structure of the distribution archive

In this subsection, we mention the contents of the distribution archive by its directory structure. The files and routines included in each directory are described briefly. The source codes in this archive can be redistributable under the terms of GNU General Public License [5], except for the ones under the `contrib/` directory.

src/ Main routines of the *HISPUT* program. Files and routines in this directory are described in the next subsection.

lib/ The routines which can be used for generic purpose. Currently, there is only one subdirectory.

- **nakano/** This subdirectory contains: 1D/2D spline functions, 1-argument equation solver using bisection method, and the FPU control interface for FORTRAN.

contrib/ This directory is the collection of routines developed by other groups. If you run make with the Makefile in this directory, you can build the library file including these.

- **mt/** Mersenne Twister routines.
- **mori/** A part of routines included in reference [87], e.g., the DE formula and the NC method of 8th order.
- **slatec/** A selection of SLATEC routines utilized in our simulation program.
- **sparse/** SPARSE library routines applied the patch to be callable from FORTRAN.

examples/ Originally, these have been developed to check the respective routines in the *HISPUT* program. Some of them also are used to prepare the figures presented in this thesis.

[4] `http://www.debian.org/`
[5] `http://www.gnu.org/copyleft/gpl.html`

mt/ Test code for Mersenne Twister.

spline/ Test code for spline function routines.

bem/ Test code for BEM routine. The BEM data in fig. 2.6 are the result of this routine.

bemcmp/ Sample program to output the MC data in fig. 2.6.

eject/ Test codes for routines treating the ejection of the sputtered atom from the target.

coldist/ Test code to calculate the distribution of colliding gas speed v_g for given energy of the sputtered atom (eq. 2.88).

colgas/ Test codes to obtain several parameters for the sputtered atom flying through the gas environment with finite temperature, e.g., mean free path of the sputtered atom, and velocity of colliding gas atom. Used to prepare fig. 2.4.

vrel/ Sample code to calculate the relative speed between the sputtered atom and the gas atom. Used to prepare fig. 2.5.

scatter/ Sample code to calculate the scattering angle from the collision parameter and the kinetic energy of the sputtered atom when the gas atom is stationary. Used to prepare figs. 2.2 and 3.13.

trap/ Test code for the routine accounting the particle trap on the chamber wall.

inc/ Test code for the routine to calculate the residual time of the sputtered atom in an arbitrary cell located inside of the chamber.

spreadf/ Routines and execution rules to obtain the time evolution of high energy atoms spread into the free space filled with gas. Used to prepare the figures shown in section 3.2.

spreadb/ Routines and execution rules to obtain the evolution of sputtered atoms in an actual sputtering environment. Used to prepare fig. 3.7.

thesis-figs/ Rules and tools to obtain a series of physical parameters using *HISPUT* for different sputtering conditions (pressures, ejection energies, etc.). They include the script to prepare the input data, the batch program to execute the *HISPUT* with these input data files, and the script to summarize the calculation results.

00common/ Some blocks for the input data for the *HISPUT*, which can be used commonly: chamber boundaries, depth profile of the target erosion track, atomic parameters, etc.

copper-tt/ Rules to obtain the dependence of the calculation results on the thermalization threshold energy (section 2.6.7).

copper/ Rules to evaluate the thickness profile of sputtered Cu films (section 3.3).

LaB6/ Rules to evaluate the pressure dependence of the film composition in LaB_6 sputtered films (section 3.4).

density/ Rules to evaluate the atomic density profile of Cu sputtered atoms (section 3.5).

A.2.3 Source file and routines

In this subsection, files in `src/` directory are mentioned. Functions and subroutines contained in them are also explained briefly.

It is ruled that the common blocks are hidden from outside of the file. In other words, they are referenced only from the routines in the same file, and the special interface routine are prepared to set the values to the variables in them.

For input/output of the program, device numbers 0, 5, 6, 9, 10 are used. The purpose of these and the relationships with the Unix (Linux) devices are summarized in table A.1.

Number	Device	Purpose
0	`/dev/stderr`	To output debug information and errors
5	`/dev/stdin`	To input calculation parameters
6	`/dev/stdout`	To output miscellaneous information
9	(user defined)	To input cell data (see `inc.F`)
10	(user defined)	To output calculation data

Table A.1: I/O Devices used in *HISPUT*

The files with suffix `.F` are the sources that need to be processed by the C preprocessor before the compilation by the FORTRAN compiler, while those with suffix `.f` are the sources directly passed to the FORTRAN compiler.

main.F Main program.

> **program hisput** Main program routine.

readin.F The routine to read the parameters passed to the program.

> **subroutine readin** The routine to read the parameters passed to the program. The name of the output file which will be allocated to the device number 10 is also read from this input file.

input.dat.samp Sample file to be read by `subroutine readin`.

aeject.F Calculate the ejection angle of the sputtered atom (see section 2.2.3).

> **subroutine aeject** Calculate the ejection angle of the sputtered atom from the target using Monte Carlo method.

eeject.f Calculate the ejection energy of the sputtered atom (see section 2.2.2).

> **subroutine eeject** The routine to obtain the ejection energy of the sputtered atom.

function fe Thompson's formula (eq. 2.18).

subroutine seteej Set the parameters in `common block ceej` to be used by `eeject` and `fe`.

function dfe Derivative of the `fe` function. Used to obtain the maximum of `fe`.

peject.F Calculate the ejection position of the sputtered atom (see section 2.2.1).

subroutine peject The routine to deduce the ejection position of the sputtered atom using eq. 2.4. Set `common block epej`.

subroutine setpej Initialization routine for `peject`. Construct the spline function to represent the depth profile of the erosion track.

function ddpej Derivative of the depth profile function of the erosion track. Used to obtain the maximum of the depth profile.

bem.F Calculate the diffusive stage of the particle transport by boundary element method (BEM) (see section 2.6).

subroutine bem Main routine of BEM.

subroutine bmform Generate the matrix in eq. 2.145.

subroutine elmoff Calculate the off-diagonal component of the matrix in eq. 2.145.

subroutine elmdia Calculate the diagonal component of the matrix in eq. 2.145.

subroutine pivttq After the matrix is generated, swap the known/unknown components to be handled by the LAPACK routines.

subroutine boundr Resume the positions of components swapped by `pivttq` after the equation is solved.

bemsrc.F Calculate the source term from the thermalized position of the sputtered atom using eq. 2.146.

subroutine setbemsrc Initialize the array.

subroutine bemsrc Calculate the value inside of the summation of eq. 2.146. This subroutine will be called every time when the sputtered atom is thermalized during the Monte Carlo step.

subroutine readbemsrc Read out the sum of each node after the Monte Carlo calculation is over.

itq.f Deduce the value of fundamental solution on each node (see sections 2.6.3–2.6.5).

function ts $\bar{\theta}^*$ in eq. 2.134.

function tsi Integrand $\bar{\theta^*}\left(x^{(i)}, x'\right) R\left(x'\right)$ in eq. 2.142.

function qsi Integrand $\bar{q^*}\left(x^{(i)}, x'\right) R\left(x'\right)$ in eq. 2.141.

subroutine preptq Initialization routine for `tsi` and `qsi`. Set `common block citq`.

ellipt.f Interface functions for the SLATEC routines of complete elliptic functions.

function dellf Interface function for the complete elliptic function of 1st kind.

function dells Interface function for the complete elliptic function of 2nd kind.

cdir.F Determine the velocity of the sputtered atom after the collision with gas atom (see section 2.5.3).

subroutine cdir Determine the velocity of the sputtered atom after the collision with gas atom.

subroutine setcdir Preparation routine for `cdir`. Set values in `common block ccdir`.

subroutine roty Rotation around the y axis (eq. 2.91).

subroutine rotz Rotation around the z axis (eq. 2.92).

subroutine relv Deduce the relative speed between the sputtered atom and the gas atom using eq. 2.89.

coldist.F Calculate the probability function of the gas speed colliding to the sputtered atom flying through the thermal gas environment (see section 2.5.2).

subroutine setdist Initialization routine for `distf` function. Set values in `common block ccoldf`. It takes the speed of the sputtered particle as an argument. Note that you have to call this routine before calling `distf` when the the sputtered particle speed changes.

function distf Calculate the right hand side of eq. 2.88.

colgas.F Routines to determine the mean free path of the sputtered particle traveling through the gas environment, and the speed of the colliding gas atom to it.

subroutine colgas Deduce the speed of colliding gas atom using the inverse function of eq. 2.88. Actually it uses a spline function set by `setcol`.

subroutine frpath Deduce the mean free path of the sputtered particle from eq. 2.86. Actually it uses a spline function set by `setcol`.

subroutine setcol Prepare the spline functions for `colgas` and `frpath`. Set the variables in `common block ccol` and `cmfp`.

function bfun The function called from `setcol`. Used on solving the eq. 2.88 for v_g by the bisection method.

subroutine setbfun Set the pseudo random number w to `common block cgaswp` to use it as a internal parameter of `bfun`.

scatter.F Calculate the scattering angle in the potential scattering framework (see section 2.3.2).

subroutine scat Return the scattering angle χ_0 obtained by eq. 2.40. Actually it uses a spline function set by `setsca`.

subroutine setsca Prepare the spline function for `scat`. Set the variables in `common block csct`.

function scint1 Integrand in eq. 2.40.

function scint2 Denominator of the `scint1`. Also used to determine the lower limit of the integration by eq. 2.41.

sp.f Born-Mayer (BM) type scattering potential (eq. 2.46).

function sp Returns the value of BM potential. It takes the distance r as a parameter.

subroutine setsp Set the parameters A and b of the BM potential to `common block csp`.

trap.F Deciding routine of the trap of sputtered atoms on chamber wall nodes (see section 2.4).

subroutine trap Decide the trap of sputtered atoms on chamber wall.

subroutine settrap Initialization routine for `trap`. Store the positions of boundary nodes in `common block ctrap`.

inc.F Calculate the residual time of sputtered atoms (see section 3.5).

subroutine inc Calculate the residual time of sputtered atoms.

subroutine setinc Initialization routine for `inc`. Read the input from device 9 and set values to `common block cincp`.

subroutine repinc Output routine.

subroutine pinner Decide if the sputtered particle is inside of the cell of the specified index.

subroutine iswap Swap two integers.

subroutine dswap Swap two double precisions.

inc.dat.samp Sample file to be read by `subroutine inc`. The device number 9 will be allocated to this file.

ecross.f Routine to determine whether the linear path of the sputtered atom in 3D space crosses the line node in RZ space of the axisymmetric coordinate (see section 2.4).

subroutine ecross Routine to determine if the linear path of the sputtered atom in 3D space crosses the line node in RZ space of the axisymmetric coordinate.

subroutine scross Initialization routine for `ecross`. Set variables in `common block ccross`.

subroutine rcross Sort routine called by `ecross`.

axarea.F Calculate the area in 3D of the nodes obtained by splitting the axisymmetric chamber boundary in RZ plane.

subroutine axarea For axisymmetric space, calculate the area of the line node in RZ space.

The call tree of these functions and subroutines are visualized in figure A.1. This only includes the routines in the files at `src/` directory, and not the ones in the files at `lib/` nor at `contrib/`.

Program `hisput` can be built automatically by running the make utility with the `Makefile` in this `src/` directory.

With this program, you can execute the simulation by:

```
% ./hisput < input.dat.samp > output.dat
```

For detail of this execution procedure, please refer the input data generated by executing the `mkinputs.pl` script and the batch file `do.sh` contained in subdirectories under `thesis-figs/`.

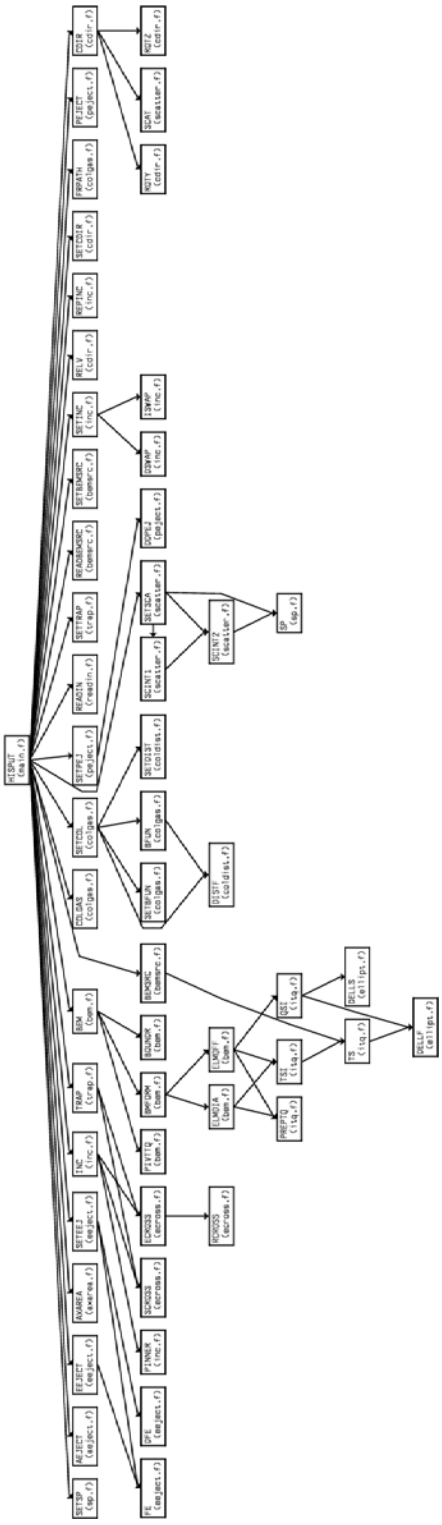

Figure A.1: Call tree of *HISPUT* subroutines.

Appendix B

Atomic Parameters

This table gives the atomic/elemental parameters used in the MC simulation of this study, which include mass M, Born-Mayer potential (BMP) parameters A, b, and surface binding energy U_s. Atomic mass is taken from [100], BMP parameters are from [1], and surface binding energy is from [177]. Atomic mass is shown both in atomic unit and in kg.

Table B.1: Atomic mass and potential parameters

Z	Sym	M/a.u.	$M/10^{-27}$kg	$A/\ (e^2/a_0)$	A/eV	$b/\ ({a_0}^{-1})$	$b/\text{Å}^{-1}$	U_s/eV
2	He	4.002602	6.646482	8.6047	234.13	2.20779	4.17217	
3	Li	6.941	11.526	16.109	438.33	2.12081	4.00780	
4	Be	9.012182	14.96509	24.599	669.34 [1]	2.05904	3.89107	3.32
5	B	10.811	17.952	35.606	968.84	2.02771	3.83187	5.77
6	C	12.0107	19.9443	48.367	1316.1	2.01592	3.80959	7.37
7	N	14.00674	23.25875	62.840	1709.9	2.00900	3.79651	
8	O	15.9994	26.5676	78.771	2143.4	2.00474	3.78846	
9	F	18.9984032	31.547612	96.267	2619.4	2.00229	3.78383	
10	Ne	20.1797	33.5092	114.72	3121.5	1.99954	3.77863	
11	Na	22.989770	38.175437	134.56	3661.4	1.99899	3.77759	
12	Mg	24.3050	40.3594	140.72	3829.0	1.95694	3.69813	
13	Al	26.981538	44.803928	157.85	4295.1	1.94681	3.67899	3.39
14	Si	28.0855	46.6371	186.39	5071.7	1.95888	3.70180	4.63
15	P	30.973761	51.433175	205.67	5596.3	1.95137	3.68760	
16	Si	32.066	53.247	222.99	6067.6	1.94026	3.66661	
17	Cl	35.4527	58.8706	235.64	6411.8	1.92449	3.63681	
18	Ar	39.948	66.335	255.82	6960.9	1.91901	3.62645	
19	K	39.0983	64.9243	277.95	7563.0	1.91634	3.62141	
20	Ca	40.078	66.551	298.57	8124.1	1.91044	3.61026	
21	Sc	44.955910	74.651096	319.62	8696.9	1.90544	3.60081	
22	Ti	47.867	79.485	343.72	9352.6	1.90402	3.59812	4.85

[1] It is 699.34 in ref. [1], but it must be an error since it is inconsistent with the value of e^2/a_0.

Table B.1: Atomic mass and potential parameters

Z	Sym	M/a.u.	$M/10^{-27}$kg	$A/\ (e^2/a_0)$	A/eV	$b/\ (a_0{}^{-1})$	b/Å^{-1}	U_s/eV
23	V	50.9415	84.5904	366.70	9977.9	1.90077	3.59198	5.31
24	Cr	51.9961	86.3416	389.77	10606	1.89794	3.58663	4.10
25	Mn	54.938049	91.226839	414.53	11279	1.89607	3.58310	2.92
26	Fe	55.845	92.733	438.46	11931	1.89300	3.57730	4.28
27	Co	58.933200	97.860948	463.35	12608	1.89116	3.57382	4.39
28	Ni	58.6934	97.4628	487.72	13271	1.88818	3.56819	4.44
29	Cu	63.546	105.52	511.53	13919	1.88457	3.56137	3.49
30	Zn	65.39	108.58	539.78	14687	1.88424	3.56074	
31	Ga	69.723	115.778	564.68	15365	1.88099	3.55460	
32	Ge	72.61	120.57	590.33	16063	1.87903	3.55090	3.85
33	As	74.92160	124.41033	618.26	16823	1.87833	3.54958	
34	Se	78.96	131.12	645.35	17560	1.87688	3.54684	
35	Br	79.904	132.684	672.43	18297	1.87495	3.54319	
36	Kr	83.80	139.15	703.70	19148	1.87520	3.54366	
37	Rb	85.4678	141.9227	731.90	19915	1.87373	3.54088	
38	Sr	87.62	145.50	763.87	20785	1.87395	3.54130	
39	Y	88.90585	147.63174	792.10	21553	1.87249	3.53854	
40	Zr	91.224	151.481	819.91	22310	1.87042	3.53463	6.25
41	Nb	92.90638	154.27478	850.89	23153	1.86990	3.53365	7.57
42	Mo	95.94	159.31	881.65	23990	1.86926	3.53244	6.82
43	Tc	99	164.4	911.85	24811	1.86489	3.52418	
44	Ru	101.07	167.83	941.72	25624	1.86723	3.52860	6.74
45	Rh	102.90550	170.87872	972.66	26466	1.86643	3.52709	5.75
46	Pd	106.42	176.71	1005.2	27352	1.86599	3.52626	3.89
47	Ag	107.8682	179.1195	1040.7	28318	1.86657	3.52735	2.95
48	Cd	112.411	186.663	1071.1	29145	1.86521	3.52478	
49	In	114.818	190.660	1102.6	30002	1.86416	3.52280	
50	Sn	118.710	197.123	1140.2	31025	1.86510	3.52458	3.14
51	Sb	121.760	202.187	1171.4	31874	1.86382	3.52216	
52	Te	127.60	211.88	1199.4	32636	1.86136	3.51751	
53	In	126.90447	210.7300	1231.2	33501	1.86020	3.51532	
54	Xe	131.29	218.01	1265.2	34426	1.85980	3.51456	
55	Cs	132.90545	220.69484	1298.9	35343	1.85901	3.51307	
56	Ba	137.327	228.037	1336.4	36363	1.85956	3.51411	
57	La	138.9055	230.6582	1370.2	37283	1.85891	3.51288	
58	Ce	140.116	232.668	1403.3	38184	1.85796	3.51108	
59	Pr	140.90765	233.98282	1436.0	39074	1.85679	3.50887	
60	Nd	144.24	239.52	1471.5	40040	1.85664	3.50859	
61	Pm	145	240.7	1508.4	41044	1.85651	3.50834	
62	Sm	150.36	249.68	1544.3	42020	1.85621	3.50778	
63	Eu	151.964	252.342	1580.5	43005	1.85606	3.50749	

Table B.1: Atomic mass and potential parameters

Z	Sym	M/a.u.	$M/10^{-27}$kg	$A/\ (e^2/a_0)$	A/eV	$b/\ ({a_0}^{-1})$	$b/\text{Å}^{-1}$	U_s/eV
64	Gd	157.25	261.12	1615.9	43969	1.85571	3.50683	
65	Tb	158.92534	263.90192	1651.4	44935	1.85512	3.50572	4.05
66	Dy	162.50	269.84	1688.7	45950	1.85513	3.50573	
67	Ho	164.93032	273.87343	1724.9	46935	1.85465	3.50483	
68	Er	167.26	277.74	1765.1	48028	1.85493	3.50536	
69	Tm	168.93421	280.52205	1801.4	49016	1.85449	3.50452	2.42
70	Yb	173.04	287.34	1842.3	50129	1.85489	3.50528	
71	Lu	174.967	290.540	1879.8	51149	1.85459	3.50471	
72	Hf	178.49	296.39	1914.1	52083	1.85344	3.50254	6.44
73	Ta	180.9479	300.4712	1952.7	53133	1.85346	3.50258	8.1
74	W	183.84	305.27	1991.2	54181	1.85300	3.50171	8.9
75	Re	186.207	309.204	2028.1	55185	1.85231	3.50041	8.03
76	Os	190.23	315.88	2067.9	56268	1.85240	3.50058	8.17
77	Ir	192.217	319.184	2104.6	57266	1.85190	3.49963	6.94
78	Pt	195.078	323.934	2144.2	58344	1.85191	3.49965	5.84
79	Au	196.96655	327.07087	2185.7	59473	1.85204	3.49989	3.81
80	Hg	200.59	333.09	2230.0	60678	1.85254	3.50084	
81	Tl	204.3833	339.3867	2270.7	61786	1.85246	3.50069	
82	Pb	207.2	344.1	2311.8	62904	1.85258	3.50092	
83	Bi	208.98038	347.02032	2349.2	63922	1.85164	3.49914	
84	Po	210	348.7	2395.9	65192	1.85224	3.50027	
85	At	210	348.7	2434.6	66246	1.85173	3.49931	
86	Rn	222	368.6	2476.5	67386	1.85163	3.49912	
87	Fr	223	370.3	2517.4	68499	1.85137	3.49863	
88	Ra	226	375.2	2623.0	71372	1.86368	3.52189	
89	Ac	227	376.9	2665.6	72531	1.86360	3.52174	
90	Th	232.0381	385.3086	2716.9	73927	1.86470	3.52382	6.2
91	Pa	231.03588	383.64437	2761.1	75130	1.86480	3.52401	5.55
92	U	238.0289	395.2566	2806.6	76368	1.86519	3.52475	

Acknowledgement (in Japanese)

本論文のご指導を快諾していただき、多くの有益なご指摘を賜りました東京大学教授 吉田豊信 博士に心より感謝致します。また本論文の審査を引き受けていただき、同じく多くのご意見を頂きました東京大学教授 堀池靖浩 博士、東京大学教授 鳥海 明 博士、東京大学助教授 渡邊 聡 博士、東京大学助教授 近藤高志 博士に深く感謝します。

成蹊大学教授 馬場 茂 博士には、本論文に関連する研究の遂行にあたり常に快適な研究環境を与えていただくとともに、様々なご指導をいただきました。

金沢工業大学教授 金原 粲 博士は、筆者の学生時代からの延長でもある本研究に関して、継続して有益なご指摘をくださいました。

京都大学教授 森 正武 博士は、本研究で開発したシミュレーションプログラムにおいて、ご著書の FORTRAN ルーチンを利用すること、およびそのルーチンを含むソースコードを公開・配布することを快諾してくださいました。

京都大学助教授 松本 眞 博士には、乱数発生ルーチン "Mersenne Twister" の利用に関してご教示をいただきました。

成蹊大学教授 小島紀徳 博士ならびに岐阜大学助教授 上宮成之 博士には、LaB_6 膜の ICP-Mass 測定を行っていただきました。

国立科学博物館 洞口俊博 博士 には、京都大学大型計算機センター ATMLINE データベースの利用に関するご教示をいただきました。

バキュームプロダクツ株式会社の 大橋哲二 氏には、本研究で利用した製膜装置の設計にあたって有益なご意見をいただき、また実際に作製を行っていただきました。成蹊大学機械工作室 佐藤道憲 氏には、実験装置の作製の一部をご指導いただきました。

最後に、成蹊大学物理情報工学科 (前 計測数理工学科) 表面物性研究室の学生諸君には、様々な形で本研究の遂行を助けていただきました。特に森 意佐央君にはガス熱運動を取り扱うルーチンの開発において、大貫徳之君には Cu プラズマの分光測定において、それぞれ協力していただきました。ここに記して感謝の意を表します。

Bibliography

[1] A. A. Abrahamson. Born-Mayer-type interatomic potential for neutral ground-state atoms with $Z = 2$ to $Z = 105$. *Phys. Rev.*, 178:76 – 79, 1969.

[2] J. B. Almeida. Design of magnetrons for dc sputtering. *Vacuum*, 39:717 – 721, 1989.

[3] J. N. Avaritsiotis and C. D. Tsiogas. A reactive sputtering process model for symmetrical planar diode system. *Thin Solid Films*, 209:17 – 25, 1992.

[4] Z Bai, C. Bischof, J. Demmel, and J. Dongarra. *Lapack Users' Guide*. the Society of Industrial and Applied Mathematics, Philadelphia, 2nd package edition, 1995. (editor: E. Anderson).

[5] L. T. Ball, I. S. Falconer, D. R. McKenzie, and J. M. Smelt. An interferometric investigation of the thermalization of copper atoms in a magnetron sputtering discharge. *J. Appl. Phys.*, 59(3):720 – 725, 1986.

[6] Albert-László Barabási and H. Eugene Stanley. *Fractal concepts in surface growth*. Cambridge Univ. Press, Cambridge, 1995.

[7] S. Berg and I. B. Katardjiev. Preferencital sputtering effects in thin film processing. *J. Vac. Sci. Technol. A*, 17(4):1916 – 1925, 1999.

[8] G. A. Bird. *Molecular gas dynamics and the direct simulation of gas flows*. Oxford University Press, New York, 1994.

[9] A. J. Blair, G. Metzger, and C. B. Fleddermann. Optical absorption spectroscopic diagnostics during sputter deposition of Y-Ba-Cu-oxide. *J. Appl. Phys*, 72(10):4792 – 4797, 1992.

[10] A. Bogaerts, R. Gijbels, and W. J. Goedheer. Hybrid Monter Carlo-fluid model of a direct current glow discharge. *J. Appl. Phys.*, 78(4):2233 – 2241, 1995.

[11] A. Bogaerts, J. Naylor, M. Hatcher, W. J. Jones, and R. Mason. Influence of sticking coefficients on the behavior of sputtered atoms in an argon glow discharge: Modeling and comparison with experiment. *J. Vac. Sci. Technol. A*, 16(4):2400 – 2410, 1998.

[12] Annemie Bogaerts, Mark van Straaten, and Renaat Gijbels. Description of the thermalization process of the sputtered atoms in a glow discharge using a three dimensional Monte Carlo method. *J. Appl. Phys.*, 77(5):1868 – 1874, 1995.

[13] R. Mark Bradley and James M. E. Harper. Theory of ripple topography induced by ion bombardment. *J. Vac. Sci. Technol. A*, 6(4):2390 – 2395, 1988.

[14] L. C. Wrobel C. A. Brebbia, J. C. F. Telles. *Boundary Element Techiniques Theory and Applications in Engineering*. Springer-Verlag, Berlin, 1984.

[15] C. C. Chang. Energy dependence of angular distributions of sputtered particles from the Ag{111} surface. *Phys. Rev. B:*, 48(20):12399 – 12405, 1993.

[16] J. W. Coburn and E. Kay. Positive-ion bombardment of substrates in rf diode glow discharge sputtering. *J. Appl. Phys.*, 43:4965 – 4971, 1972.

[17] Radlfo Cuerno and Albert-László Barabási. Dynamic scaling of ion-sputterd surfaces. *Phys. Rev. Lett.*, 74(23):4746 – 4749, 1995.

[18] Rodolfo Cuerno, Hernan A. Makse, Silvina Tomassone, Stephen T. Harrington, and H. Eugene Stanley. Stochastic model for surface erosion via ion sputtering: Dynamical evolution from ripple morphology to rough morphology. *Phys. Rev. Lett.*, 75(24):4464 – 4467, 1995.

[19] J. J. Cuomo and S. M. Rossnagel. Hollow-cathode-enhanced magnetron sputtering. *J. Vac. Sci. Technol. A*, 4(3):393 – 396, 1986.

[20] Carl de Boor. *A Practical Guide to Splines*. Springer-Verlag, New York, 1978.

[21] M. P. Desjarlais. The effect of charge exchange processes on ion diode impedance. *J. Appl. Phys.*, 66:4696 – 4701, 1989.

[22] S. K. Dew. Theoretical and practical aspects of collimated sputtering. *J. Appl. Phys.*, 76(8):4857 – 4862, 1994.

[23] S. K. Dew, T. Smy, R. N. Tait, and M. J. Brett. Modeling bias sputter planarization of metal films using a ballistic deposition simulation. *J. Vac. Sci. Technol. A*, 9(3):519 – 523, 1991.

[24] Steven Dew, Tom Smy, and Michael Brett. Step coverage, uniformity and composition studies using intergrated vapour transport and filim deposition models. *Jpn. J. Appl. Phys.*, 32(2):1140 – 1145, 1994.

[25] M. F. Dony, J. P. Dauchot, M. Wautelet, M. Hecq, and A. Richard. Diagnostics by optical absorption of sputtered atom density in magnetron discharges. *J. Vac. Sci. Technol. A*, 18(3):809 – 813, 2000.

[26] M. F. Dony, A. Ricard, J. P. Dauchot, M. Hecq, and M. Wautelet. Optical diagnostics of d.c. and r.f. argon magnetron discharges. *Surf. Coatings Technol.*, 74-75:479 – 484, 1995.

[27] M. F. Dony, A. Ricard, M. Wautelet, J. P. Dauchot, and M. Hecq. Comparison of direct current and radio frequency argon discharges by optical emission and absorption spectroscopy. *J. Vac. Sci. Technol. A*, 15:1890 – 1896, 1997.

[28] S. Dosa, S. Ghosal, R. L. Kosut, J. L. Ebert, T. E. Abrahamson, A. Kozak, D. W. Zou, X. Zhou, J. F. Groves, and H. N. G. Wadley. Reactor-scale models for rf diode sputtering of metal thin films. *J. Vac. Sci. Technol. A*, 17(4):1926 – 1933, 1999.

[29] Tilo P. Drüsedau, Mirko Löhmann, and Bernd Garke. Decay length of the pressure dependent deposition rate for magnatron sputtering. *J. Vac. Sci. Technol. A*, 16(4):2728 – 2732, 1998.

[30] C. Eisenmenger-Sittner, R. Beyerknecht, and A. Bergauer. Angular distribution of sputtered neutrals in a post magnetron geometry: Measurement and Monte Carlo simulation. *J. Vac. Sci. Technol. A*, 13(5):2435 – 2443, 1995.

[31] R. Elsing. The practical use and application of Monte-Carlo studies in physical vapour deposition technology. *Surf. Coat. Technol.*, 49:132 – 138, 1991.

[32] C. B. Eom, J. Z. Sun, K. Yamamoto, A. F. Marshall, K. E. Luther, T. H. Geballe, and S. S. Landerman. In situ grown $YBa_2Cu_3O_{7-\delta}$ thin films from single-target magnetron sputtering. *Appl. Phys. Lett.*, 55:595 – 597, 1989.

[33] C. C. Fang, F. Jones, R. R. Kola, G. K. Celler, and V. Prasad. Stress and microstructure of sputter-deposited thin films: Molecular dynamics simulations and experiment. *J. Vac. Sci. Technol. B*, 11(6):2947 – 2952, 1993.

[34] C. C. Fang, V. Prasad, and F. Jones. Molecular dynamics modeling of microstructure and stresses in sputter-deposited thin films. *J. Vac. Sci. Technol. A*, 11(5):2778 – 2789, 1993.

[35] L. J. Friedrich, S. K. Dew, M. Brett, and T. Smy. Thin film microstructure modelling through line-segment simulation. *Thin Solid Films*, 266:83 – 88, 1995.

[36] L. J. Friedrich, S. K. Dew, M. J. Brett, and T. Smy. Integrating system and feature scale models to study copper reflow. *J. Vac. Sci. Technol. B*, 17(1):186 – 193, 1999.

[37] L. J. Friedrich, D. S. Gardner, S. K. Dew, M. J. Brett, and T. Smy. Study of the copper reflow process using the GROFILMS simulator. *J. Vac. Sci. Technol. B*, 15(5):1780 – 1787, 1997.

[38] J. R. Gavaler, J. Talvacchio, T. T. Braggins, M. G. Forrester, and J. Greggi. Critical paramters in the sinble-target sputtering of $YBa_2Cu_3O_7$. *J. Appl. Phys.*, 70:4383 – 4391, 1991.

[39] Michael J. Grapperhaus, Zoran Krivokapic, and Mark J. Kushner. Design issues in ionized metal physical vapor deposition of copper. *J. Appl. Phys.*, 83(1):35 – 43, 1998.

[40] S. Hamaguchi and S. M. Rossnagel. Simulations of trench-filling profiles under ionized magnetron sputtermetal deposition. *J. Vac. Sci. Technol. B*, 13(2):183 – 191, 1995.

[41] G. L. Hansen and R. G. Ahonen. The effect of gas scattering on the deposition profile of optical thin films. *J. Vac. Sci. Technol. A*, 5(5):2898 – 2901, 1987.

[42] M. Hasegawa and K. Nanbu. Numerical analysis of film growth and step coverage in the collimation sputtering method. *Vacuum*, 48(10):825 – 831, 1997.

[43] T. Heberlein, G. Krautheim, and W. Wuttke. The sputter deposition process : a Monte-Carlo study. *Vacuum*, 42:47 – 51, 1991.

[44] D. Henderson, M. H. Brodsky, and P. Chaudhari. Simulation of structural anisotropy and void formation in amorphous thin films. *Appl. Phys. Lett.*, 25(11):641 – 643, 1974.

[45] D. W. Hoffman. A sputteirng wind. *J. Vac. Sci. Technol. A*, 3(3):561 – 566, 1985.

[46] D. W. Hoffman. Perspective on stresses in magnetron-sputtered thin films. *J. Vac. Sci. Technol. A*, 12(4):953 – 961, 1994.

[47] Jeffrey A. Hopwood, editor. *Ionized Physical Vapor Deposition*. Academic Press, San Diego, 2000.

[48] T. Horaguchi and T. Hirata. ATMLINE: relational database for atomic spectrum lines. *Kyoto University Data Processing Center Bulletin*, 22:129 – 141, 1989. (in Japanese).

[49] Yoichi Hoshi and Eisuke Suzuki. Investigation of sputter deposotion process of iron films by computer simulation. *IONICS*, 21(1):37 – 44, 1995. (in Japanese).

[50] R. P. Howson, H. A. J'afer, and A. G. Spencer. Substrate effects from an unbalanced magnetron. *Thin Solid Films*, 193/194:127 – 137, 1990.

[51] T. C. Huang, G. Lim, F. Parmigiani, and E. Kay. Effect of ion bombardment during deposition on the x-ray microstructure of thin silver films. *J. Vac. Sci. Technol. A*, 3(6):2161 – 2166, 1985.

[52] Shunji Ido, Mieko Kashiwagi, and Mikihiko Takahashi. Computational studies of plasma generation and control in a magnetron sputtering system. *Jpn. J. Appl. Phys.*, 38(7B):4450 – 4454, 1999.

[53] Shunji Ido and Kosuke Nakamura. Computational studies on plasma generation and erosion in rectangular magnetron sputtering system. *Jpn. J. Appl. Phys.*, 35(4A):2302 – 2305, 1996.

[54] Shunji Ido, Takeshi Suzuki, and Mieko Kashiwagi. Computational studies on the erosion process in a magnetron sputtering system with a ferromagnetic target. *Jpn. J. Appl. Phys.*, 37(3A):965 – 969, 1998.

[55] Masanobu Ishida, Yukio Yamaguchi, and Yasunori Yamamura. Simulation of the MO film deposition in the magnetron sputtering discharge. *Thin Solid Films,*, 334:225 – 229, 1998.

[56] J. Jeans. *The dynamical theory of gases*. Dover publications, Dover, 4th edition, 1954.

[57] Robert W. Johnson and A. H. Daane. The langhanum-boron system. *J. Phys. Chem.*, 65:909 – 915, 1961.

[58] S. Kadlec and J. Musil. Optimized magnetic field shape for low pressure magnetron sputtering. *J. Vac. Sci. Technol. A*, 13(2):389 – 393, 1995.

[59] T. Kajiwara, T. Urakabe, K. Sano, K. Fukuyama, K. Watanabe, S. Baba, T. Nakano, and A. Kinbara. Mechanical and electrical properties of rf sputtered LaB_6 thin films on glass substrates. *Vacuum*, 41:1224 – 1228, 1990.

[60] Manfred Kaminsky. *Atomic and ionic impact phenomena on metal surfaces.* Springer-Verlag, Berlin, 1965.

[61] Suk Tai Kang, Ryuichi Shimizu, and Tsuyoshi Okutani. Sputtering of Si with keV Ar^+ ions. I. measurement and Monte Carlo calculations of sputtering yield. *Jpn. J. Appl. Phys.*, 18:1717 – 1725, 1979.

[62] E. Kay, F. Parmigiani, and W. Parrish. Microstructure of sputtered metal films grown in high- and low-pressure discharges. *J. Vac. Sci. Technol. A*, 6(6):3074 – 3081, 1988.

[63] J. H. Keller and R. G. Simmons. Sputtering process model of deposition rate. *IBM J. Res. Develop.*, 23(1):24 – 32, 1979.

[64] A. Kersch, W. Morokoff, and Chr. Werner. Selfconsistent simulation of sputter deposition with the Monte Carlo method. *J. Appl. Phys.*, 75(4):2278 – 2285, 1994.

[65] A. Kinbara, T. Nakano, A. Kobayashi, S. Baba, and T. Kajiwara. LaB_x thin films prepared by magnetoron sputtering. *Appl. Surf. Sci.*, 70/71:742 – 745, 1993.

[66] Donald E. Knuth. *The Art of Computer Programming, Volume 2: Seminumerical Algorisms.* Addisoin Wesley, Massachusetts, 3rd edition, 1997.

[67] P. Lecoeur, B. Mercey, and H. Murray. Influence of angular distribution on the deposition rate of species sputtered from a multicomponent target in differnt configurations: Appliocations to mixed valene copper oxides. *J. Vac. Sci. Technol. A*, 13(4):2221 – 2227, 1995.

[68] Francisco A. Leon. Numerical modeling of glass flow and spin-on planarization. *IEEE Trans. CAD*, 7(2):168 – 173, 1988.

[69] Michael A. Lieberman and Allan J. Lichtenberg. *Principles of plasma discharges and materials processing.* Jon Wiley & Sons, Inc., New York, 1994.

[70] Z. Lin and T. S. Cale. Flux distributions and deposition profiles from hexagonal collimatorsdduring sputter deposition. *J. Vac. Sci. Technol. A*, 13(4):2183 – 2188, 1995.

[71] Mike Loukides. *UNIX for FORTRAN Programmers.* O'Reilly & Associates, Sebastopol, 1990.

[72] John E. Mahan and Andre Vantomme. A simplified collisional model of sputtering in the linear cascade regime. *J. Vac. Sci. Technol. A*, 15(4):1976 – 1989, 1997.

[73] John E. Mahan and Andrè Vantomme. Trends in sputter yield data in the film deposition regime. *Phys. Rev. B:*, 61(12):8516 – 8525, 2000.

[74] Maxim A. Makeev and Albert-László Barabási. Ion-induced effective surface diffusion in ion sputtering. *Appl. Phys. Lett.*, 71(19):2800 – 2802, 1997.

[75] A. Malaurie and A. Bessaudou. Numerical simulation of the charactersistics of the different metallic species falling on the growing film in d.c. magnetron sputtering. *Thin Solid Films*, 286:305 – 316, 1996.

[76] A. Manenschijn and W. J. Goedheer. Angular ion and nertral energy distribution in a collisional rf sheath. *J. Appl. Phys.*, 69(5):2923 – 2930, 1991.

[77] A. Manenschijn, G. C. A. M. Janssen, E. van der Drift, and S. Radelaar. Measurement of ion impact energy and ion flux at the rf electrode of a parallel plate reactive ion etcher. *J. Appl. Phys.*, 69(3):1253 – 1262, 1991.

[78] Rod S. Mason, John C. Naylor, Michael G. Hatcher, and W. Jeremy Jones. Production, thermalization, and transport of sputtered lithium atoms across a glow discharge plasma, studied by concentration modulated absorption spectroscopy. *J. Appl. Phys.*, 84(3):1179 – 1185, 1988.

[79] D. M. Mattox. Particle bombardment effects on thin-film depositoin: A review. *J. Vac. Sci. Technol. A*, 7(3):1105 – 1114, 1989.

[80] T. M. Mayer, E. Chason, and A. J. Howard. Roughening instability and ion-induced viscous relaxation of SiO_2 surfaces. *J. Appl. Phys.*, 76(3):1633 – 1643, 1994.

[81] A. A. Mayo, S. Hamaguchi, J. H. Joo, and S. M. Rossnagel. Across-wafer nonuniformity of long throw sputter deposition. *J. Vac. Sci. Technol. B*, 15(5):1788 – 1793, 1997.

[82] T. Mehdi, P. B. Legrand, J. P. Dauchot, M. Wautelet, and M. Hecq. Optical emission diagnostics of an rf magnetron sputtering discharge. *Spectrochim. Acta*, 48B:1023 – 1033, 1993.

[83] Kevin Meyer, Ivan K. Schuller, and Charles M. Falco. Thermalization of sputtered atoms. *J. Appl. Phys.*, 52(9):5803 – 5805, 1981.

[84] S. Miyake, N. Shimura, and T. Makabe. Diagnostics of direct-current-magnetron discharges by the emission-selected computer-tomography technique. *J. Vac. Sci. Technol. A*, 10:1135 – 1139, 1992.

[85] Dae Won Moon and Kyung Joong Kim. Surface topography development on ion-beam-sputtered surface: Role of surface inhomogeneity induced by ion-beam bombardment. *J. Vac. Sci. Technol. A*, 14:2744 – 2756, 1996.

[86] Charlotte E. Moore. *Atomic Energy Levels*, volume 2 of *NSRBS-NDS 35*. National Bureau of Standards, 1971.

[87] Masatake Mori. *FORTRAN 77 Suuchi Keisan Programing*. Iwanami Shoten, Tokyo, 1986. (in Japanese).

[88] Shigeichi Moriguchi, Kanehisa Udagawa, and Shin Hitotsumatsu. *Iwanami Suugaku Koushiki*. Iwanami Shoten, Tokyo, 1960. (in Japanese).

[89] Nobuhiro Motegi, Yuzou Kashimoto, Koji Nagatani, Seiichi Takahashi, Tomoyasu Kondo, Yasushi Mizusawa, and Izumi Nakayama. Long-throw low-pressure sputtering technology for very large-scale integrated devices. *J. Vac. Sci. Technol. B*, 13:1906 – 1909, 1995.

[90] T. Motohiro. Applications of Monte Carlo simulation in the analysis of sputter-deposition process. *J. Vac. Sci. Technol. A*, 4(2):189 – 195, 1986.

[91] T. Motohiro and Y. Taga. Monte Carlo simulation of thermalization process of sputterd particles. *Surf. Sci.*, 134:L494 – L499, 1983.

[92] T. Motohiro and Y. Taga. Monte Carlo simmulation of the practice transport process in sputter deposition. *Thin Solid Films*, 112:161 – 173, 1984.

[93] T. Motohiro and Y. Taga. On the elemental dependence of arrivval rate of the sputtered particles in the Monte Carlo simulation of the particle transport process in sputter deposition. *Thin Solid Films*, 172:L105 – L107, 1989.

[94] S. J. Mroczkowski. Electron emissinon characteristics of sputtered lanthanum hexaboride. *J. Vac. Sci. Technol.*, A9:586 – 590, 1991.

[95] Karl-Heinz Müller. Stress and microstructure of sputter-deposited thin films: Molecular dynamics investigations. *J. Appl. Phys.*, 62(5):1796 – 1799, 1987.

[96] G. K. Muralidhar, J. Musil, and S. Kadlec. An unbalanced magnetron sputtering device for low and medium pressures. *Rev. Sci. Instrum.*, 66(10):4961 – 4966, 1995.

[97] M. Muroi, T. Matsui, Y. Okamura, K. Tsuda, M. Nagano, and K. Mukae. Low temperature synthesis of $YBa_2Cu_3O_{7-x}$ thin films. *J. Mater. Res.*, 4:781 – 786, 1989.

[98] A. M. Myers, J. R. Doyle, J. R. Abelson, and D. N. Ruzic. Monte Carlo simulations of magnetron sputtering particle transport. *J. Vac. Sci. Technol. A*, 9(3):614 – 618, 1991.

[99] K. Nanbu, S. Uchida, and H. Yoshida. Computer simulation of growth of thin films fabricated by the sputtering method: comparison with experiment. *Thin Solid Films*, 228:330 – 332, 1993.

[100] National Astronomical Observatory, editor. *Rika Nenpyo (Chronological Scientific Tables 1999)*. Maruzen, Tokyo, 1998.

[101] John F. O'Hanlon. *A User's Guide to Vacuum Technology*. Jon Wiley & Sons, Inc., New York, 1989.

[102] T. Ohta and H. Yamada. A sputter equipment simulation system for VLSI device. *Vacuum*, 51(4):479 – 484, 1998.

[103] T. Okutani, M. Shikata, S. Ichimura, and R. Shimizu. Auguiar distribution of Si atoms sputtered by keV Ar^+ ions. *J. Appl. Phys.*, 51:2884 – 2887, 1980.

[104] W. Z. Park, T. Eguchi, C. Honda, K. Muraoka, Y. Yamagata, B. W. James, M. Maeda, and M. Akazaki. Investigation of the thermalizaiton of sputtered atoms in a magnetron discharge using laser-induced fluorescence. *Appl. Phys. Lett.*, 58(3):2564 – 2566, 1991.

[105] Robert Parsons. Sputter deposition processes. In John L. Vossen and Werner Kern, editors, *Thin Film Processes II*, chapter II-4. Academic Press, San Diego, 1991.

[106] H. Patterson and D. H. Tomlin. Experiments by radioactive tracer methods on sputtering by rare-gas ions. *Proc. Roy. Soc. London Ser.A*, 265:474 – 488, 1962.

[107] A. M. C. Pérez-Martin and J. J. Jiménez-Rodríguez. Angular distribution and escape probability of sputtered atoms. *Vacuum*, 42:537 – 542, 1991.

[108] A. J. Perry, D. Vender, and R. W. Boswell. The application of the helicon source to plasma sputtering. *J. Vac. Sci. Technol. B*, 9(2):310 – 317, 1991.

[109] I. Petrov, I. Ivanov, V. Orlinov, and J. E. Sundgren. Comparison of magnetron sputter deposition conditions in neon, argon, krypton, and xenon discharges. *J. Vac. Sci. Technol. A*, 11(5):2733–2741, 1993.

[110] Z. J. Radzimski, O. E. Hankins, W. P. Posadowski J. J. Cuomo, and S. Shingubara. Optical emission spectroscopy of high density metal plasma formed during magnetron sputtering. *J. Vac. Sci. Techonol. B*, 15:202 – 208, 1997.

[111] G. Mohan Rao and S. Mohan. Optimization studies on magnetic field geometry for planar magnetron sputtering targets. *J. Vac. Sci. Technol. A*, 9(6):3100 – 3104, 1991.

[112] R. L. Rhoades and S. M. Gorbatkin. Characterization of Ar/Cu electron-cycrotron-resonance plasmas using optical emissio nspectroscopy. *J. Appl. Phys.*, 80:2605 – 2613, 1996.

[113] R. S. Robinson. Energetic binary collisions in rare gas plasmas. *J. Vac. Sci. Technol.*, 16(2):185 – 188, 1979.

[114] S. M. Rossnagael. Directional and preferential sputtering-based physical vapor deposition. *Thin Solid Films*, 263:1 – 12, 1995.

[115] S. M. Rossnagel. Gas density reduction effects in magnetrons. *J. Vac. Sci. Technol. A*, 6(1):19 – 24, 1988.

[116] S. M. Rossnagel. Energetic particle bombardment of films during magnetron sputtering. *J. Vac. Sci. Technol. A*, 7(3):1025 – 1029, 1989.

[117] S. M. Rossnagel. Directional and ionized physical vapor deposition for microelectronics applications. *J. Vac. Sci. Technol. B*, 16:2585 – 2608, 1998.

[118] S. M. Rossnagel and J. J. Cuomo. Film modification by low energy ion bombardment during deposition. *Thin Solid Films*, 171:143 – 156, 1989.

[119] S. M. Rossnagel and J. Hopwood. Magnetron sputter deposition with high levels of metal ionization. *Appl. Phys. Lett.*, 63(24):3285 – 3287, 1993.

[120] S. M. Rossnagel and J. Hopwood. Metal ion deposition from ionized magnetron discgarge. *J. Vac. Sci. Technol. B*, 12:449 – 453, 1994.

[121] S. M. Rossnagel, D. Mikalsen, H. Kinoshita, and J. J. Cuomo. Collimated magnetron sputter deposition. *J. Vac. Sci. Technol. A*, 9(2):261 – 265, 1991.

[122] S. M. Rossnagel and K. L. Saeger. Optical emission in magnetrons: Nonlinear aspects. *J. Vac. Sci. Technol. A*, 7(3):968 – 971, 1989.

[123] S. M. Rossnagel, I. Yang, and J. J. Cuomo. Compositional changes during magnetron sputtering of alloys. *Thin Solid Films*, 199:59 – 69, 1991.

[124] D. N. Ruzic and H. K. Chiu. Modeling of particle-surface reflections including surface roughness characterized by fractal geometry. *J. Nucl. Mater.*, 162-164:904 – 909, 1989.

[125] David N. Ruzic. The effects of surface roughness characterized by fractal geometry on sputtering. *Nucl. Instr. and Meth.*, B47(3):118 – 125, 1990.

[126] J. G. Ryan and S. Roberts. The formation and characterization of rare earth boride films. *Thin Solid Films*, 135:9 – 19, 1986.

[127] K. Sakuta, M. Iyori, Y. Katayama, and T. Kobayashi. Effect of discharge gas pressure on YBaCuO epitaxial film formation by reactive RF magnetron sputtering. *Jpn. J. Appl. Phys.*, 29:L611 – L613, 1990.

[128] S. Scaglione, L. Caneve, and F. Sarto. Sputtering yield of optical materials: Sigmund's model and experimental results. *J. Vac. Sci. Technol. A*, 12(4):1523 – 1527, 1994.

[129] Ivan K. Schuller and Charles M. Falco. Structure and physical properties of sputtered metallic superlattices. *Surf. Sci.*, 113:443 – 453, 1982.

[130] Vladimir V. Serikov and Kenichi Nanbu. Monte Carlo numerical analysis of target erosion and film growth in a three-dimensional sputtering chamber. *J. Vac. Sci. Technol. A*, 14:3108 – 3123, 1996.

[131] Vladimir V. Serikov and Kenichi Nanbu. The analysis of background gas heating in direct current sputtering discharges via particle simulation. *J. Appl. Phys.*, 82(12):5948 – 5957, 1997.

[132] T. E. Sheridan, M. J. Goeckner, and J. Goree. Model of energetic electron transport in magnetron discharges. *J. Vac. Sci. Technol. A*, 8:30 – 37, 1990.

[133] T. E. Sheridan, M. J. Goeckner, and J. Goree. Electron velocity distribution functions in a sputtering magnetron discharge for the E×B direction. *J. Vac. Sci. Technol. A*, 16(4):2173 – 2176, 1998.

[134] Eiji Shidoji, Hiroto Ohtake, Nobuhiko Nakano, and Toshiaki Makabe. Two-dimensional self-consistent simulation of a dc magnetron discharge. *Jpn. J. Appl. Phys.*, 38(4A):2131 – 2136, 1999.

[135] Peter Sigmund. Theory of sputtering. I. sputtering yield of amorphous and polycrystalline targets. *Phys. Rev.*, 184:383 – 416, 1969.

[136] Peter Sigmund. A mechanism of surface micro-roughening by ion bombardment. *J. Mater. Sci.*, 8:1545 – 1553, 1973.

[137] T. Smy, L. Tan, S. S. Winterton, S. K. Dew, and M. J. Brett. Simulation of sputter deposition at high pressures. *J. Vac. Sci. Techinol. A*, 15:2847 – 2853, 1997.

[138] Tom Smy, Kenneth L. Westra, and Michael J. Brett. Simulation of density variation and step coverage for a variety of via/contact geometries using SIMBAD. *IEEE Trans. Electron Devices*, 37(3):591 – 598, 1990.

[139] R. E. Somekh. The thermalization of energetic atoms during the sputtering process. *J. Vac. Sci. Technol. A*, 2:1285 – 1291, 1984.

[140] J. Stache. Hybrid modeling of deposition profiles in magnetron sputtering systems. *J. Vac. Sci. Technol. A*, 12(5):2867 – 2872, 1994.

[141] Keisuke Sugano, Kazuyoshi Yoshimura, and Fumio Takayama. *C ni yoru spline kansuu*. Tokyo Denki University Press, Tokyo, 1993. (in Japanese).

[142] S. Swann. Film thickness distribution in magnetron sputtering. *Vacuum*, 38:791 – 794, 1988.

[143] R. N. Tait, S. K. Dew, T. Smy, and M. J. Brett. Density variation of tungsten filims sputtered over topography. *J. Appl. Phys.*, 70(8):4295 – 4300, 1991.

[144] R. N. Tait, T. Smy, and M. J. Brett. Simulation and measurement of density variation in Mo films sputter deposited over oxide steps. *J. Vac. Sci. Technol. A*, 8(3):1593 – 1596, 1990.

[145] N. Terada, H. Ihara, M. Jo, M. Hirabayashi, Y. Kimura, K. Matsutani, K. Hirata, E. Ohno, R. Sugise, and F. Kawashima. Sputter synthesis of $Ba_2YCu_3O_y$ as-deposited superconducting thin films from stoichiometric target—A mechanism of compositional deviation and its control. *Jpn. J. Appl. Phys.*, 27:L639 – L642, 1988.

[146] M. W. Thompson. II. the energy spectrum of ejected atoms during the high energy sputteirng of gold. *Philos. Mag.*, 18:377 – 414, 1968.

[147] J. A. Thornton. The microstructure of sputter-deposited coatings. *J. Vac. Sci. Technol. A*, 4(6):3059 – 3065, 1986.

[148] John A. Thornton. Influence of apparatus geometry and deposition conditions on the structure and topography of thick sputtered coatings. *J. Vac. Sci. Technol.*, 11(4):666 – 670, 1974.

[149] H. Tsuge and S. Esho. Angular distribution of sputtered atoms from polycrystalline metal targets. *J. Appl. Phys.*, 52(7):4391 – 4395, 1981.

[150] R. T. C. Tsui. Calculation of ion bombarding energy and its distribution in rf sputtering. *Phys. Rev.*,, 168(1):107 – 113, 1968.

[151] Mutumi Tuda, Kouichi Ono, and Akimasa Yuuki. Transport and deposition processes of sputtered particles in rf-microwave hybrid sputtering discharges. *Jpn. J. Appl. Phys.*, 33(7B):4473 – 4477, 1994.

[152] G. M. Turner. Monte Carlo calculations of gas rarefaction in a magnetron sputtering discharge. *J. Vac. Sci. Technol. A*, 13(4):2161 – 2169, 1995.

[153] G. M. Turner, I. S. Falconer, B. W. James, and D. R. McKenzie. Monte Carlo calculation of the thermalization of atoms sputtered from the cathode of a sputtering discharge. *J. Appl. Phys.*, 65:3671 – 3679, 1989.

[154] G. M. Turner, I. S. Falconer, B. W. James, and D. R. McKenzie. Monte Carlo calculations of the properties of sputtered atoms at a substrate surface in a magnetron discharge. *J. Vac. Sci. Technol. A*, 10(3):455 – 461, 1992.

[155] G. M. Turner, A. Sikorski, D. R. McKenzie, G. B. Smith, K. Ng, and D. J. H. Cockayne. Spatial variations in the stoichiometry of sputtered YBaCuO thin films: theory and experiment. *Physica C*, 170:473 – 480, 1990.

[156] H. M. Urbassek and D. Sibold. Sputterd atom transport in high-current gas discharges: A self-consistent computer simulation study. *J. Vac. Sci. Technol. A*, 11:676 – 681, 1993.

[157] M. A. Vidal and R. Asomoza. Monte Carlo simulation of the transport process in the growth of *a*-Si:H prepared by cathodic reactive sputtering. *J. Appl. Phys.*, 67(1):477 – 482, 1990.

[158] Robert K. Waits. Planar magnetron sputtering. In John L. Vossen and Werner Kern, editors, *Thin Film Processes*, chapter II-4. Academic Press, San Diego, 1978.

[159] W. Wang, J. Foster, A. E. Wendt, T̃. Onuoha J. H. Booske, P. W. Sandstorm, H. Liu, S. S. Gearhart and N. Hershkowitz. Magnetic-field-enhanced rf argon plasma for ionized sputtering of copper. *Appl. Phys. Lett.*, 71:1622 – 1624, 1997.

[160] X. Wang, H. Masumoto, Y. Someno, and T. Hirai. Optical properties of titania/silica multilayer filters prepared by helicon plasma sputtering. *J. Vac. Sci. Technol. A*, 16(5):2926 – 2930, 1998.

[161] Kiyotaka Wasa and Shigeru Hayakawa. *Handbook of sputter deposition technology.* Noyes Publications, New Jersey, 1992.

[162] Bernhard Welz and Michael Sperling. *Atomic absorption spectrometry.* Wiley-VCH, Weinheim, 3rd edition, 1999.

[163] W. D. Westwood. Calculation of deposition rates in diode sputtering systems. *J. Vac. Sci. Technol.*, 15(1):1 – 9, 1978.

[164] H. Windischmann. Intrinsic stress in sputtered thin films. *J. Vac. Sci. Technol. A*, 9(4):2431 – 2436, 1991.

[165] Henry Windischmann. Intrinsic stress in sputter-deposited thin films. *Crit. Rev. Solid State Mater. Sci.*, 17(6):547 – 596, 1992.

[166] B. Window. Removing the energetic neutral ploblem in sputtering. *J. Vac. Sci. Technol. A*, 11(4):1522 – 1527, 1993.

[167] B. Window and N. Savvides. Unbalanced dc magnetrons as sources of high ion fluxes. *J. Vac. Sci. Technol. A*, 4(3):453 – 456, 1986.

[168] Harold F. Winters, H. J. Coufal, and W. Eckstein. Influence of energy reflected from the target on thin film characteristics. *J. Vac. Sci. Technol. A*, 11(3):657 – 663, 1993.

[169] W.L.Patterson and G.A.Shirn. The sputtering of nickel-chromium alloys. *J. Vac. Sci. Technol.*, 4(6):343 – 346, 1967.

[170] L. C. Wrobel. *Potential and viscous flow problems using the boundary element method.* PhD thesis, The University of Southampton, 1981.

[171] C. T. Wu, R. T. Kampwirth, and J. W. Hafstrom. High-rate magnetron sputtering of high t_c Nb_3Sn films. *J. Vac. Sci. Technol.*, 14(1):134 – 137, 1977.

[172] S. C. Wu, H. T. Hsu, F. H. Chen, W. R. Chang, and T. Y. Tseng. Growth parameter effect in superconducting $YBa_2Cu_4O_8$ thin films by d.c. magnetron sputtering. *J. Mater. Sci. Lett.*, 29:5593 – 5598, 1994.

[173] S. C. Wu, W. C. Tsai, C. K. Huang, H. T. Hsu, C. J. Huang, and T. Y. Tseng. Pressure effect on $YBa_2Cu_3O_7$ thin films growth in off-axis radio frequency magnetron sputtering. *J. Vac. Sci. Technol.*, A13:2412 – 2419, 1995.

[174] J. Xu, B. M. Moon, and K. V. Rao. Study of the resputtering effect during rf-sputter deposition of YBCO films. *J. Mater. Res.*, 10:798 – 802, 1995.

[175] Y. Yamamura and M. Ishida. Monte Carlo simulation of the thermalization of sputtered atoms and reflected atoms in the magnetron sputtering discharge. *J. Vac. Sci. Technol. A*, 13:101 – 112, 1995.

[176] Yasunori Yamamura. Computer studies of reemission and depth profiles for helium on molybdenum. *Nucl. Instr. and Meth.*, B28:17 – 26, 1987.

[177] Yasunori Yamamura and Hiro Tawara. Energy dependence of ion-induced sputtering yields from monatomic solids at normal incidence. *Atomic Data and Nuclear Data Tables*, 62(2):149 – 253, 1996.

[178] YiFeng Yang, Ji Ung Lee, and James E. Nordman. Effects of target presputtering on stoichiometry of sputtered Bi-Sr-Ca-Cu-O thin films. *J. Vac. Sci. Technol. A*, 10(5):3288 – 3291, 1992.

[179] P. Ziemann and E. Kay. Correlation between the ion bombardment during film growth of Pd films and their structural and electrical properties. *J. Vac. Sci. Technol. A*, 1(2):512 – 516, 1983.